Indicators for the Signal Degradation and Optimization of Automotive Radar Sensors under Adverse Weather Conditions

Vom Fachbereich 18 - Elektrotechnik und Informationstechnik
der Technischen Universität Darmstadt
zur Erlangung der Würde eines
Doktor-Ingenieurs (Dr. -Ing.)
genehmigte

Dissertation

von

Dipl. -Ing. Alebel Arage Hassen
aus Worillu / Wollo / Äthiopien

Referent:	Prof. Dr. -Ing. Rolf Jakoby
Korreferent:	Prof. Dr. -Ing. habil. Peter Knoll

Zeitdauer:	09.2003 - 08.2006
Tag der Einreichung:	14.11.2006
Tag der Disputation:	18.12.2006

Darmstadt 2006
D17
Darmstädter Dissertationen

Abstract

In recent years vehicle radar and lidar sensors are widely used as sources of control signals for Autonomous Intelligent Cruise Control and Collision Mitigation systems. These devices are operating in the millimeter wave and infrared range in which their performance may be degraded by adverse weather conditions. Currently available information regarding the signal interaction with fog, rain, snow and spray make clear that millimeter-wave radar sensors are far less affected by adverse weather conditions than infrared-based sensors [1, 2, 3, 4]. However, when automotive radar sensors are particularly designed for safety-oriented systems, the effects of critical issues (such as water film and heavy rains) on the sensor performance become of the uttermost importance.

In this thesis, an analysis of the effects of water film and rain on millimeter-wave propagation have been presented. Based on the fundamental formulation of wave propagation and scattering in stratified as well as random media, physical parameters describing the wave interaction with the water film and rains have been studied and assessed. It has been shown that both significantly attenuate millimeter-wave signals, and may exert an adverse influence on detection performance of millimeter-wave radar sensors. Consequently, **water-film and rain indicators have been derived from returned signals to convey for the first time wet-antenna and rain information to the radar sensor system, where they could be employed for monitoring the radar detection performance**.

Methods have also been worked out in detail for **low-cost measurement of water-film and rain indicators** in the radar system. Experimental investigations have been exhibited to be able to satisfactorily implement these indicators in production. Finally, **techniques have been introduced to show how detection performance could be optimized**.

The presented findings emphasize the importance of identification of water film and rain and of being able to optimize detection performance in order to assure availability of automotive radar senors in adverse weather conditions. Results should also be significant for all kinds of millimeter-wave radar sensors where wave interactions with water film on the surface of the radar antenna or its protecting radome as well as with rains in the radar beams are the key issue.

Abstract in German

Automotive Radar- und Lidarsensoren werden in den letzten Jahren als Steuersignalequelle für Systemen wie Autonomous Intelligent Cruise Control (AICC) und Collision Mitigation (CM) verstärkt eingesetzt. Diese Sensoren operieren in Millimeterwellen und Infrarotbereich, in welche ihre performanz bei sclechten Wetterverhältnisse signifikant degradiert werden können, und müssen diesen durch geeignetes Design erkannt und angepaßt werden. Besonders wichtig für Millimeterwelle basierten Automotiveradarsensoren ist die automatische Erkennung von der Wasserfilm auf der Antennenöberfläche und dem Regen im Übertragungsmedium um die Degradation der Radarsichtweit und -detektionsvermögen dynamisch zu unterdrücken bzw. zu vermeiden. In dieser Dissertationsarbeit werden neueartigen Wasserfilm- und Regenindikatoren vorgestellt, die kostengünstig mit dem am Markt vertretenden Automotiveradarsensor von Bosch demonstriert sind und während dieser Arbeit auf Serientauglichkeit untersucht worden. Ferner wird ein Performanzoptimierungsverfahren zur Gewährleistung der Radarsensorverfügbarkait bei schlechtem Wetter presentieren.

Acknowledgments

This work is carried out within the framework of a Ph. D. stipendium of the Robert Bosch GmbH at the department of Development Long Range Radar devision of Automotive Electronic Driver Assistance in Leonberg, Baden-Württemberg, Germany. Therefore all the persons at this devision are most gratefully acknowledged.

I wish to express my sincere gratitude to:

My supervisor Professor Dr. -Ing. Rolf Jakoby, for giving me supervision and inspiration in the Technische Universität Darmstadt; and co-supervisor Professor Dr.-Ing. habil. Peter Knoll, for advising and supporting me to continue and complete this Ph. D. work in the Robert Bosch GmbH, Leonberg.

All those who have contributed to this work, and shared their knowledge with me, here I would like to mention W. M. Steffens, J. Hauk, J. Hildebrand, T. Binzer and J. Winterhalter.

Those who have helped me with measurements in one or another way:
K. D. Mioska, P. Wirth, R. Hermann and D. R. Reddy.

Those who have reviewed this thesis and suggested substantial improvements:
A. Damtew and T. Hussien.

My Family and, of course, the almighty God who gave me strength and imperturbability.

Darmstadt, December 2006 Alebel Arage

Contents

List of Figures

List of Tables

Chapter 1

Introduction

Motivation

Since 1970 automotive radar sensors have been investigated to use for more convenient and safer driving, and have been first employed as cruise control system in the 1980*s* [5, 6]. This application has been recently spread to Autonomous Intelligent Cruise Control (AICC) and Collision Mitigation (CM) systems as a result of cooperate projects between car manufacturers, universities and micro-wave companies. For example, the European project that started in 1986, aimed to improve vehicle safety, efficiency, and economy, was one of the main driving factor in the development of various types of sensors for automobiles, including micro- and millimeter-wave radars.

Furthermore, an Advanced Safety Vehicle Program, started in 1991 under the initiative of Japans Transportation Minister, and product road-maps of automotive system manufacturers show that the incoming trend of this technology is focusing at autonomous driving [1, 7]. This may be the ultimate form of vehicle dynamics control system. Millimeter-wave radar and vision sensors are parts of the environmental recognition technology that will be required to achieve effective vehicle dynamics control.

Similar to millimeter-wave radar sensor, infrared-based sensor such as lidar has been also employed for environmental recognition, particularly for the Adaptive Cruise Control (ACC) system by considering required performance and feasibility. Both infrared-based and millimeter-wave radar sensors will

provide range, velocity and angle information on targets ahead of the vehicle. This will be used along with vehicle dynamics data to correlate projected vehicle path and detected target positions. The resulting data will be used to control the vehicle throttle, brakes, and steering or the automatic transmission. ACC system adapts the speed of the vehicle according to the speed of the vehicle ahead, in order to maintain a constant distance between the two vehicles. The driver sets the maximum speed and the minimum separation desired. Both sensor systems can also be used to locate and track multiple targets on the road ahead, to anticipate traffic conditions in the driving lane. The ACC system application of millimeter-wave and infrared-based sensors is marketed as a comfort and convenience option rather than a safety option. There is still a safety risk associated with its use on automobiles. Due to the critical impact of radar and lidar sensors on the ACC system, it is important to conduct accurate verification and calibration of the system at various stages of development, production, and installation. Hence, the use of ACC systems was restricted to highway driving for breaking up to a specified level. If additional breaking is required to slow the automobile, the ACC function is disabled and the driver has to take control on the automobile.

New generation systems make use of multiple sensors to extend the ACC system to city driving or stop-and-go traffic, pre-crash sensing, collision warning and avoidance systems (CWAS). These are typically short-range applications and various sensor types can be used, including infrared, vision, ultrasonic, and micro-wave radar. For most applications beyond highway ACC system, multiple sensor systems must be used in conjunction with the long-range ACC lidar or millimeter-wave radar sensors. Such sensor fusion technology is the key to achieve high level environmental recognition and to advance the target autonomous driving.

Most of these future safety-oriented applications are associated with increasing demands for grater performance and reliability in environmental recognition sensors at any traffic and weather scenarios. Unfortunately, with most recent developments and innovative products, such requirements appeared not to be met for all weather conditions. This is the challenge for long-range infrared-based and millimeter-wave radar sensors. As it is indispensable for safety-oriented applications, this has to be solved by these sensor engineers. Basically in adverse weather conditions, the electromagnetic wave interacts not only with hydrometeors (particles of water in solid or liquid

form in the atmosphere) but also with materials, which could be built up on the surface of the sensor or its protective covering. Some examples of hydrometeors are mist, rain, freezing rain, ice pellets, snow, hail and fog. Their sizes are generally 1 μm or more in radius. Expected materials on the surface of the sensor or its protective covering are like grit and dirt as well as dray snow and water films, which may be formed through condensation, impingement and stick of water-particles. The wave interaction with these materials and hydrometeors also results in attenuation and reflection that rely on the relationship between the particle-size and the wavelength as well as on the particle density, extent and index of refraction.

The refractive index of water is rather complicated with a strong temperature and frequency dependence. It is given in **Figure B.2** in a wide electromagnetic spectrum. In micro-wave range, the real part is around 10 with the imaginary part varying from around 0.2 to 2 but generally rising with temperature and frequency. In millimeter wave range (i.e. above 30 GHz), both the real and imaginary parts decrease. So in these both frequency ranges, water is known as lossy material. Attenuation due to water particle is thus a mixture of absorption and scatter losses. Due to low value of the imaginary part of the refractive index of water in the region 1 mm to 100 nm, water is transparent at optical frequencies. The attenuation will be then a result of energy lost through scattering by water particles. For the frequency spectrum above 10 GHz, the attenuation of electromagnetic energy due to water particles is presented in **Figure B.1**.

The different forms of water-particles (mist, rain, freezing rain, ice pellets, snow, hail and fog) affect the infrared and millimeter-wave propagation unequally. The reason is that the absorption and total scattering cross sections of the water-particle depend on the relationship between particle-size and wavelength as well as on the particle density and extent [2, § 3-2].

A very big fraction of the water-particles in the atmosphere has generally a diameter greater than ≥ 2 μm. For example, fog droplets are smaller than 100 μm in diameter and the number density may vary from 10^6 to 10^9 m^{-3} with typical value of 10^8 m^{-3}. The water content may vary from 0.03 g/m^3 for light fog to 2 g/m^3 for heavy fog, and optical visibility may be typically 1 km down to 30 m.
Raindrops, as the second example of water-particles in the atmosphere, are randomly positioned in space with a special drop size distribution that de-

pends on the rainfall intensity. They have generally diameters greater than (100 μm up to $4mm$). Laws and Parsons give an empirical raindrop-size distribution for a mean drop-size spectrum in continental temperate rainfall (**Figure 5.1**). It shows that a very big fraction of the raindrops at rainfall intensities 2.5 mm/hr and larger have a diameter greater than or equal to 1 mm.

Almost all sizes of these water-particles are greater than the infrared wavelengths ($\lambda \leq$ 30 μm). They may consequently yield maximum scattering cross sections (**Figure 2.6**) in the infrared and visible light range. This results in quit large attenuation and backscattered signal, particularly in dense water-particles like heavy rain and fog droplets (**Figure B.1**). These intelligibly degrads the performance of lidar sensor ($\lambda \leq$ 1 μm) not only by limiting the maximum detection range to that of comparable human eye, but also by increasing process occupies nontrivial amounts of memory and computational throughput to filter out irrelevant detections due to water-particles.

This also includes road spray that could arise during rainy weather condition from other road vehicles in front of the sensor-carrier vehicle [3]. Note that, due to beam spreading loss and scattering in the propagation path, only backscattered signals from road spray and water-drops in the near distance have considerable effect on the sensor performance.

In the millimeter-wave range, only raindrops with rainfall intensities greater than 4 mm/hr (**Figure 5.1**) can obtain maximum absorption and total scattering cross sections. This may introduce strong rain attenuation and backscattering. The effects of snow and hail are difficult to assess precisely since their water content varies significantly. In general, ice has a much smaller loss than water of the same mass, and millimeter-wave attenuation in dry snow is hence negligible [2, § 3-2]. If the snow is wet, however, the attenuation increases considerably but expected to be less than moderate rain. It all implies that the 77 GHz millimeter-wave radar may operate without any substantial degradation of performance in all forms of water-particles except rains with rainfall intensities $\geq$ 4 mm/hr (i.e moderate, heavy and extremely heavy rains).

As previously pointed out, water has a high dielectric constant and is a lossy material at micro-wave and millimeter-wave range. In the case of water

film on the surface of antenna or its radome, this may well provide enough attenuation and reflection according to the water-film thickness or amount of water content as well as frequency. It means, particularly for millimeter waves, a less degree of moisture on the surface of antenna lens or radome can adversely affect wave propagation and introduce ceasing of millimeter-wave radar operation.

On the other hand, lidar sensor is insensible to water film because of the pure dielectric property of water at optical frequencies. Nevertheless, dust materials like dry snow, grit and dirt on the lidar lens may also cause harm on measurement sensitivity due to attenuation and diffraction phenomena [8, § 14.5].

Regarding to effects of most of the water-particles on wave propagation at 77 GHz, attenuation and backscattering data have been collected from different scientific works, reported in the past, and presented on **Table 1.1**. These data as well confirms that the presence of rain and water film in the propagation path could be critical for performance of automotive radar sensors.

Table 1.1: Effects of water-particles on the 77 GHz wave propagation.

Media	*Materials*	*Attenuation*	*backscattering*	*Source*
Air	*fog* @gm/m^3	0.3 dB/km		[9]
	snow @gm/m^3	1 dB/km	-50 dBm^2/m^3	[10]
	rain @$5mm/hr$	4 dB/km	-35 dBm^2/m^3	[10, 11, 12]
	@$20mm/hr$	10 dB/km	-23 dBm^2/m^3	[11, 13]
	@$50mm/hr$	20 dB/km	-20 dBm^2/m^3	[14, 11]
	spray @ $\leq \frac{1}{2}mm$	0.1 dB/m	-20 dBm^2/m^3	[3]
Antenna	*waterfilm*	30 dB/mm	-3 dB	[15]
	ice @$0.5mm$	2 dB	-5 dB	[16]

In general, the above theoretical assumptions and experimental investigations in [3, 1] show that automotive radar sensors perform well better in

most adverse weather conditions than lidar sensors. Further improvement of this favorable aspect should make millimeter wave based automotive radar sensors reliable in all weather conditions.

Hence, this work has been focused more on the fundamental understanding of how water film and heavy rains affect the performance of millimeter-wave automotive radar sensors and how this could be recognized as well as counterbalanced, automatically. With a greater knowledge about these effects, the requirements of future advanced safety application systems (i.e. better performance and reliability at all weather conditions) may be substantially achieved by the millimeter-wave radar sensor.

Objectives

The aim of the thesis is to look for and optimize water-film and rain indicators, which enables to maintain availability of automotive radar sensors in adverse weather conditions like rain and snow. In a very general form, this has been presented schematically in **Figure 1.1**. More specifically, the contributions of this research to millimeter-wave radar sensors are:

- to investigate the effects of water film and rain on the detection performance,
- to find efficient water-film and rain indicators, and develop innovative techniques for their low-cost implementation in radar sensors system, and
- to propose methods for optimizing the detection performance in adverse weather conditions.

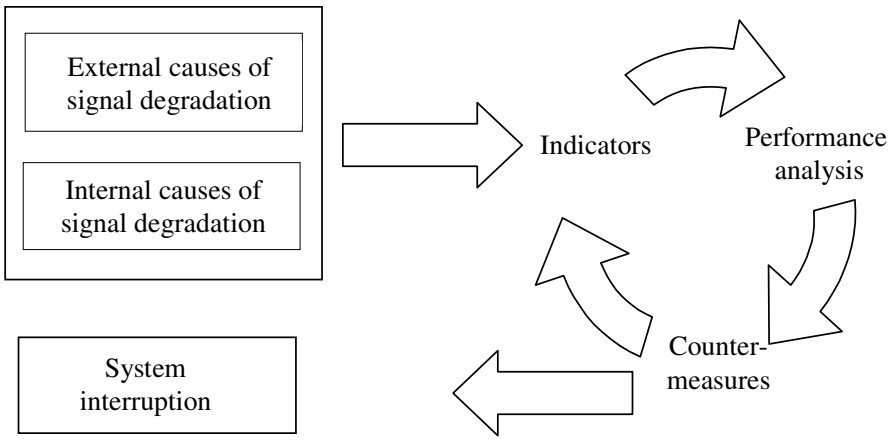

Figure 1.1: Possible performance optimization model of an automotive radar sensor system for safety-oriented applications: radar signal may be degraded due to external causes, e.g. adverse weather conditions, and/or internal causes, e.g. fault in the radar system components. Indicators, which have been developed to identify the kinds of radar signal degradation, may be used to determine the degree of performance loss and can be applied to command the necessary counteractions.

Outline of this work

As mentioned before, the interaction of electromagnetic waves with water film and rains may cause a significant effect on the wave propagation. In order to examine these effects on the detection performance of millimeter-wave radar sensors, Chapter 2 gives an essential summary about the propagation and scattering characteristics of electromagnetic waves in dielectric stratified media as well as in the presence of randomly distributed particles. This has been given rise to an understanding of the dielectric property of water and its dependence on micro- and millimeter-wave frequencies as well as on temperatures.

For the purpose of practical and feasible probe of the theoretical results, Chapter 3 discusses about the operation principle of a millimeter wave based radar sensors. The antenna technology, measurement system and some sys-

tem parameters of an actual automotive long range radar sensor have been reviewed in brief.

The main essence of this thesis is concentrated in Chapter 4 and Chapter 5. The theoretical analysis as well as the experimental and practical investigation of the effects of water film on millimeter-wave propagation have been treated in Chapter 4. Physical parameters such as reflectivity and transmissivity have been adapted with lossy stratified media, and used to describe the effects of water film on detection performance of millimeter-wave radar sensors. A water-film indicator has been derived from the correlation of these physical parameters and its relationship with the maximum detection range of a radar sensor has been worked out in detail. Results have been then verified with a number of experimental investigations. The electronic version of this work includes lab and on-road demonstrations of these results using an actual automotive radar sensor systems.

Chapter 5 deals with the theoretical and practical analysis of the effects of rain on the detection performance of millimeter-wave radar sensors. The theoretical analysis of effects of rain has been treated using results revised in Chapter 2. Particularly, the backscattering effect of rain has been examined for narrow beam monostatic radars using the first order multiple scattering principle. This covers the practical situation like deriving of rain indicator from backscattered signal in order to identify rain and its consequence on the detection performance of automotive radar sensors. The relationship between the loss of signal-to-noise ratio and rain backscattering cross section has been also elaborated. The investigation have been supported with practical experiments by comparing measurement results of an actual automotive radar sensor system and meteorological instrumentation like rain gauge.

In a compact form, Chapter 6 summarizes the essential results of this work. Further aspects regarding to performance optimization of automotive radar sensors have been also mentioned briefly.

Chapter 2

Wave propagation in stratified and random media

Before beginning discussions about the effects of water film and rain on the performance of millimeter-wave radar sensors and their identification mechanism, this chapter gives an essential summary about the propagation and scattering characteristics of electromagnetic waves in multi-layer media as well as in the presence of randomly distributed particles.

First, it deals with isotropic linear media, giving physical explanations for electric responses. Lossy materials, particularly water with dielectric properties that depends upon frequency and temperature, will be described succinctly using the Debye-model. And then, it demonstrates how physical parameters like reflectivity and transmissivity of stratified media can be determined using the fundamental formulation of the electromagnetic wave theory.

Finally it revises basic radar equations and examines the scattering and absorption properties of randomly distributed particles using single and first-order multiple scattering approximations. The results of these theoretical analysis will be directly applied in the upcoming chapters to illustrate effects of water film and rain on the performance of millimeter-wave radar sensors.

2.1 Characteristics of dielectrics

The response of materials to applied electromagnetic field includes displacements of both free and bound electrons by electric fields and the orientation of atomic moments by magnetic fields. These responses can be mostly treated as linear (i.e. proportional to the applied fields) over useful range of field magnitudes. Often, the response is independent of the direction of the applied field and such material is called isotropic. The frequency of the field counts to one of the key factors, which may significantly influence the reaction of these linear, isotropic materials to time-varying fields. Hence, it is of special importance to discuss the frequency dependence of permittivity, defined as the ability of a material to respond to the electric field.

Isotropic and linear materials have been considered in this text, and they are represented by scalar values of ϵ and μ (usual dielectrics $\mu = \mu_0$) for analysis at a given frequency. As they are given in several books and articles [17, 18, 19, 20, 21], various physical phenomena contributing to the complex permittivity differ for solids, liquids and gases. Nevertheless, some of the fundamental properties and simple models will be discussed to give insight into the most important characteristics [22, 8].
It can be shown that, if the atoms or molecules are polarized, a dipole moment density can be defined by

$$\mathbf{P}_d = \Delta V \overset{lim}{\rightarrow} 0 \ \ \frac{\sum_i \mathbf{p}_i}{\Delta V} \, . \tag{2.1}$$

Neglecting higher-order multi-poles, this is identical to the so called electrical polarization that enters the relation between the electric flux density $\mathbf{D}$ and the electric field vector $\mathbf{E}$

$$\mathbf{D} = \epsilon_0 \mathbf{E} + \mathbf{P} = \epsilon_0 \left(1 + \chi_e\right) \mathbf{E} \, . \tag{2.2}$$

The term $\epsilon_0 = 8.85 \times 10^{-12} F/m$ is the ability of a free space to store electrostatic energy (permittivity of free space), χ_e is the dielectric susceptibility and it has been assumed that $\mathbf{P}$ is linearly dependent on the $\mathbf{E}$. Few dielectric materials, such as polar dielectrics, have a permanent polarization that retards the orientation of the dipole molecules in the applied electric field $\mathbf{E}$. If there are N like molecules per unit volume, the induced polarization $\mathbf{P}$ may be written

$$\mathbf{P} = \epsilon_0 \chi_e \mathbf{E} = N g \alpha_T \mathbf{E} \, , \tag{2.3}$$

where α_T is the molecular polarizability and g is the ratio between local field acting on the molecule and the applied field $\mathbf{E}$. The local field differs from the applied field because of the effect of surrounding molecules. The corresponding electric flux density may also be written

$$\mathbf{D} = \epsilon\mathbf{E} = \epsilon_0\epsilon_r\mathbf{E} \, . \tag{2.4}$$

So, comparing (2.4) with (2.2) and (2.3) gives the relative permittivity

$$\epsilon_r = 1 + \frac{Ng\alpha_T}{\epsilon_0} = 1 + \chi_e \, . \tag{2.5}$$

If the surrounding molecules act in a spherically symmetric fashion on the molecule for which the local electric field is being calculated, g can be shown to be $\frac{(2+\epsilon_r)}{3}$ and (2.5) may then be written as

$$\frac{\epsilon_r - 1}{\epsilon_r + 2} = \frac{N\alpha_T}{3\epsilon_0} \, . \tag{2.6}$$

This expression is known as the Clausius-Mossotti relation, or when frequency effects in α_T are included, the Debye equation [22, p. 669]. It is proved to be accurate for gases, and gives qualitative behavior for liquids and gases.

The molecular polarizability α_T has contributions from several different atomic or molecular effects. One part, called electronic, arises from the shift of electron cloud in each atom relative to its positive nucleus. Another part, called ionic, comes from the displacement of positive and negative ions from their neutral position. Still another part may arise if the individual molecules have permanent dipole moments. Application of the electric field tends to align these permanent dipoles against the randomizing forces of molecular collision, and since random motion is a function of temperature, this effect is clearly temperature dependent. The three effects together constitute the total molecular polarizability,

$$\alpha_T = \alpha_e + \alpha_i + \alpha_d \, . \tag{2.7}$$

Where α_e, α_i, α_d are electronic, ionic and permanent dipole contribution, respectively. The dependence of the molecular polarization and of the relative permittivity on the frequency of the applied field constitute the phenomenon of dispersion, which needs deeply the atomic theory of matter for an adequate

treatment. But in [22, 8], the Lorentz model of an atom gives a simplified model of a dispersing medium and explicit dependence of the complex relative permittivity $\underline{\epsilon}_r$ on frequency.

In the general characterization of lossy dielectrics, the complex relative permittivity $\underline{\epsilon}_r$ is defined as:

$$\underline{\epsilon} = \epsilon_0 \underline{\epsilon}_r = \epsilon_0 \left(\epsilon' - j\epsilon''\right) = \epsilon_0 \epsilon' \left(1 - j\epsilon''/\epsilon'\right) = \epsilon_0 \epsilon' \left(1 - j\tan\delta\right) . \tag{2.8}$$

Where ϵ' is the ability of the material to be polarized by the external electric field, and ϵ'' and $\tan\delta$ are the loss factor and loss tangent, respectively. The loss tangent quantifies the efficiency with which the electromagnetic energy is converted to heat.

The molecular polarization contributes to ϵ' and ϵ'' in a manner shown by the electronic and ionic resonances pictured as well as by dipole orientation and relaxation for a hypothetical dielectric in **Figure 2.1**. In case of ionic and electronic contribution, the lossy part (near resonance) goes through a peak. The contribution to ϵ' from a given resonance (like the reactance of the tuned circuit [22, Chap. 11]) has peaks of the opposite sign on either side of the resonance. These contribution plays no part at frequencies of interest to this work.
The dynamic response of the permanent dipole contribution to permittivity is different in that the force opposing complete alignment of the dipoles in the direction of the applied field is from thermal effects. It acts as a viscous force and the dynamic response is "overdamped" and produce smooth decrease in ϵ along with a peak of absorption **(Figure 2.1)**. Since this contribution is depend to a significant extent upon frequency and temperature, the next paragraph discusses in detail about the dielectric properties of polar materials like water at millimeter-frequencies.

Dielectric property of water at mm-frequencies

As it is explained above, the knowledge of the dielectric properties of lossy materials, of which water is an example, is important in the study of millimeter-wave propagation. From this point of view the observation of dielectric properties of water at different temperatures including supercooled water is of interest, since water in these state often occurs in rain, slushes, ice and clouds from which radar signal may be attenuated.

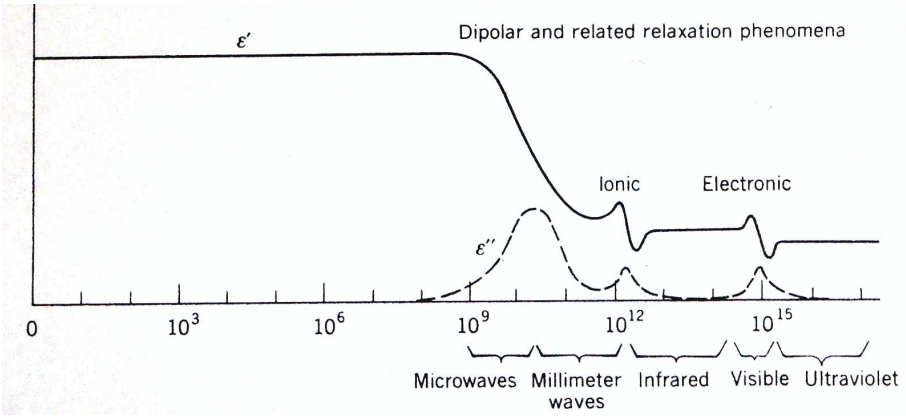

Figure 2.1: Frequency response of permittivity and loss factor for a hypothetical dielectric showing various contributing phenomena in a very wide frequency spectrum, Source: [22, p. 670].

From theoretical and experimental analysis on polar liquids [21], it has been found possible to describe the dielectric properties of water in terms of dipole rotation and relaxation, at any rate for wavelengths of a few millimetres and greater. Debye, in his original theory, supposed that the molecular dipoles could be envisaged as tiny spheres, the rotation of which was opposed by forces related by Stockes's law to the macroscopic viscosity η of the surrounding medium, and he deduced that

$$\tau = \frac{4\pi\eta a^3}{kT} \,, \tag{2.9}$$

where a is the molecular radius, k is the Boltzmann's constant, T is the absolute temperature and τ being the relaxation time, known as a measure of the time required for dipole to rotate. Also, the relaxation time τ can be considered as the delay for the dipole to respond to the field change, or for reversion after disorientation. Further approaches to the problem of dipole relaxation have involved also by Fröhlich [23] and Eyring [24].

The Authors Saxton and Lane [25] have described measurements of the dielectric properties of pure polar liquids (water, methyl and ethyl alcohols) at wavelengths of 6.2 mm, 1.24 cm and 3.2 cm over the temperature range -8 to 50 $^{\circ}C$. Measurements have all been made using a method involving

the observation of the attenuation in transmission through wave guides of differing cross-section dimensions containing the liquid. The complex relative dielectric constant $\underline{\epsilon}_r$ of a medium is related to the refractive index n and absorption coefficient κ as follows:

$$\underline{\epsilon}_r = \epsilon' - j\epsilon'' = (n - j\kappa)^2 \, . \tag{2.10}$$

One could then determine both ϵ' and ϵ'', and therefore also refractive index n and the absorption coefficient κ, for water from these measurements of the rate of attenuation in transmission through two wave guides of suitably chosen cross-section dimension. According to (2.9), τ varies with temperature in a manner which can be obtained from the well-known Debye expression for the dielectric constant of a polar medium in a time-dependent fields:

$$\epsilon' = \epsilon_\infty + \frac{\epsilon_s - \epsilon_\infty}{1 + (w\tau)^2} \, , \tag{2.11}$$

$$\epsilon'' = \frac{(\epsilon_s - \epsilon_\infty)\, w\tau}{1 + (w\tau)^2} \, . \tag{2.12}$$

In equations (2.11) and (2.12) ϵ_s is the relative permittivity measured at low frequencies (or static dielectric constant), ϵ_∞ is that part of the dielectric constant due to the electronic and atomic polarizations, $w = 2\pi f$, where f is the frequency. The measurements given in [25] have made it possible to find a single value of $\epsilon_\infty = 4.9$, substantially independent of temperature, and a single relaxation time for any given temperature which will satisfactorily account for the dielectric properties of water at millimetre and centimetre wavelengths. In addition, it has been established that agreement between theory and experiment is satisfactory down to a wavelength of 6 mm, and also shown that the dielectric properties of water vary in a continuous manner through the normal freezing-point ($0°$ C) into the supercooled state down to temperatures of the order of -8 $°C$. Based on the value τ and measured data of ϵ_s (see **Table 2.1**), the components of the complex relative permittivity of pure water and its corresponding loss tangent have been calculated for micro- and millimeter-wave range using (2.11), (2.12) and (2.8).

Results are provided to **Figure 2.2** for a temperature of $20°$ C. The dielectric loss factor ϵ'' increases to a maximum at the critical frequency $w\tau = 1 \Rightarrow f_c = \frac{1}{2\pi\tau}$, where the first derivation of (2.12) gets minimum. For water at $20°$ C and $\tau = 10.1$ ps, the loss factor reaches its maximum

Table 2.1: Relaxation time (τ) in water ($\epsilon_\infty = 4.9$), Source: [25].

temperature (°C)	ϵ_s	τ (ps)
-10	92.30 (extrap.)	27.50 (extrap.)
0	88.20	18.70
10	84.20	13.60
20	80.40	10.10
30	76.70	7.50
40	73.10	5.90
50	69.80	4.70

($\epsilon'' = 37.75$) at $f_c = 15.8\ GHz$ and starts to decrease smoothly with the frequency. At the same time, ϵ' falls rapidly from its original value $\epsilon_s = 80.4$ and approaches gradually to ϵ_∞. As a consequence, the loss tangent gets to its maximum ($tan\delta = 1.9$) at a frequency, higher than f_c with a factor $\sqrt{\frac{\epsilon_s}{\epsilon_\infty}}$, of about 64 GHz.

The temperature dependence of the complex relative permittivity and its loss factor for pure water at constant frequency (e.g. 76.5 GHz) is also given in **Figure 2.3** in the temperature range of -10 to 50 $°C$. It is calculated from the data, given in **Table 2.1**.

According to [26], anomalous dielectric behavior of water is generally found over a range of frequencies between about 2 and 100 GHz. The shifts in the dielectric properties with temperature gives rise to maxima in the temperature behavior at constant frequency. As the temperature increases, the strength and extent of the hydrogen bonding both decrease. This

1. lowers both the static and optical dielectric permittivities,
2. lessens the difficulty for the movement dipole and so allows the water molecule to oscillate at higher frequencies, and
3. reduces the drag to the rotation of the water molecules, so reducing the friction and hence the dielectric loss.

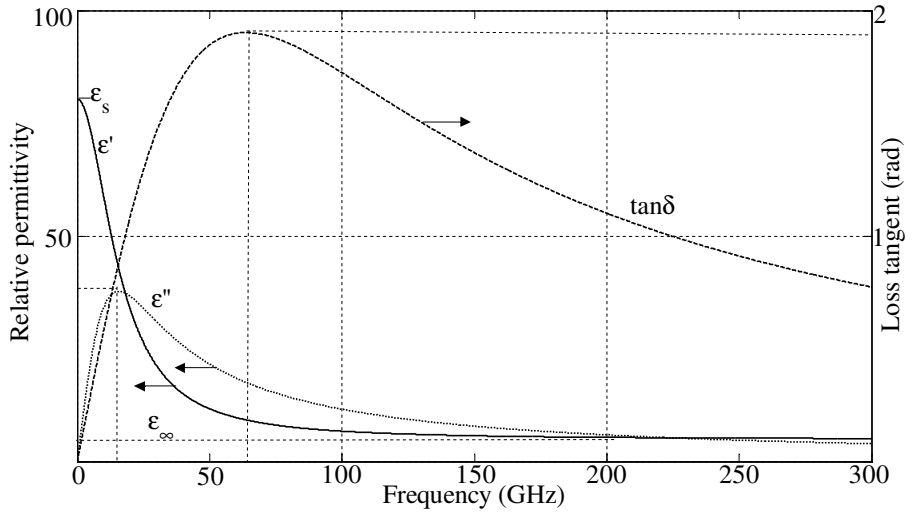

Figure 2.2: The complex dielectrical properties of water at 20 $°C$ versus frequency at micro and millimeter waves.

So, extrapolated results in [27] indicate a decreasing trend of the dielectric properties with increasing temperature beyond the point of maxima. This point of maxima for 76.5 GHz may occur at temperature around 70° C. Thus, **Figure 2.3** shows that the real (ϵ') and/or the imaginary (ϵ'') part of the complex dielectric constant increase (in different manner) with temperature. The loss tangent reaches its maximum at about 20 $°C$, which implies that pure water absorbs its maximum energy for the 76.5 GHz signal at room temperature, having strong impact on radar sensors at that frequency.

Dielectric property of salty water at mm-frequencies

Dissolved salt depresses the dielectric constant dependent on its concentration (C) and the average hydration number of the individual ions (H_N)

$$\epsilon' = \epsilon_\infty + \frac{\epsilon_s - 2H_N C - \epsilon_\infty}{1 + (w\tau)^2} \ . \tag{2.13}$$

Salt decreases the natural structuring of the water, so reducing the static dielectric permittivity in a similar manner to increased temperature [27].

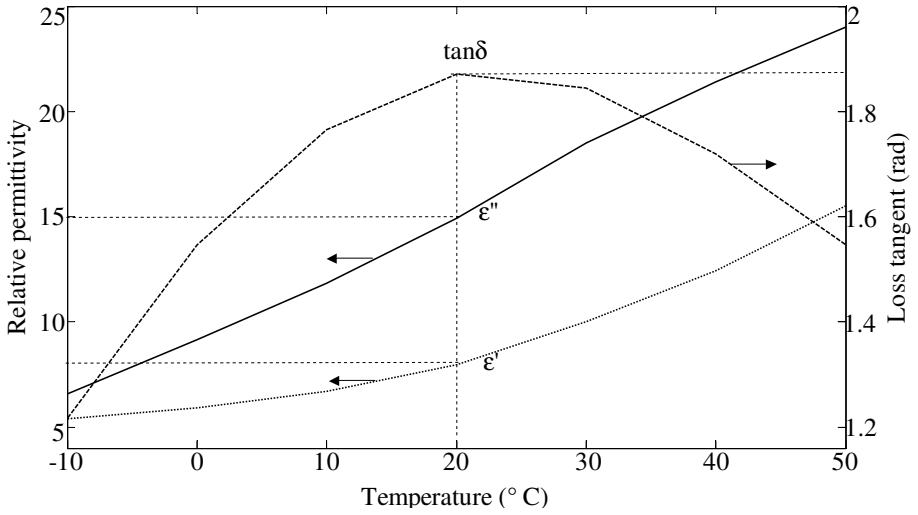

Figure 2.3: The complex dielectrical properties of water at 76.5 GHz versus temperature.

The dielectric loss is increased by a factor that depends on the conductivity (Λ), concentration and frequency

$$\epsilon'' = \frac{(\epsilon_s - 2H_N C - \epsilon_\infty)\, w\tau}{1 + (w\tau)^2} + \frac{\Lambda C}{w\epsilon_0}\,. \tag{2.14}$$

It increases with rise in temperature and decreasing frequency. According to [27], at frequencies below 30 GHz the ions are able to respond and move with the changing potential so producing frictional heat and increasing the loss factor ϵ''. Whereas at frequency above 30 GHz, there is no significant change with that of pure water.

Dielectric property of ice at mm-frequencies

Bound water and ice have critical frequencies at about 10 MHz (τ about 16 ns) with raised static dielectric permittivities (ϵ_s). At higher frequencies in th millimeter-wave region, ice has low dielectric permittivity (e.g. ice: $\epsilon_\infty = 3.1$, $\epsilon_s = 97.5$ [28]; water: $\epsilon_\infty = 4.9$, $\epsilon_s = 88.2$ at $0°\ C$), and is almost transparent, absorbing little energy. This is particularly noticed from labo-

ratory measurements, which have been made and published by a number of researchers at millimeter and sub-millimeter wavelengths [2, 29].

2.2 Wave propagation in stratified media

The subject of stratified media has been very extensively treated in the scientific literature and many schemes for the computation of its optical effects have been proposed [30, 8, 31, 22]. In this section, based on the basic properties of the electromagnetic filed [8, Chap. 1], the theory of stratified media is discussed for treating a model having small number of layers. Some special cases of particular interest of this work is also considered in detail. Only dielectric stratified media will be treated in this section. The extension of the analysis to lossy media will be described in Chapter 4, in accordance with the effects of water film on the performance of millimeter wave radar sensors.

The notation introduced in this section will be used throughout this thesis. Cartesian coordinates x, y, z and unit vectors $\mathbf{e}_x$, $\mathbf{e}_y$, $\mathbf{e}_z$ have been chosen. A medium whose properties are constant throughout each plane perpendicular to a fixed direction is called a stratified medium. If the z-axis of a Cartesian reference system is taken along this special direction, then

$$\epsilon = \epsilon(z), \qquad \mu = \mu(z) . \tag{2.15}$$

2.2.1 Reflection and transmission coefficients

Consider a linearly polarized, simple harmonic plane wave (see A) of amplitude E_0 incident upon a stratified medium that extends from $z = 0$ to $z = d_2$ and that is bounded on each side by a homogeneous, semi-infinite medium air (**Figure 2.4**). When an incident plane wave $\mathbf{E}_i$ falls on to a boundary between two homogeneous media of different dielectric properties, it is split into two waves: a transmitted wave proceeding into the second medium and a reflected wave propagated back into the first medium. The existence of these two waves can be demonstrated from the boundary condition, since it is easily seen that these conditions cannot be satisfied without postulating both the transmitted and the reflected wave. Let be tentatively assume that

these waves are also plane so that expression for their directions of propagation and their amplitude shall be driven according to (A.14) and (A.18).

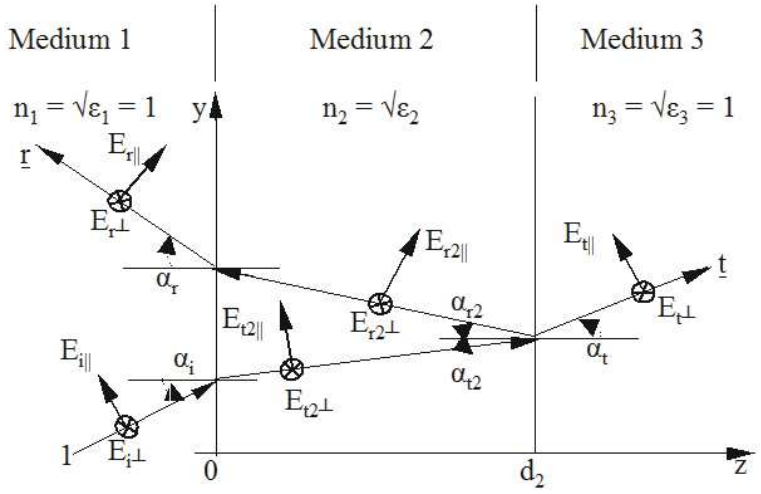

Figure 2.4: Electromagnetic wave propagation through a stratified media.

In **Figure 2.4**, all quantities associated with the incident field will be denoted by the subscript i and those associated with the reflected and transmitted field by the subscript r and t, respectively. Thus $\mathbf{E}_i$, $\mathbf{E}_r$, and $\mathbf{E}_t$ denoted the electric vectors of the incident, reflected and transmitted waves. Similarly, $\mathbf{H}_i$, $\mathbf{H}_r$, and $\mathbf{H}_t$ denote the magnetic vectors of the incident, reflected and transmitted waves. The ϵ_2, μ_2 are the electric permittivity and magnetic permeability of the second medium (pure dielectric). The first and third medium are assumed to be of free space.
Further, let $\mathbf{k}_i$, $\mathbf{k}_r$ and $\mathbf{k}_t$ be the direction of propagation of the incidence, reflected and transmitted waves, and let α_i, α_r and α_t be the angles between $\mathbf{k}_i$, $\mathbf{k}_r$ and $\mathbf{k}_t$-vectors and z-direction

Any arbitrarily polarized plane wave may be resolved into two waves, namely perpendicular ($\mathbf{E}_\perp$) and parallel ($\mathbf{E}_\parallel$) components to the plane of incidence (yz-plane in **Figure 2.4**). These wave components are also known as Transversal Electric Wave (denoted by TE-Wave) and Transversal Magnetic Wave (denoted by TM-Wave), respectively. Since the boundary conditions at a discontinuity surface for these two waves are independent of each other,

they will have different expressions for reflection and transmission of electromagnetic wave in dielectric medium. Therefore, the expression for reflection and transmission factor of electromagnetic wave could be separately treated for perpendicular and parallel components of the propagated wave.
The total reflection and transmission factor will be then obtained by superposition of these results.

Perpendicular Polarized Wave (TE-Wave)

Medium 1: the incident electric field vector $\mathbf{E}_{i\perp}$ is directed towards the x-axis of the Cartesian coordinate system and makes an angle of incidence α_i between its propagation direction $\mathbf{k}_i$ and the z-axis of the incidence plane (**Figure 2.4**). So, the normal and radius vector of this incidence field will be

$$\eta_i = \mathbf{e}_y \sin\alpha_i + \mathbf{e}_z \cos\alpha_i \ , \tag{2.16}$$

and

$$\mathbf{r}_i = \mathbf{e}_y y + \mathbf{e}_z z \ . \tag{2.17}$$

Substituting equations (2.16) and (2.17) into the first term of equations (A.23) and (A.24) give the incident electric and magnetic field vectors for the first medium:

$$\mathbf{E}_{i\perp} = \mathbf{e}_x E_0 e^{-jk(y\sin\alpha_i + z\cos\alpha_i)} \ , \tag{2.18}$$

$$\mathbf{H}_{i\perp} = (\mathbf{e}_y \cos\alpha_i - \mathbf{e}_z \sin\alpha_i)\, \frac{E_0}{Z_0} e^{-jk(y\sin\alpha_i + z\cos\alpha_i)} \ . \tag{2.19}$$

The reflected wave from the boundary of the first and second medium makes an angle of reflection α_r with the negative z-axis of the incidence plane by its propagation back into the first medium so that it obtains a normal vector

$$\eta_r = \mathbf{e}_y \sin\alpha_r - \mathbf{e}_z \cos\alpha_r \ . \tag{2.20}$$

According to the second term of equations (A.23) and (A.24), the reflected electric and magnetic field vectors for the first medium will be

$$\mathbf{E}_{r\perp} = \mathbf{e}_x \underline{r}_\perp E_0 e^{-jk(y\sin\alpha_r - z\cos\alpha_r)} \ , \tag{2.21}$$

and

$$\mathbf{H}_{r\perp} = -(\mathbf{e}_y \cos\alpha_r + \mathbf{e}_z \sin\alpha_r) \frac{\underline{r}_\perp E_0}{Z_0} e^{-jk(y\sin\alpha_r - z\cos\alpha_r)} \ , \tag{2.22}$$

where $\underline{r}_\perp$ is the complex reflection coefficient.

Medium 2: the transmitted wave across the boundary of medium 1 and 2 makes an angle of transmission α_{t2} with respect to the positive z-axis by its propagation toward medium 3 so that it obtain the following normal and field vectors

$$\eta_{t2} = \mathbf{e}_y \sin\alpha_{t2} + \mathbf{e}_z \cos\alpha_{t2} \ , \tag{2.23}$$

$$\mathbf{E}_{t2\perp} = \mathbf{e}_x \underline{A}_{t2\perp} E_0 e^{-jkn_2(y\sin\alpha_{t2} + z\cos\alpha_{t2})} \ , \tag{2.24}$$

$$\mathbf{H}_{t2\perp} = (\mathbf{e}_y \cos\alpha_{t2} - \mathbf{e}_z \sin\alpha_{t2}) \frac{n_2 \underline{A}_{t2\perp} E_0}{Z_0} e^{-jkn_2(y\sin\alpha_{t2} + z\cos\alpha_{t2})} \ , \tag{2.25}$$

where n_2 is the index of refraction of the second medium and $\underline{A}_{t2\perp}$ is a complex amplitude of the $\mathbf{E}_{t2}$ that splits into reflected and transmitted wave at transition of the medium 2 and 3. The reflected wave, propagate back to the medium 2, makes an angle of reflection α_{r2} with z-axis and will gain a normal and field vectors of

$$\eta_{r2} = \mathbf{e}_y \sin\alpha_{r2} - \mathbf{e}_z \cos\alpha_{r2} \ , \tag{2.26}$$

$$\mathbf{E}_{r2\perp} = \mathbf{e}_x \underline{A}_{r2\perp} E_0 e^{-jkn_2(y\sin\alpha_{r2} - z\cos\alpha_{r2})} \ , \tag{2.27}$$

$$\mathbf{H}_{r2\perp} = -(\mathbf{e}_y \cos\alpha_{r2} + \mathbf{e}_z \sin\alpha_{r2}) \frac{n_2 \underline{A}_{r2\perp} E_0}{Z_0} e^{-jkn_2(y\sin\alpha_{r2} - z\cos\alpha_{r2})} \ , \tag{2.28}$$

where $\underline{A}_{r2\perp}$ is the complex amplitude of the reflected electric field $\mathbf{E}_{r2}$.

Medium 3: it includes only the wave that refracts through the boundary of medium 2 and 3 and continue to propagate in the direction of α_t with respect to the positive z-axis. Its normal and field vectors will be then

$$\eta_t = \mathbf{e}_y \sin\alpha_t + \mathbf{e}_z \cos\alpha_t \ , \tag{2.29}$$

$$\mathbf{E}_{t\perp} = \mathbf{e}_x \underline{t}_\perp E_0 e^{-jk(y\sin\alpha_t + z\cos\alpha_t)} \ , \tag{2.30}$$

$$\mathbf{H}_{t\perp} = (\mathbf{e}_y \cos\alpha_t - \mathbf{e}_z \sin\alpha_t) \frac{\underline{t}_\perp E_0}{Z_0} e^{-jk(y\sin\alpha_t - z\cos\alpha_t)} \ , \tag{2.31}$$

where $\underline{t}_\perp$ is a complex transmission coefficient for medium 2.

Equations for electric and magnetic field vectors of medium 1 to 3 are stated due to theirs continuous physical properties, characterized by the ϵ and μ. These properties change abruptly at the transition between the media (**Figure 2.4**). As a result, the vectors **E**, **H**, **D** and **B** may then be

expected also to become discontinuous, while the charge and current density will degenerate into corresponding surface quantity. Note that the electric displacement **D** and the magnetic induction **B** are known as the second set of vectors, which describe the effects of the field on material objects (see A). Relations from boundary conditions, describing the transitions across such discontinuity surfaces, will be therefore used as follows [8, Chap. 1]. The tangential component of the electric and magnetic field vectors are continuous across the surface. Hence, it gives at the boundary where $z = 0$:

$$\mathbf{E}_{i\perp}(0) + \mathbf{E}_{r\perp}(0) = \mathbf{E}_{t2\perp}(0) + \mathbf{E}_{r2\perp}(0) \ , \tag{2.32}$$

$$\mathbf{H}_{i\perp y}(0) + \mathbf{H}_{r\perp y}(0) = \mathbf{H}_{t2\perp y}(0) + \mathbf{H}_{r2\perp y}(0) \ . \tag{2.33}$$

Where the index y in (2.33) implies the y-component of the magnetic vector that is tangential to the y-x plane boundary whereas the z-component of the magnetic vector is normal to the y-x plane boundary.
Substituting equations (2.18), (2.21), (2.24), (2.27) into equation (2.32) and equations (2.19), (2.22), (2.25), (2.28) into equation (2.33) yield

$$e^{-jky\sin\alpha_i} + \underline{r}_\perp e^{-jky\sin\alpha_r} = \underline{A}_{t2\perp} e^{-jkn_2 y\sin\alpha_{t2}} + \underline{A}_{r2\perp} e^{-jkn_2 y\sin\alpha_{r2}} \ , \tag{2.34}$$

and

$$\begin{aligned} \mathbf{e}_y \left(\cos\alpha_i e^{-jky\sin\alpha_i} - \underline{r}_\perp \cos\alpha_r e^{-jky\sin\alpha_r}\right) = \\ \mathbf{e}_y n_2 \left(\underline{A}_{t2\perp}\cos\alpha_{t2} e^{-jkn_2 y\sin\alpha_{t2}} - \underline{A}_{r2\perp}\cos\alpha_{r2} e^{-jkn_2 y\sin\alpha_{r2}}\right) \ . \end{aligned} \tag{2.35}$$

In a homogeneous medium, since the incident and reflected wave normals are in the plane of incidence, the law of reflection can be applied to the above equations. That is, regarding to **Figure 2.4**

$$\alpha_i = \alpha_r, \qquad \alpha_{t2} = \alpha_{r2} = \alpha_2 \ . \tag{2.36}$$

Also, equations (2.34) and (2.35) become true for the whole y-axis and show that the refracted wave normal is in the plane of incidence, as well

$$\sin\alpha_i = n_2 \sin\alpha_2 \ . \tag{2.37}$$

Equation (2.37) is known as the law of refraction (or Snell's law) [22, 8]. Similarly, the continuity of tangential components of the electric and magnetic field vectors at the transition between medium 2 and 3 ($z = d_2$) demands

$$\mathbf{E}_{t2\perp}(d_2) + \mathbf{E}_{r2\perp}(d_2) = \mathbf{E}_{t\perp}(d_2) \ , \tag{2.38}$$

and

$$\mathbf{H}_{t2\perp y}(d_2) + \mathbf{H}_{r2\perp y}(d_2) = \mathbf{H}_{t\perp y}(d_2)\ . \tag{2.39}$$

The following expressions will be obtained by substituting equations (2.24), (2.27), (2.30) into equation (2.38) and equations (2.25), (2.28), (2.31) into equation (2.39), and by considering the law of reflection (2.36)

$$\left(\underline{A}_{t2\perp} e^{-jkn_2 d_2 \cos\alpha_2} + \underline{A}_{r2\perp} e^{jkn_2 d_2 \cos\alpha_2}\right) e^{-jkn_2 y \sin\alpha_2} = \underline{t}_\perp e^{-jk(y\sin\alpha_t + d_2\cos\alpha_t)}, \tag{2.40}$$

and

$$\mathbf{e}_y n_2 \cos\alpha_2 \left(\underline{A}_{t2\perp} e^{-jkn_2 d_2 \cos\alpha_2} - \underline{A}_{r2\perp} e^{jkn_2 d_2 \cos\alpha_2}\right) e^{-jkn_2 y \sin\alpha_2} = \mathbf{e}_y \cos\alpha_t \underline{t}_\perp e^{-jk(y\sin\alpha_t - d_2\cos\alpha_t)}\ . \tag{2.41}$$

The fulfillment of the above two equation along the y-axis requires the relation

$$n_2 \sin\alpha_2 = \sin\alpha_t\ , \tag{2.42}$$

and it yields in combination with (2.37) the general law of refraction for **Figure 2.4**

$$\sin\alpha_i = n_2 \sin\alpha_2 = \sin\alpha_t\ . \tag{2.43}$$

Equation (2.43) implies that the wave, passing through **Figure 2.4**, continues its propagation in medium 3 with the same direction of propagation as the incident wave in the first medium, i.e. $\alpha_i = \alpha_t$.
Substituting the expressions (2.36) and (2.43) into (2.34), (2.35), (2.40) and (2.41) yields a simplified linear equation system from which the four unknown complex quantities $\underline{r}_\perp$, $\underline{A}_{t2\perp}$, $\underline{A}_{r2\perp}$ and $\underline{t}_\perp$ may be obtained.

$$1 + \underline{r}_\perp = \underline{A}_{t2\perp} + \underline{A}_{r2\perp}\ , \tag{2.44}$$

$$\cos\alpha_i\,(1 - \underline{r}_\perp) = n_2 \cos\alpha_2\,(\underline{A}_{t2\perp} - \underline{A}_{r2\perp})\ , \tag{2.45}$$

$$\underline{A}_{t2\perp} e^{-jkn_2 d_2 \cos\alpha_2} + \underline{A}_{r2\perp} e^{jkn_2 d_2 \cos\alpha_2} = \underline{t}_\perp e^{-jkd_2\cos\alpha_t}\ , \tag{2.46}$$

$$n_2 \cos\alpha_2 \left(\underline{A}_{t2\perp} e^{-jkn_2 d_2 \cos\alpha_2} - \underline{A}_{r2\perp} e^{jkn_2 d_2 \cos\alpha_2}\right) = \underline{t}_\perp \cos\alpha_t e^{-jkd_2\cos\alpha_t}\ . \tag{2.47}$$

These linear equation systems, (2.44) to (2.47), can be easily extended for stratified media with more than three layers, and used to formulate equations for the total reflection and total transmission coefficients, as it is used

in § 4.1. The relationship between the number of layers (NL) and the number of linear equation (NLE) to be obtained is given by $NLE = 2 * NL - 2$.

Equations (2.44) to (2.47) may be conveniently expressed in terms of $r_\perp$ and $t_\perp$ associated with the perpendicular components of the reflection and transmission coefficients of the second medium in **Figure 2.4**. In terms of these expression, the formula for $r_\perp$ and $t_\perp$ become

$$\underline{r}_\perp = \frac{j\left(\frac{Q}{n_2} - \frac{n_2}{Q}\right)\sin\delta}{2cos\ \delta + j\left(\frac{Q}{n_2} + \frac{n_2}{Q}\right)\sin\delta}\,, \tag{2.48}$$

$$\underline{t}_\perp = \frac{2e^{j\delta_0}}{2\cos\delta + j\left(\frac{Q}{n_2} + \frac{n_2}{Q}\right)\sin\delta}\,, \tag{2.49}$$

where

$$Q = \frac{\cos\alpha_i}{\cos\alpha_2} = \frac{\cos\alpha_i}{\sqrt{1 - \frac{\sin^2\alpha_i}{\epsilon_2}}}\,, \tag{2.50}$$

is the relation between angle of incidence and angle of transmission, and

$$\delta = kn_2d_2\cos\alpha_2 = kd_2\sqrt{n_2^2 - \sin^2\alpha_i}, \qquad \delta_0 = kd_2\cos\alpha_i, \tag{2.51}$$

are phase terms. The expressions in (2.48) and (2.49) show that the complex reflection and transmission coefficients of a stratified medium depend on the angle of incidence, the electrical properties of the material, the frequency of the incident wave and the thickness of the stratified medium. That means, these expressions may be utilized to study the effects of materials, such as ice- and water film on the antenna surface of automotive radar, on the radio wave propagation (see chapter 4).
The phase terms in (2.48) and (2.49) are known as phase change on reflection and on transmission, whilst the magnitudes represent the absolute value of the reflected and transmitted fields. Squaring the magnitude in (2.48) and (2.49) give the reflection and transmission coefficient of the power.

$$R_\perp = |\underline{r}_\perp|^2 = \frac{\left(Q^2 - \epsilon_2\right)^2\sin^2\delta}{4\epsilon_2Q^2 + \left(Q^2 - \epsilon_2\right)^2\sin^2\delta}, \tag{2.52}$$

$$T_\perp = |\underline{t}_\perp|^2 = \frac{4\epsilon_2}{4\epsilon_2 + \left(\frac{Q^2-\epsilon_2}{Q}\right)^2\sin^2\delta}\,, \tag{2.53}$$

where $R_\perp$ and $T_\perp$ are called the reflectivity and transmissivity, associated with polarization in the perpendicular direction, respectively. It can easily be verified that, in agreement with the law of conservation of energy,

$$R_\perp + T_\perp = 1 \,. \tag{2.54}$$

According to (2.52), the dielectric film in **Figure 2.4** will be reflection free only by $\sin\delta = 0$, i.e for the following thicknesses of the stratified medium (see (2.51))

$$d_2 = \frac{m}{2}\frac{\lambda}{\sqrt{\epsilon_2 - \sin^2\alpha_i}}, \qquad m = 0, 1, 2, ... \tag{2.55}$$

In such cases, the amount of the power of the incident field transmit completely to the third semi-infinite medium. The maximum reflection and minimum transmission are to expect by $\sin\delta = 1$, i.e. for the film with the thicknesses of

$$d_2 = \frac{2m+1}{4}\frac{\lambda}{\sqrt{\epsilon_2 - \sin^2\alpha_i}}, \qquad m = 0, 1, 2, ... \tag{2.56}$$

According to (2.52), (2.53) and (2.50), the magnitude for the maximum reflection and minimum transmission will be

$$|\underline{r}_\perp|_{max} = \frac{\epsilon_2 - Q^2}{\epsilon_2 + Q^2} = \frac{\epsilon_2 - 1}{\epsilon_2 + 1 - 2\sin^2\alpha_i}\,, \tag{2.57}$$

$$|\underline{t}_\perp|_{min} = \frac{2\sqrt{\epsilon_2}Q}{\epsilon_2 + Q^2} = \frac{2\cos\alpha_i\sqrt{\epsilon_2 - \sin\alpha_i}}{\epsilon_2 + 1 - 2\sin^2\alpha_i}\,. \tag{2.58}$$

Parallel Polarized Wave (TM Wave)

In case of TM wave, the electric field vector of the incident wave $\mathbf{E}_{i\perp}$ (2.18) rotates an its wave normal by 90° and become the following direction of polarization in the incidence plane

$$\eta_i \times \mathbf{e}_x = \mathbf{e}_y \cos\alpha_i - \mathbf{e}_z \sin\alpha_i \,. \tag{2.59}$$

Therefore, it has been denoted in Fig 2.4 by $E_{\|}$. The corresponding magnetic field vector will be then, according to A.19, polarized in the perpendicular (or positive x) direction to the plane of incidence. It is then referred as transversal magnetic (TM) wave.

The corresponding formula for reflection and transmission coefficients of TM wave are immediately obtained by using the similar strategy and taking same procedures like the TE wave. Therefore, the tangential component of the electric and magnetic field vectors, are continuous across the surface, given at the boundary where $z = 0$:

$$\left(1 + \underline{r}_{\|}\right) \cos \alpha_i = \left(\underline{A}_{t2\|} + \underline{A}_{r2\|}\right) \cos \alpha_2 \ , \tag{2.60}$$

$$1 - \underline{r}_{\|} = n_2 \left(\underline{A}_{t2\|} - \underline{A}_{r2\|}\right) \ , \tag{2.61}$$

and at the boundary $z = d_2$

$$\cos \alpha_2 \left(\underline{A}_{t2\|} e^{-j\delta} + \underline{A}_{r2\|} e^{j\delta}\right) = \underline{t}_{\|} \cos \alpha_i e^{-j\delta_0} \ , \tag{2.62}$$

$$n_2 \left(\underline{A}_{t2\|} e^{-j\delta} - \underline{A}_{r2\|} e^{j\delta}\right) = \underline{t}_{\|} e^{-j\delta_0} \tag{2.63}$$

Where $\underline{r}_{\|}$, $\underline{t}_{\|}$ are the complex reflection and transmission coefficients, associated with the parallel polarized wave components of the stratified medium, and $\underline{A}_{t2\|}$, $\underline{A}_{r2\|}$ are the complex amplitudes for the forward and backward propagated wave in the stratified medium of **Figure 2.4**. The required $\underline{r}_{\|}$ and $\underline{t}_{\|}$ may then be obtained from the linear equation systems (2.60) to (2.63) with the help of (2.50) and (2.51)

$$\underline{r}_{\|} = \frac{j\left(\frac{1}{Qn_2} - Qn_2\right)\sin \delta}{2\cos \delta + j\left(\frac{1}{Qn_2} + Qn_2\right)\sin \delta} \ , \tag{2.64}$$

$$\underline{t}_{\|} = \frac{2e^{j\delta_0}}{2\cos \delta + j\left(\frac{1}{Qn_2} + Qn_2\right)\sin \delta} \ . \tag{2.65}$$

The above expressions show that $\underline{r}_{\|}$ and $\underline{t}_{\|}$ can be obtained from $\underline{r}_{\perp}$ and $\underline{t}_{\perp}$ if the term Q in (2.48) and (2.49) is substituted with $\frac{1}{Q}$, which implies specially for the $\underline{r}_{\|}$ a possible change in phase. According to (2.64), the reflection coefficient will be zero not only for $\sin \delta = 0$ but also for $\epsilon Q^2 = 1$.

It will be achieved if the wave is incident under the so called polarizing or Brewster angle, denoted by α_B and will be determine by substituting Q from (2.50):

$$\alpha_B = \arctan \sqrt{\epsilon_2} \, . \tag{2.66}$$

The electric vector of the reflected wave has no component in the plane of incidence at α_B and it will appear again for angle of incidence beyond α_B with a change in phase or polarization with respect to that of the incidence wave [8, p. 43-49] [32, §. 21-4].
Similar to $r_\perp$ and $t_\perp$, the maximum reflection and minimum transmission coefficients of the TM wave are to expect by $\sin\delta = 1$, i.e. for the thicknesses of the film given by (2.56). The expression for these terms can be hold then from (2.64) and (2.65):

$$\left|\underline{r}_\parallel\right|_{max} = \frac{|\epsilon_2 Q^2 - 1|}{\epsilon_2 Q^2 + 1} = \frac{\left|\epsilon_2 \left(\epsilon_2 - 1\right) - \left(\epsilon_2^2 - 1\right)\sin^2\alpha_i\right|}{\epsilon_2 \left(\epsilon_2 + 1\right) - \left(\epsilon_2^2 + 1\right)\sin^2\alpha_i} \, , \tag{2.67}$$

$$\left|\underline{t}_\parallel\right|_{min} = \frac{2\sqrt{\epsilon_2} Q}{\epsilon_2 Q^2 + 1} = \frac{2\epsilon_2 \cos\alpha_i \sqrt{\epsilon_2 - \sin^2\alpha_i}}{\epsilon_2 \left(\epsilon_2 + 1\right) - \left(\epsilon_2^2 + 1\right)\sin^2\alpha_i} \, . \tag{2.68}$$

The reflectivity $R_\parallel$ and transmissivity $T_\parallel$, associated with polarization in the parallel direction, expressed in terms of the magnitude of $\underline{r}_\parallel$ and $\underline{t}_\parallel$ as follows:

$$R_\parallel = \left|\underline{r}_\parallel\right|^2 = \frac{\left(\epsilon_2 Q - \frac{1}{Q}\right)^2 \sin^2\delta}{4\epsilon_2 + \left(\epsilon_2 Q - \frac{1}{Q}\right)^2 \sin^2\delta} \, , \tag{2.69}$$

$$T_\parallel = \left|\underline{t}_\parallel\right|^2 = \frac{4\epsilon_2}{4\epsilon_2 + \left(\epsilon_2 Q - \frac{1}{Q}\right)^2 \sin^2\delta} \, . \tag{2.70}$$

Analogous to (2.54), expression (2.69) and (2.70) verifies also the fulfillment of law of conservation of energy for a dielectric medium:

$$R_\parallel + T_\parallel = 1 \, . \tag{2.71}$$

According to **Figure 2.4**, the **E** vector of the incident wave that is the resultant electric field vector of $\mathbf{E}_{i\parallel}$ and $\mathbf{E}_{i\perp}$, makes an angle of ψ with the plane of incidence, yz-plane. This angle is known as a polarization angle for the linear polarized wave **E**. Finally, the total reflectivity R and transmissivity

T of the two secondary fields, i.e. $\mathbf{E}_r$ and $\mathbf{E}_t$, may be expressed in terms of the polarization angle ψ and $R_\perp$, $R_\parallel$ and $T_\perp$, $T_\parallel$, respectively [8, p. 43-49]:

$$R = R_\parallel \cos^2\psi + R_\perp \sin^2\psi \,, \tag{2.72}$$

$$T = T_\parallel \cos^2\psi + T_\perp \sin^2\psi \,. \tag{2.73}$$

For normal incidence, i.e. for $\alpha_i = 0$, the distinction between the parallel and perpendicular components disappears, and one has from (2.52), (2.69) and (2.53), (2.70)

$$R = R_\parallel = R_\perp = \frac{(\epsilon_2 - 1)^2 \sin^2\delta}{4\epsilon_2 + (\epsilon_2 - 1)^2 \sin^2\delta} \,, \tag{2.74}$$

$$T = T_\parallel = T_\perp = \frac{4\epsilon_2}{4\epsilon_2 + (\epsilon_2 - 1)^2 \sin^2\delta} \,. \tag{2.75}$$

It is to see from (2.74) that the smaller the difference in the dielectric properties of the stratified medium and its surrounding, the less the energy carried away by the reflected wave.

The above results will be generally applied in chapter 4 to observe the significance of effects of materials on the millimeter-wave propagation, when they may be appeared in the propagation path. The relationship between power loss and power transmitted, particularly due to lossy materials on the antenna surface of automotive radars, can be clearly and easily stated using equations (2.74) and (2.75).

2.2.2 Cross-polarization coefficients

The reflected and transmitted wave are described not only by their amplitude and phase, but also by their polarization (see § 2.2.1). One of the most difficult problems connected with propagation of wave through stratified media is the question of what happens to the original polarization of the incident wave after the wave has been reflected and transmitted.

On the basis of theoretical work, Beckmann and Spizzichino showed that a wave reflected in the plane of incidence is not depolarized if the incident wave is polarized either purely vertically or horizontally. Further, on the basis of theoretical studies, it was shown there that a horizontally or

vertically polarized wave is strongly depolarized if it is scattered out of the plane of incidence, for example laterally. All these and a detail treatment of depolarization caused by a surface of arbitrary dielectric property have been illustrated in [33, Chap. 8] and show in the general case a change in polarization must be expected.

The cross-polarization factor uniquely defines the orthogonal polarization to which an electromagnetic wave is subjected. It is useful only if $\mathbf{E}_i$ is linearly polarized. In **Figure 2.4**, the incidence wave $\mathbf{E_i}$ is assumed to be linearly polarized and makes an angle of polarization ψ with the plane of incidence, yz-plane. Its unit vector $\mathbf{e}_0$ lies in the plane, which is stretched out on $\mathbf{e}_x$ and $\eta_i \times \mathbf{e}_x$, and may be expressed in terms of ψ and (2.16)

$$\mathbf{e}_0 = \mathbf{e}_x \cos\psi + (\mathbf{e}_y \cos\alpha_i - \mathbf{e}_z \sin\alpha_i)\sin\psi \ . \tag{2.76}$$

As consequence, the amplitude of the incidence wave E_0, the reflected wave E_r and the transmitted wave E_t may take a form of expression like:

$$E_0 = (E\cos\psi)\,\mathbf{e}_x + (E\sin\psi)\,(\mathbf{e}_y \cos\alpha_i - \mathbf{e}_z \sin\alpha_i) \ , \tag{2.77}$$

$$E_r = (\underline{r}_\perp E\cos\psi)\,\mathbf{e}_x + \left(\underline{r}_\parallel E\sin\psi\right)(\mathbf{e}_y \cos\alpha_i - \mathbf{e}_z \sin\alpha_i) \ , \tag{2.78}$$

$$E_t = (\underline{t}_\perp E\cos\psi)\,\mathbf{e}_x + \left(\underline{t}_\parallel E\sin\psi\right)(\mathbf{e}_y \cos\alpha_i - \mathbf{e}_z \sin\alpha_i) \ . \tag{2.79}$$

As it has been seen in §2.2.1, the reflection coefficients $\underline{r}_\perp$ and $\underline{r}_\parallel$ as well as corresponding transmission coefficients $\underline{t}_\perp$ and $\underline{t}_\parallel$ are the same in amplitude and phase only for a normal incidence, i.e. $\alpha_i = 0$. In all other cases, they are completely different in amplitude and phase. Hence the reflected and transmitted waves are polarized elliptically. The orthogonally polarized electric field $\mathbf{E}_k$ lies in the direction of a unit vector

$$\mathbf{e}_k = \eta_i \times \mathbf{e}_0 \ , \tag{2.80}$$

and obtains the following expression for its reflexion and transmission wave components

$$\mathbf{E}_{rk} = \mathbf{e}_k \cdot E_r, \qquad \mathbf{E}_{tk} = \mathbf{e}_k \cdot E_t \ . \tag{2.81}$$

By substituting (2.78), (2.79), (2.80) into (2.81) and by considering equations (2.16), (2.48), (2.49), (2.64), (2.65), and (2.76), the cross-polarization coefficients for reflection p_{kr} and transmission p_{kt} will be given in relation to the amplitude of the incidence wave E:

$$p_{kr} = \frac{\mathbf{E}_{rk}}{E} = \frac{1}{2}|\sin 2\psi|\left|\underline{r}_\perp - \underline{r}_\parallel\right| \ , \tag{2.82}$$

$$p_{kt} = \frac{\mathbf{E}_{tk}}{E} = \frac{1}{2}|\sin 2\psi|\left|\underline{t}_{\parallel} - \underline{t}_{\perp}\right| . \tag{2.83}$$

According to (2.82) and (2.83), the cross-polarization coefficients will be maximum for a $\psi = 45\,\text{deg}$ linear polarized incidence wave and be minimum (or zero) for a purely parallel polarized ($\psi = 90\,\text{deg}$) or purely perpendicular polarized ($\psi = 0\,\text{deg}$) incidence waves, as mentioned in [33]. For a 45 deg linear polarized incidence wave, (2.82) and (2.83) become then

$$p_{krmax} = \frac{1}{2}\left|\underline{r}_{\perp} - \underline{r}_{\parallel}\right| , \tag{2.84}$$

$$p_{ktmax} = \frac{1}{2}\left|\underline{t}_{\parallel} - \underline{t}_{\perp}\right| . \tag{2.85}$$

There will also no cross-polarization (or depolarization) if $\underline{r}_{\perp} = \underline{r}_{\parallel}$ and/or $\underline{t}_{\perp} = \underline{t}_{\parallel}$, as it may be seen from (2.84) and (2.85). The only important case of this is near normal incidence, i.e. $\alpha_i = 0$ or $\sin\delta = 0$ (see (2.48), (2.64) as well as (2.49), (2.65)). For $\sin^2\delta = 1$, substituting equations (2.57) and (2.67) in (2.84) as well as (2.58) and (2.68) in (2.85) give on the other hand the following general formulas for the maximum cross-polarization coefficients of reflection and transmission

$$p_{krmax} = \left|\frac{\epsilon_2\,(1-Q^4)}{(\epsilon_2+Q^2)(\epsilon_2 Q^2+1)}\right| , \tag{2.86}$$

$$p_{krmax} = \left|\frac{\sqrt{\epsilon_2}\,(\epsilon_2-1)\,Q\,(1-Q^2)}{(1+\epsilon_2 Q^2)(\epsilon_2+Q^2)}\right| . \tag{2.87}$$

For 45 deg linearly polarized incidence wave, these equations show that the cross-polarization is mainly a function of dielectric properties and angle of incidence. Its significance and applicability will be thus examined in the relation with the effects of lossy materials on the electromagnetic wave propagation, specially in Chapter 4 for the identification of water film at the antenna surface of automotive radar sensors.

2.3 Wave propagation and scattering in random media

The propagation and scattering characteristics of a wave in the presence of randomly distributed particles has been exhaustively covered in a number of books [2, 34]. This section thus summarizes only the basic formulations of the scattering problems, which are principally basic for the potential applications in the upcoming chapters of this work.

Random scatterers are random distributions of many particles (or discrete scatterers). Some examples are rain, fog, smog, hail, and other particles in a state of Brownian motion. These media are, in general, randomly varying in time and space so that the amplitude and phase of the waves may also fluctuate randomly in time and space. These random fluctuations and scattering of the waves are important in a variety of practical problems. For example, radar engineers may need to concern themselves with clutter echoes produced by storms, rain, snow, or hail.

Wave propagation and scattering analysis in such random media can be made in two steps. First, by considering the scattering and absorption characteristics of a single scatterer, and second, by considering the characteristics of a wave when many scatterers are distributed randomly. The next section discusses in brief the definitions of scattering amplitude, and absorption and scattering cross-sections.

2.3.1 Scattering and absorption of a wave by a single particle

The single scattering theory is applicable to the waves in a thin diameter distribution of scatterers. This covers many practical situations including radar, lidar, and sonar (sound navigation ranging) applications in various media.

When a single particle is illuminated by a wave, a part of the incident power is scattered out and another part is absorbed by the particle. The characteristics of these two phenomena, scattering and absorption, can be expressed most conveniently by assuming an incident plane wave, discussed

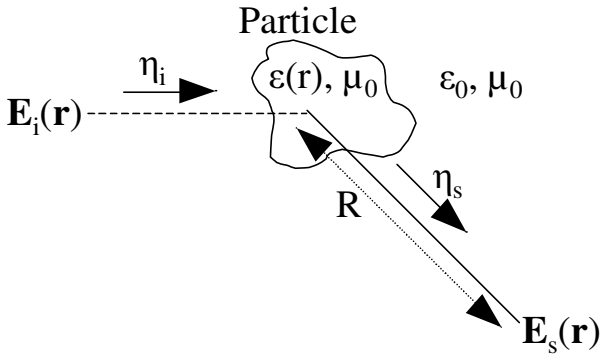

Figure 2.5: A plane wave $\mathbf{E}_i(\mathbf{r})$ is incident upon a dielectric scatterer and the scattered field $\mathbf{E}_s(\mathbf{r})$ is observed in the direction η_s at a distance R, Source: [2, Chap. 2].

in A. Consider a linearly polarized electromagnetic plane wave of unit amplitude propagating in a medium with dielectric constant ϵ_0 and permeability μ_0, with the electric field modified from the first term of (A.23)

$$\mathbf{E}_i(\mathbf{r}) = \mathbf{e}_i e^{-jk\eta_i \cdot \mathbf{r}} , \tag{2.88}$$

where $\mathbf{e}_i$ and η_i are unit vectors in the direction of polarization and propagation respectively and $\mathbf{r}$ is the point of observation. This wave is incident upon a lossy homogeneous particle such as a raindrop or ice particle in **Figure 2.5** whose complex relative dielectric constant $\underline{\epsilon}_r$ is given by (2.10).

The total field, at a distance R from a reference point in the particle, in the direction of a unit vector η_s consists of the incident field $\mathbf{E}_i$ and the field $\mathbf{E}_s$ scattered by the particle. With in a distance $R < D^2/\lambda$ where D is a typical dimension of the particle such as its diameter, the field $\mathbf{E}_s$ has complicated amplitude and phase variations because of interference between contributions from different parts of the particle. So, the observation point $\mathbf{r}$ is said to be in the near field of the particle. When the $R > D^2/\lambda$, however, the scattered field $\mathbf{E}_s$ behaves as a spherical wave and is given, according to [8, § 13.1], by

$$\mathbf{E}_s(\mathbf{r}) = \mathbf{f}(\eta_s, \eta_i)\frac{e^{-jkR}}{R} . \tag{2.89}$$

$\mathbf{f}(\eta_s, \eta_i)$ represents the amplitude, phase and polarization of the scattered wave in the far field in the direction η_s when the particle is illuminated by a

plane wave propagating in the direction η_i with unit amplitude. It is known as the scattering amplitude. It should be also noted that even though the incident wave is linearly polarized, the scattered wave is in general elliptically polarized [35].

The exact expression of the scattering amplitude is the volume integral of the multiplication of the total electric field inside the particle and the relative dielectric property [2, § 2-4]. A quantity which is often of interest in the analysis of scattering experiments is not the scattered field itself but rather the rate at which the energy is scattered and absorbed by the particle. It turns out that there is a close relationship between the rate at which energy is lost from the incident field by these processes and the amplitude of the scattered field in the forward direction (the direction incidence). This relationship is quantitatively expressed by the so called optical cross-section theorem [8, § 13.3 and 13.6.3].

Consider the scattered power flux density S_s at a distance R from the particle in the direction η_s, caused by an incident power flux density S_i. Their ratio σ_d defins the differential scattering cross section of the particle per unit solid angle at distance R. According to equations (A.22), (2.88) and (2.89), this differential scattering cross section can be expressed by

$$\sigma_d(\eta_s, \eta_i) = \lim_{R \to \infty} \left[\frac{R^2 S_s}{S_i} \right] = |\mathbf{f}(\eta_s, \eta_i)|^2 \, . \tag{2.90}$$

The $\sigma_d(\eta_s, \eta_i)$ has the dimensions of area per solid angle. It means, the observed scattered power flux density in the direction of η_s is extended uniformly over one steradian (1 sr) of solid angle about η_s. Then the cross section of a particle which would cause just this amount of scattering would be σ_d, so that σ_d varies with η_s.

In radar applications, the bistatic radar cross section σ_{bi} and the backscattering cross section σ_b (or the radar cross section, RCS) are often used. They are related to σ_d through

$$\sigma_{bi}(\eta_s, \eta_i) = 4\pi\sigma_d(\eta_s, \eta_i), \qquad \sigma_b = 4\pi\sigma_d(-\eta_i, \eta_i) \, . \tag{2.91}$$

Equation (2.91) shows that the observed power flux density in the direction η_s is extended uniformly in all directions from the particle over the entire 4π steradians of solid angle.Then the cross section that would cause this

would be 4π times σ_d for the direction η_s. Next, consider the total observed scattered power at all angles surrounding the particle. The cross section of a particle which would produce this amount of scattering is called the scattering cross section σ_s, and is given in general form

$$\sigma_s = \int_{4\pi} \sigma_d dw = \int_{4\pi} |\mathbf{f}(\eta_s, \eta_i)|^2 \, dw \; . \tag{2.92}$$

Where dw is the differential solid angle.

Next, consider the total power absorbed by the particle. The cross section of a particle that would correspond to this much power is called the absorption cross section σ_a. It can be expressed either in terms of the total flux entering the particle or as the volume integral of the loss inside the particle in **Figure 2.5**. When the magnitude of the incident wave is chosen to be unity ($|E_i| = 1$), the absorption cross section of an inhomogeneous particle is given as follows:

$$\sigma_a = \int_v k\epsilon_r''(\mathbf{r}') \, |\mathbf{E}(r')|^2 dV' \; . \tag{2.93}$$

Equation (2.93) is exact integral representation in terms of imaginary parts of the relative permittivity of the particle and the unknown total field $|\mathbf{E}(r')|$ inside the particle. This field $|\mathbf{E}(r')|$ is not known in general, and therefore (2.93) is not a complete description of the absorption cross section in terms of known quantities. In many practical situations, however, it is possible to approximate $|\mathbf{E}(r')|$ by different known functions depending on the relative permittivity of the particle and the relationship between the particle size and the wavelength. A useful approximate expressions for the absorption cross section σ_a as well as for the scattering amplitude $\mathbf{f}(\eta_s, \eta_i)$ in (2.89) have been given in [2, § 2-5 to 2-8]. The sum of the scattering and the absorption cross sections is called the total cross section σ_t or the extinction cross section of a particle, $\sigma_t = \sigma_s + \sigma_a$.

General properties of cross sections

This section presents an overall view of how scattering and absorption cross sections are related to the geometric cross section, wavelength, and dielectric constant by considering two extreme cases as follows. This has been quite

well explained in [2, § 2-2] on the basis of models of scattering by large particle. The theoretical results show that if the size of a particle is much greater than a wavelength, the total cross section σ_t approaches twice the geometric cross section σ_g of the particle as the size increases, i.e. $\sigma_t \approx 2\sigma_g$.

It is also seen that the total absorbed power, when the particle is very large, cannot be greater than the incident power. Thus, the absorption cross section σ_a approaches a constant somewhat less than the geometric cross section, i.e. $\sigma_a \approx \sigma_g$.

If the size is much smaller than a wavelength, the scattering cross section σ_s is inversely proportional to the fourth power of the wavelength and proportional to the square of the volume of the particle. To show this [2, § 2-5], note that the scattered field E_s is caused by the field in the particle, and thus E_s at a distance R is proportional to the incident field E_i, and the volume V of the scatterer

$$|E_s| = |E_i| \left[(const)\, V/R\right] . \tag{2.94}$$

The constant in (2.94) should be of dimension $(length)^2$, and since it is a function of wavelength, it should be proportional to λ^{-2}. Equating (2.94) to (2.89) gives

$$|E_s| \propto |E_i| \frac{V}{R\lambda^2} \propto |E_i| \frac{|\mathbf{f}(\eta_s, \eta_i)|}{R} . \tag{2.95}$$

Therefore, according to (2.90), $\sigma_s \propto |\mathbf{f}(\eta_s, \eta_i)|^2 \propto V^2/\lambda^4$. These characteristics of a small particle are generally called Rayleigh scattering. The absorption cross section σ_a for a small scatterer is inversely proportional to the wavelength and directly proportional to its volume. Compared with the geometric cross section, curves of the normalized cross section versus the relative size of the particle are shown in **Figure 2.6**.

The salient features are the considerable increase in the normalized total and absorption cross section of the smaller particles towards their maximum constants value as the absorption is increased. The oscillatory curve can be attributed to an interference effect between the direct scattered ray and rays sprayed off due to surface waves whose amplitude and phase vary with the size-wavelength relationship [34, Chap. 4]. Since the surface wave, as it progresses around the surface of the sphere, continually spraying energy tangentially away from the surface, the oscillation is damped with increasing size-wavelength relationship. Also note the damping and the shift of the

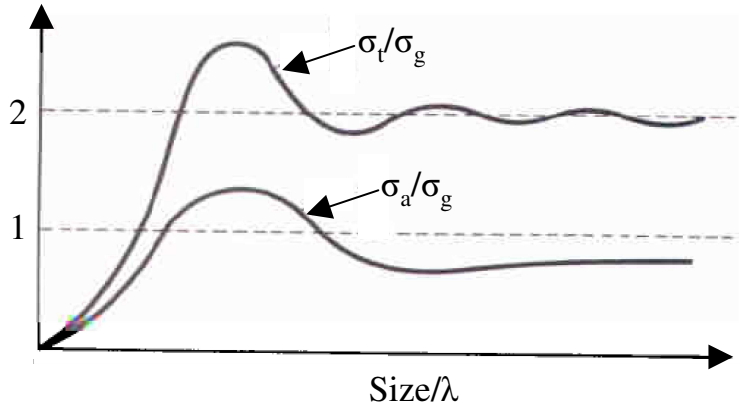

Figure 2.6: Total and absorption cross section (σ_t, σ_a) normalized to the geometric cross section (σ_g), Source: [36, § 10-3].

maximum toward a smaller size in comparison with lossless or less absorbing particles.

2.3.2 Basic radar equations

The radar equation relates the range of a target to the characteristics of the transmitter, receiver, antenna, target and environment. It is useful not just as a means for determining the location and relative velocity of a target, but it can serve both as a tool for understanding radar operation and as a basis for radar design. In this section, the simplest form of the radar equation is summarized.

Let Tr be a transmitter illuminating an object at a large distance R_1, $G_t(\eta_i)$ be the gain function of the transmitter in the incidence direction and P_t be the total power transmitted by the transmitter Tr (**Figure 2.7**). The scattered wave is received with a receiver Re at a large distance R_2. Let $A_r\,(\eta_{\mathbf{s}})$ be the receiving cross section of the receiver and P_r be the received power. The ratio of the received to the transmitted power is one of the interested parameter, to be find. Assume that R_1 and R_2 are large and that the object is in the far field of both antennas. This requires that approximately

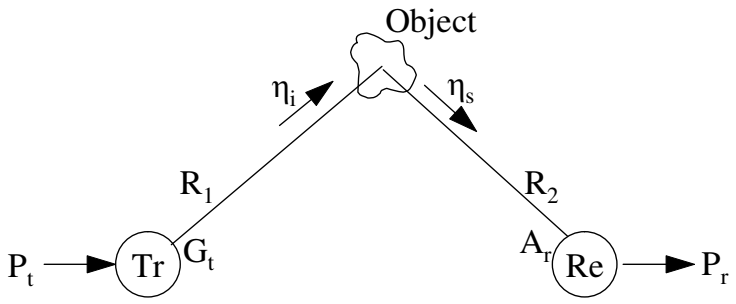

Figure 2.7: Radar principle.

$$R_1 > \frac{2D_t^2}{\lambda}, \qquad R_2 > \frac{2D_r^2}{\lambda} \; . \tag{2.96}$$

Where D_t and D_r are the aperture sizes of the transmitter and the receiver. Radar employ directive antennas to direct the radiated power P_t into some particular direction. The gain $G(\eta_i)$ of an antenna is the ratio of the actual power flux $P(\eta_i)$ radiated per unit solid angle in the direction η_i to the power flux $P_t/4\pi$ of an isotropic radiator per unit solid angle, $G_(\eta_i) = P(\eta_i)/(P_t/4\pi)$. An isotropic radiator is the one which radiates uniformly in all direction. In terms of the gain $G_t(\eta_i)$ of the transmitter, the incident power flux density S_i at the object is given by

$$S_i = \frac{G_t(\eta_i)}{4\pi R_1^2} P_t \; . \tag{2.97}$$

The Power flux density S_r at the receiver is also given by

$$S_r = \frac{\sigma_{bi}(\eta_s, \eta_i)}{4\pi R_2^2} S_i \; . \tag{2.98}$$

Where $\sigma_{bi}(\eta_s, \eta_i)$ is the measure of the amount of incident power intercepted by the target and reradiated back in the direction of the receiving radar, and is denoted as the radar bistatic cross section. The received power P_r, when a wave is incident on the receiver from a given direction η_s, is given by

$$P_r = A_r(\eta_s) S_r \; . \tag{2.99}$$

Where $A_r(\eta_s)$ is called the receiving cross section, which is, according to the antenna theory, the production of the gain function $G_r(-\eta_s)$ and the ratio

$\lambda^2/4\pi$ [36, § 10-2]

$$A_r(\eta_s) = \frac{\lambda^2}{4\pi} G_r(-\eta_s) \; . \tag{2.100}$$

Combining the equations from (2.97) to (2.100) gives the ratio of the received to the transmitted power

$$\frac{P_r}{P_t} = \frac{\lambda^2 G_t(\eta_i) G_r(-\eta_s) \sigma_{bi}(\eta_s, \eta_i)}{(4\pi)^3 R_1^2 R_2^2} \; . \tag{2.101}$$

This is the bistatic radar equation. For monostatic radar, which used the same antenna as a transmitter and receiver (i.e. $\eta_s = -\eta_i$ and $R_1 = R_2 = R$), the ratio of the received to the transmitted power will be

$$\frac{P_r}{P_t} = \frac{\lambda^2 (G_r(\eta_i))^2 \sigma_b(-\eta_i, \eta_i)}{(4\pi)^3 R^4} \; . \tag{2.102}$$

Equation (2.101) and (2.102) give the received power in terms of antenna gains, the distance, the cross section, wavelength and transmitted power. This is only applicable in the far field. It is also required that the receiving antenna has to be matched to the incoming wave in polarization and impedance. If there is a mismatch, (2.101) and (2.102) must be multiplied by the so called mismatch factor, which is less than unity. In addition, both the transmitter and the receiver must be in the far zone of the object.

2.3.3 Approximation of average scattered power

The last two sections demonstrates the characteristics of a single scatterer and its scattering and absorption cross sections as well as the basic radar equation. By means of the single scattering approximation and first order multiple scattering representation, it is possible to drive important formulas concerning wave fluctuation, narrow and wide band pulse propagation, and particle motion. These topics are special interest to communication and radar engineers, who have been extensively treated them in many literatures [2, 33, 34, 37]. Due to some restriction of applications, the present section attempts the step towards approximation of the average scattered power by randomly distributed particles.

Single scattering approximation

According to [2], single scattering approximation is applicable for less dense particles. In this approximation, it is assumed that the incident wave from the transmitter reaches the receiver after encountering very few particles. The scattered wave is assumed to be due to a single scattering by a particle, and all double and multiple scatterings are assumed to be negligible. The formulation for this case is obviously simple and has been used extensively in many applications including weather radar.

Consider a volume V contains a random distribution of particles, which is illuminated by a continues wave (CW) transmitter with a gain function $G(\eta_i)$. The interested parameter to be find is the average power received by a receiver with receiving cross section $A_r(\eta_s)$ in **Figure 2.8**. Consider a small volume dV contains ρdV particles. Where ρ is the number of particles per unit volume. Assume that this volume is located far from both the transmitter and receiver. Let R_1 and R_2 be the distances from dV to the transmitter and the receiver, respectively, and let η_i and η_s be the unit vectors in the directions of the incident wave to, and the scattered wave from, the volume dV.

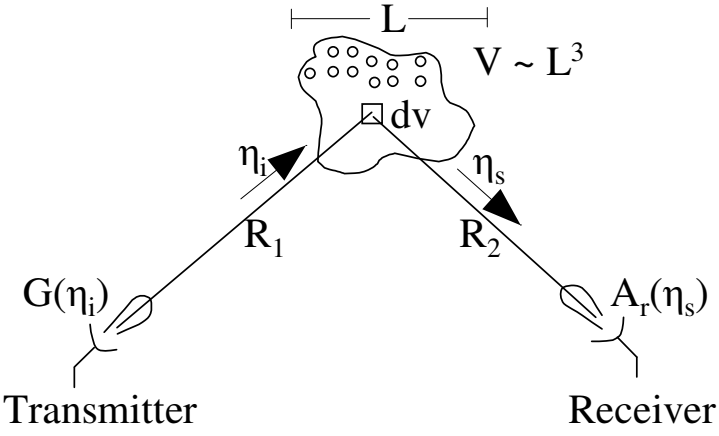

Figure 2.8: Geometric for single scattering approximation.

The incident power density S_i at dV can be given by (2.97). The scattered power density S_r due to a single particle at the receiver is also given by

(2.98). Because of the randomness of the particle distribution, interference between waves scattered by different particles can be neglected and merely add the power scattered once from all particles in dV. Thus, the total scattered power density S_r at the receiver due to all particles in dV is given by

$$S_r = \frac{\rho\sigma_{bi}(\eta_s, \eta_i)}{4\pi R_2^2} S_i dV \ . \tag{2.103}$$

According to (2.99), the corresponding total received power P_r is, therefore, given by the volume integral of the received power for bistatic radar equation of a single particle

$$\frac{P_r}{P_t} = \int_v \frac{\lambda^2 G_t(\eta_i) G_t(\eta_s)}{(4\pi)^3 R_1^2 R_2^2} \rho\sigma_{bi}(\eta_s, \eta_i) dV \ . \tag{2.104}$$

Note that equation (2.104) is applicable when the receiver is matched in both impedance and polarization [38, p. 4].

For a monostatic radar where the transmitter is also used as the receiver ($R_1 = R_2 = R$), the total received power P_r is given by the volume integral of the received power for monostatic radar equation of a single particle

$$\frac{P_r}{P_t} = \int_v \frac{\lambda^2 G_t(\eta_i)^2 \rho\sigma_b}{(4\pi)^3 R^4} dV \ . \tag{2.105}$$

In practice, these radar equations should be modified by including impedance and polarization mismatch and other losses [39, Chap. 2].
The validity of the single scattering approximation depends on the extent to which the incident wave encounters particles in the volume V. This may be measured most conveniently by means of the optical distance γ or known as attenuation coefficient. The single scattering approximation is then valid when

$$\gamma = \int_0^L \rho\sigma_t ds << 1 \ . \tag{2.106}$$

The integration is taken over a path through the volume V, and L is a linear dimension of V (**Figure 2.8**).

As the particle density is increased, it is no longer possible to assume that the direct wave is identical to the incident wave, and it forced to take into account attenuation due to scattering and absorption along the path. The

wave incident on the particle has been previously attenuated by scattering and absorption along the scattering path, and the scattered wave too. This considers some of the multiple scattering effect, which may be expressed as follows by the first-order multiple scattering principle.

First-order multiple scattering representation

First order multiple scattering takes into account attenuation by scattering and absorption of a wave propagating along a ray path. This method is often used in millimeter and optical wave propagation through rain, fog, smog, and snow [2].

The first order multiple scattering can be easily included by extending the radar equations for the single scattering approximation, discussed in the preceding section. The incident power density S_i at dV in **Figure 2.8** should now include attenuation term $e^{-\gamma_1}$ due to the total cross section. Where γ_1 is the optical distance from the transmitter to dV and is given by $\gamma_1 = \int_0^{R_1} \rho\sigma_t ds$. The number of particles (or density) $\rho(s)$ and the total cross section $\sigma_t(s)$ can be a function of the position along the path from the transmitter to dV. Similarly, the scattered power density S_r should be multiplied by $e^{-\gamma_2}$. Where γ_2 is also the optical distance from dV to the receiver and is given by $\gamma_2 = \int_0^{R_2} \rho\sigma_t ds$.

For monostatic radar (i.e. $R_1 = R_2 = R$ and $\gamma_1 = \gamma_2 = \gamma$), the received power P_r given in (2.105) can be then modified for the first-order multiple scattering case as follows

$$\frac{P_r}{P_t} = \int_v \frac{\lambda^2 G_t(\eta_i)^2 \rho\sigma_b}{(4\pi)^3 R^4} e^{-2\gamma} dV \ , \tag{2.107}$$

where γ is given by

$$\gamma = \int_0^R \rho < \sigma_t > ds \ . \tag{2.108}$$

In this derivation the effects of particle size distribution is not considered. This can be easily incorporated in the (2.107) by substituting the total cross section σ_t and the backscattered cross section σ_b with their average value defined in the following manner

$$\rho < \sigma_t > = \int_0^\infty n\,(D, \mathbf{r}) \sigma_t\,(D) dD, \tag{2.109}$$

$$\rho< \sigma_b > = \int_0^\infty n\,(D, \mathbf{r})\sigma_b\,(D)dD \tag{2.110}$$

Where $n(D, \mathbf{r})$ is the number of particles per unit volume located at $\mathbf{r}$ having a range of sizes between D and $D + dD$ and ρ is the number of particles per unit volume given by

$$\rho(\mathbf{r}) = \int_0^\infty n\,(D, \mathbf{r})dD\ . \tag{2.111}$$

Chapter 3

Automotive radar

Automotive radar senors are required to track many targets simultaneously, in range, velocity and angle to perform vehicle control. Ideally, the sensor will have the ability to measure target angle information in elevation as well as azimuth to allow discrimination of extended objects in the vehicle path such as bridges and overpasses. Currently, this is considered to increase the coast and complexity to a prohibitive level. In the future as sensor antennas develop, it can be expected that this requirement will be fulfilled by smart antenna solutions like two-dimensional phased arrays amongst other solutions.

Actual automotive radar sensors represent an important class of monostatic radar system that have been the preferred antenna format for the automotive industry, primarily to keep the antenna aperture area to a minimum and to reduce cost. However, this is not necessarily the optimum topology for radar performance since it is generally dominated by transmitter noise breakthrough rather than the noise figure as in systems with monostatic antennas.

This chapter gives mainly a short review about the measurement system and antenna technology of an actual automotive radar sensor (or LRR2 [1]), on which the feasibility of theoretical results of this work will be probed.

[1] LRR2: Bosch second generation Automotive Long Range Radar Sensor

3.1 Principles of distance and speed measurements

As stated in section 2.3.2, a radar operates by transmitting electromagnetic energy towards the target and obtaining information concerning the location and identification of the target by detecting the backscattered energy. The range of the target is determined by measuring the time difference Δt between transmission and reception of the electromagnetic energy. If the radar transmitter and receiver are in the same casing, the target range R can be determined from

$$R = \frac{c}{2}\Delta t \ , \tag{3.1}$$

where c is the speed of electromagnetic wave propagation in free space (see in (A.16)). For an approximated maximum detection range of an automotive radar sensor up to 200 m (e.g. LRR2 [40]), the time difference Δt to be measured is 1.33 μs.

The total angular excursion ϕ made by the electromagnetic wave during its transit time Δt to and from the targets given by $\phi = 4\pi R/\lambda$. If there is a relative motion between the radar and the target, the target range R and the corresponding phase ϕ are continually changing. The change in R and ϕ with respect to time are know as relative velocity v_r and as Doppler angular frequency w_d, respectively. According to [41, § 3.1], this relationship between the Doppler frequency $f_d = w_d/2\pi$ and the relative velocity v_r of a target with respect to radar can be expressed by

$$f_d = \frac{2}{\lambda}v_r \ . \tag{3.2}$$

For an automotive radar sensor, which operates at 76.5 GHz, equation (3.2) gives a Doppler frequency of 510 Hz for a 1 m/s of relative velocity v_r. The target of an automotive radar sensor could be moved relative to the radar at speed of up to 250 km/h, which corresponds to a measurable Doppler frequency of 35.4 KHz.

Measurement accuracy

There is obviously a conflict in obtaining range accuracy and simultaneously

obtaining velocity accuracy with simple wave forms like pulse and continuous wave (CW) radars that are not modulated in the phase. In such a case, the multiplication of the standard division of errors for range and Doppler frequency is given by [41, § 11.3]

$$\delta T_R \delta f = \frac{1}{\beta\tau\,(2S/N)}\ . \tag{3.3}$$

Where

- S/N is the signal-to-noise ratio of the measurement,
- τ is the effective time duration of the signal,
- β is the effective bandwidth of the signal,
- δT_R and δf are the standard division of errors for range and frequency respectively.

The increase in bandwidth results in better range measurements but less accurate in velocity measurements, and vice versa. This requires the compliance of the uncertainty relation, which states that the product of the effective bandwidth β and the effective time duration τ of the signal must be grater than or equal to π. As it is stated in the communication theory, this is one of the main requirement for an optimum amount of information or measured data passed through a communication channel [42, 43].

The solution to meet such requirement involves the use of waveforms, which have been modulated in phase. For example, in the case of an automotive radar application, Frequency Modulated Continuous Wave radar (FMCW-radar) can perform measurements with relatively good accuracy at signal-to-noise ratios at which measurements done by a pulse-radar may suffer under inaccuracy. This is due to longer illumination time of targets by FMCW-radar than pulse radar.

FMCW-radar needs in the order of ten or more milliseconds for the frequency modulation of several hundred megahertz. The pulse radar, on the other hand, operates with pulse duration of a few nanoseconds ($< 25ns$), which may lead to smaller bandwidth due to limited rise time. Measurement accuracy of FMCW-radar system has been investigated on point target and results have been provided in [44].

Furthermore, range and velocity are not the only parameters demanded of a radar. There are angle measurement and resolution problems, which depend also on the signal-to-noise ratio. For FMCW-radar system, this relationship have been already shown in [45, 46].

3.2 Radar antenna

The basic function of the radar antenna is to couple radio frequency energy from the radar transmission line into the propagation medium and vice versa. In addition, the antenna concentrates the radiated power in a predetermined beam shape and point this beam in a desired direction (referred to as directivity) and provides with it's gain for both transmission and reception of the electromagnetic power (see in section 2.3.2). These are the key characteristics of every radar antenna.

Antenna pattern

The shape of the antenna pattern, which is proportional to the Fourier transform of the aperture field, varies in general with distance R from the antenna as well as with looking direction. The pattern shape over a sphere of constant radius is independent of R in the far field or Fraunhofer region of the antenna (2.96). For example, for circularly symmetric field distributions, the antenna pattern of a homogeneous rectangular aperture is given in **Figure 3.1**. It is represented by the function $|sinc(\theta)|^2$ [31, Chap. 12]. Where θ is the angle, expressed in terms the aperture dimensions.

In the shape of the antenna pattern, the direction of the maximum radiated power is known as the main-lobe whereas all other lobes are referred to as side-lobes. Side-lobes are one of the major sources of radar interference and are undesirable. They may be caused by an inappropriate design of the primary feed and aperture size, and are dependent on the electromagnetic field distribution over the aperture. The ratio between the first side-lobe level and the main-lobe is the important parameter of the capability of the antenna suppressing the side-lobe.

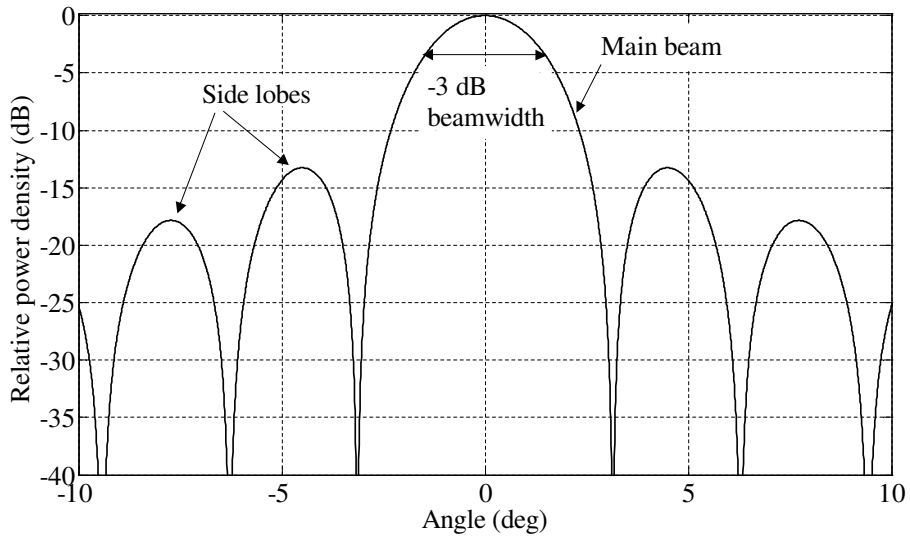

Figure 3.1: Antenna pattern of a homogeneous rectangular aperture, Sinc-function.

Multiple beam system and two-way response

The angular width of the main-lobe is a useful measure of an antenna capability for resolving the angular position of a distant point target. It is the angle between the two points on either side of the main lobe at which the radiated power has fallen to half its maximum value (i.e. the $-3\ dB$ points), and is known as the $-3\ dB$ beamwidth (**Figure 3.1**).

The other additional definition is the angle between the first nulls of the antenna pattern, which is often about twice the $-3\ dB$ beamwidth. This fact makes the following additional point. If two distant targets are separated in angle by the $-3\ dB$ beamwidth and one of them lies in the center of the main beam, then the other will lie in the region of the first null.

Therefore, the use of a narrow-beam antenna system is more attractive for radar sensors, which have to discriminate targets with a very fine angular resolution. Depending upon requirements on field of view, detection performance and cost, the antenna format could be a single scanned or multiple fixed narrow-beam antenna system. In case of automotive radars, these systems have been shown to be suitable only for short-range operation where

road curvature is not significant. But, operation at longer range leads to the possibility of missed target or incorrect target lane identification around bends [1, 47].

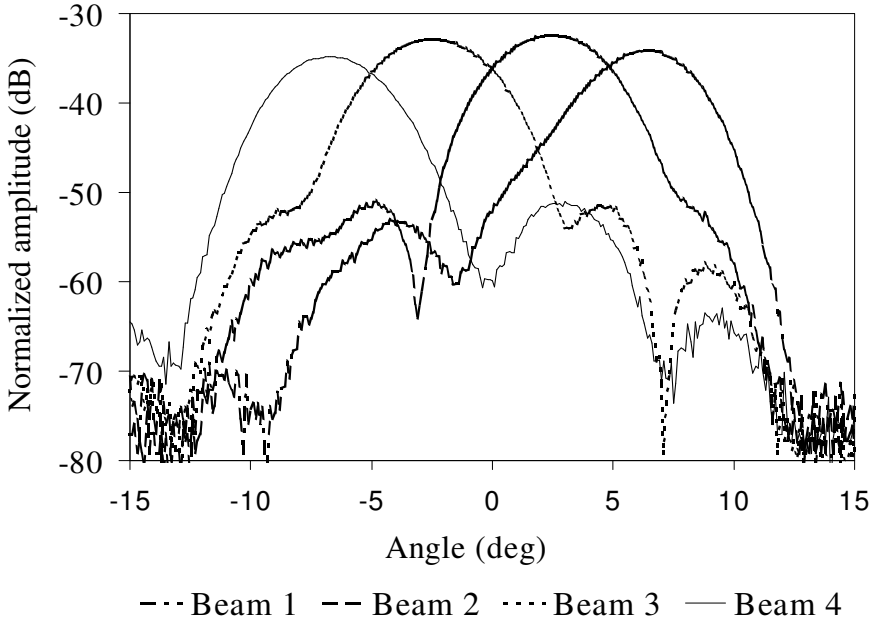

Figure 3.2: Normalized two-way antenna pattern of the LRR2-Prototype.

Radar targets and clutter use the antenna's two-way pattern, which is the square of the one-way pattern if the antenna is said to be reciprocal (i.e. the transmit and the receive pattern of the antenna are usually identical) [48, § 4.2.5]. For radar targets and clutter, the $-3\ dB$ beamwidth becomes then the $-6\ dB$ beamwidth, and side lobs are lowered to double their one-way dB value. **Figure 3.2** shows, for example, the normalized two-way antenna patterns of multiple fixed beam system, implemented by the LRR2-Prototype. It has an angular coverage of about $\pm 8\ deg$ in the azimuth plane. This multi-beam antenna pattern is used to determine the exact angle of a target by applying the so called Monopulse systems, which performs an amplitude and a phase comparison between adjacent beams [41, 45, 46]. The angular coverage is needed to track the targets in the lanes ahead in order to

anticipate vehicles cutting in front of the driver and in order to distinguish between targets that pose a threat and those that do not.

Radar antenna types

The antenna is a key element for automotive radar senors. Requirements, like packaging volume, cost and performance of the sensor are decisive factors on the choice of antenna. The following antenna solutions have been used over the years:

- mechanically scanned parabolic reflector antennas
- quasi-optic lens antennas illuminated by patch radiators
- horn antennas
- static and mechanically scanned planar arrays
- mechanically scanned twist polarization cassegrain reflector and
- frequency scanned antennas

Static planar array provide a low volume antenna whereas mechanical scanning increases the sensor volume due to the scanning mechanism assembly and possibly due to antenna component movement. Quasi-optic solutions, by virtue of the depth associated to with the focal point, also produce a sensor with increased volume. However, it has gained acceptance with the automotive manufacturer due to the possibility that the radar sensor can be mounted without special radome. For example, the lens antenna discussed below.

Lens antenna

Lens antennas, likewise reflector antennas, work on the principle of the theory of geometrical optics [32, 49]. The most important parameter in lens antenna design is the refractive index of the lens materials that may be used for the construction of the lens. It can be classified as solid dielectrics, metallic delay dielectrics, path length dielectrics, metal-plate dielectrics and

rodded dielectrics. A full detail about the properties of each type is given in [50]. Solid dielectrics, like polyethylene ($\epsilon_r = 2.25$), polystyrene ($\epsilon_r = 2.56$) and methyl methacrylate ($\epsilon_r = 2.89$) are widely used for making the lens antenna of the automotive radar sensor. Their geometrics and properties are exactly analogous to optical lenses. Lens antenna can be fed by horn or patch primary feed systems, where the later is easier to integrate in the planar structures [49, 51].

Due to the requirement of automotive manufacturer on low packaging volume of automotive radar sensors, the focal length of the lens antenna has to be essentially small, which unfortunately leads to thick lens. This results in an increasing of material cost and weight as well as signal loss due to attenuation in the material. As shown in **Figure 3.3**, such undesirable issue may be suppressed by introducing the so called Fresnel-steps in the inner surface of the lens antenna.

The depth of the stepped portions of the surface are calculated so that there is a discontinuity of 360 *deg* in the phase distribution on the outer surface at the edge of the steps. The maximum change in the optical path length, which has to be introduced by the lens material, is one wavelength. So, the thickness λ_m needs never exceed $\lambda/(n-1)$ irrespective of the aperture size [49, Chap. 1].

The major advantage of stepping (reducing the thickness and hence the weight of lenses) is but found to result in a drop in lens efficiency due to irregularities in both amplitude and phase distributions, which may be caused by wave diffraction at the edge of each steps.

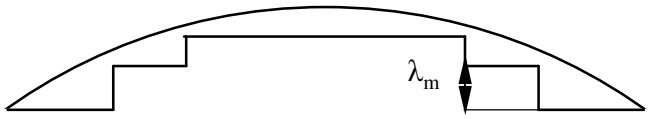

Figure 3.3: Plane-Convex Fresnel lens and its equivalent planar dielectrics.

As mentioned above, the employment of lens antenna in the automotive radar sensor systems makes possible that the radar sensor can be mounted without special radome. Moreover, the oval form of the lens antenna external

surface makes the aerodynamic force more effective by removing the water film, particularly at rainy and snowy weather conditions.

3.3 FMCW automotive radar system

Homodyne radars using FMCW modulation are a common design solution for automotive radar sensors, since such radars generally couple a single antenna via some form of circulator or rather directly to the receiver mixer diodes (**Figure 3.4**). This provides not only a simple low-cost receiver with a relatively poor noise figure ($> 10dB$), but also is well suited to make good use of simple solid-state transmitters. In addition, the signals of FMCW-radars are very difficult to detect with conventional intercept receivers [52].

The basic theoretical analysis in detail and some features of FMCW-radar specially the effects of noise reflected back from the transmitter to the receiver, the application of moving target indication to FMCW-radars and some strengths and weakness of FMCW-radar have been described in many other literatures [53, 54]. Therefore, this section concentrates only on the system and modulation as well as detection characteristics, which will be necessarily important for the next parts of this work.

System

A block diagram of a homodyne FMCW-radar of LRR2-prototype is shown in **Figure 3.4**. Here, the output of a FMCW transmitter (Gunn Oscillator) at frequency f_t is routed through a power divider and mixer (of 20 dB isolation) to the patch antennas, which are placed at the focal point of the plane-convex lens. The wave transmitted by the antennas propagates to, and is scattered from, a target and is received back at the antenna. The wave now has a frequency of $f_t + \Delta f$ and it pass to the mixers where it will be heterodyne with the momentaneous transmitted signal to produce a beat signal with frequency f_b. This Signal is then amplified by a pre-amplifier and provided through an analog digital converter to the post-signal processing and control system so that the targets echoes as a function of range and velocity can be recovered by the spectral analysis of the mixer output.

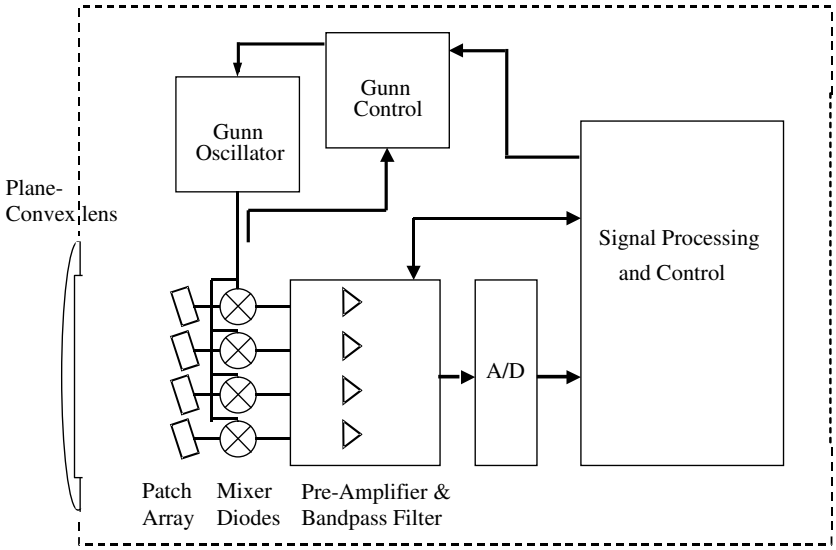

Figure 3.4: LRR2-Prototype: FMCW automotive radar system with a homodyne receiver, Source: [40].

Ensuring the linearity of the frequency sweep of the 76.5 GHz source is a critical step in FMCW-radar. That is why a Gunn Oscillator is usually used with a Phase Locked Loop (PLL or Gunn control) in order to allow proper FMCW-radar operation. Although, newer design make use of microwave monolithic integrated circuit (MMIC-) based voltage controlled oscillator (VCO) technology [55, 56, 57].

Modulation and detection characteristics

The FMCW-radar transmits a continuous wave signal whose frequency is modulated as a function of time with a periodic waveform, such as a triangular wave form presented in **Figure 3.5**. Thus, the frequency of the transmitted signal becomes $f_t(t) = f_0 + \Delta f(t)$. The signal reflected by the target will be delayed in time Δt, which is, according to (3.1), proportional to the target range R, and so has a frequency of $f_r(t) = f_0 + \Delta f(t - \Delta t)$. The demodulation of these two frequencies $f_t(t)$ and $f_r(t)$ in the radar re-

ceiver produces an output frequency, which is known as an intermediate frequency $f_{IF} = f_R = \Delta f(\Delta t)$ or, as mentioned above, beat frequency $f_b = f_R = \Delta f(\Delta t)$ [53, § 13.6].

For a moving target, according to (3.2), the beat frequency contains in addition to the range frequency f_R a Doppler frequency term f_d, i.e. $f_b = f_R + f_d$. In such case, the beat frequency is different for the negative (Ramp1) and positive (Ramp2) slopes of the modulation wave forms. The average of the intermediate frequency gives the frequency term that corresponds to the range of the target, whereas the difference determines the Doppler frequency term, from which the velocity of the target could be obtained:

$$\frac{f_{b+} + f_{b-}}{2} = f_R, \qquad \frac{f_{b+} - f_{b-}}{2} = f_d \, . \tag{3.4}$$

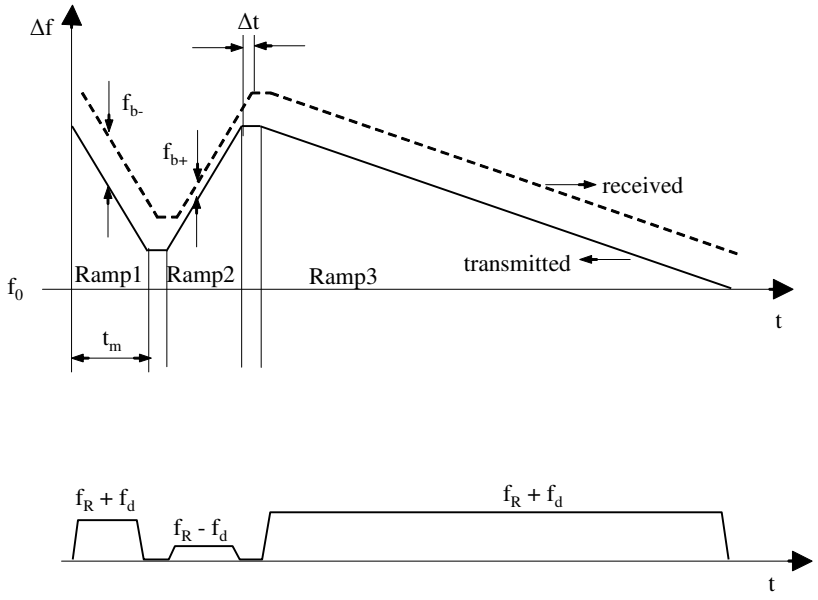

Figure 3.5: LRR2-Prototype: FMCW automotive radar modulation scheme and frequency difference between transmitted and received signal, Source: [40].

When more than one target is presented within the view of the radar, the modulation process has to contain an additional ramp (Ramp3) with different slop than the first two ramps. This modulation scheme should be repeated for some periods so that the post-signal processing could be obtained the informations of the targets, unambiguously. As a consequence, the signal processing increases in complexity that may cause for additional coast to the radar system.

The output of mixer diodes are amplified with low-noise pre-amplifiers and passed through a bandpass filter to a four channel sigma-delta analog-digital converter. The collection of samples is then passed through Fast Fourier Transformation (FFT), which is usually performed using standard Fourier transform digital signal processing (DSP) techniques providing simple and fast data analysis. The output represents the complex spectrum of the reflected signal for each beam-ramp pairs (see beams in **Figure 3.4** and ramps in **Figure 3.5**). This complex spectrum are used to extrapolate informations of targets (range, velocity and angle) using intelligent algorithms like frequency matching and monopulse [40, 46].

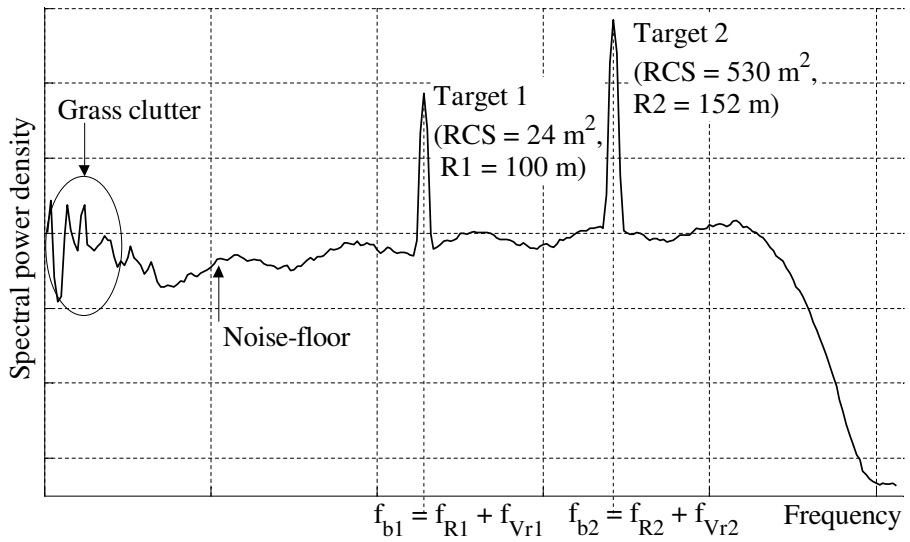

Figure 3.6: Measurement result with targets at 100 m and 152 m.

As an example, **Figure 3.6** shows the processed data for a beam-ramp pair. Triangular trihedral reflectors located at a distance of R1 (or corresponding frequency $f_{R1},\ f_{Vr1} = 0$) and R2 (or corresponding frequency $f_{R2},\ f_{Vr2} = 0$) as well as grass clutter in the near distance are clearly visible.

In additional to the well-known thermal noise that depends upon the receiver bandwidth [53, § 7.3], the process of detection of the received target signal results in an excess noise due to circuit loss and noise generated with in the mixer as well as with in the amplifiers. This overall noise convolutes with transmission functions of systems along the signal path (like ADC, windowing and the FFT) [46, § 5.3], and gives the total noise-floor of the radar system (**Figure 3.6**).
The radar sensor, used for this experiment, has the following main system parameters.

Table 3.1: System parameters of the LRR2-Prototype sensor.

System Parameter	Value
Transmit frequency	$76 - 77\ GHz$
Maximum transmit power	$10\ dBm$
Number of beams	4
Polarization	$45\ deg$ *Linear*
Antenna gain	$28\ dBi$
Azimuth field of view	$\pm 8\ deg$
Elevation field of view	$\pm 2\ deg$
Target detection distance : *range*	$2 - 200\ m$
accuracy	$\pm 0.5\ m$
resolution	$2.0\ m$
Relative Velocity : *range*	$\pm 60\ m/s$
accuracy	$\pm 0.25\ m/s$
resolution	$1.1\ m/s$
Number of ramps	3
Maximum frequency modulation sweep	$500\ MHz$
Update rate	$\approx 10\ Hz$

Chapter 4

Effects of water film on millimeter-wave radar

The wetness of an antenna surface or its covering radome can mainly be caused by adverse weather conditions such as rain, snow and weather under freezing temperature. Considerable works have been done in the past on analysis and measurements of the effects of water film on micro-wave propagation [58, 59, 60]. These studies have obtained quantitative data, which demonstrates that the water film generally affects electromagnetic wave propagation at micro-wave frequencies and results in a considerable loss. Based on that, it is here proceeding to work out in detail these effects on millimeter wave signals using the theoretical fundament given in § 2.2.

To obtain a quantitative result on the effects of water film on the performance of automotive radars, extensive measurements of reflectivity and transmissivity at 76.5 GHz have been made in the laboratory. Furthermore, application oriented experiments have been also performed using an automotive radar sensor, discussed in Chapter 3.

This chapter demonstrates essentially the potential of millimeter-wave radar sensor for identification of the effects of water film on the detection characteristics. This may be used to control the performance of automotive radar sensor systems within the bounds of possibilities.

4.1 Theoretical analysis

The performance of automotive radar sensors is a significant consideration in the choice of placement, with sensor height affecting both multipath performance and ancillary issues such as aperture obscuration by dirt, water and ice or slush. However, the front grille area has been the traditional placement area for actual automotive radar sensors and it is mounted at the height of about 35 *cm* above the road [40, 46].

Depending up on the requirement of the vehicle manufacturer, the radar must be housed with a radome or not. But, the presence of a radome can affect the gain, beamwidth, side-lobe level, and the pointing direction (boresight), as well as change the voltage-standing wave ratio (VSWR) and the antenna noise temperature [41, § 7.9]. Therefore, it should be designed properly, to distort the antenna pattern as little as possible.

In designing millimeter-wave radar sensors for use in ACC and subsequent systems, there is a requirement for data detailing degradation of performance caused by propagation through (and reflection by) water film on the surface of antenna or radome. For that matter, the presence of a water film on the surface of radome has been represented by the following wave propagation model, in order to observe its effect on the millimeter-wave propagation.

4.1.1 Wave propagation model

The formation of water on the radome surface, and then in the propagation path of radar signal, can be represented by the multi-layer wave propagation model (**Figure 4.1**). The radome-water film system is enclosed by air. It is principally the extension of the theory to stratified media that contain absorbing element, i.e. water. Thus, the effects of water film on millimeter-wave radar performance can be examined by revise the equations given in § 2.2 for this model and by matching physical parameters.

As it is clearly remarked in § 2.2, the linear equation systems (2.44) to (2.47) for the perpendicular polarized wave (or TE-Wave) and (2.60) to (2.63) for the parallel polarized wave or (TM-Wave) can be modified for any number of multi-layer media. The way, how these modifications can be done

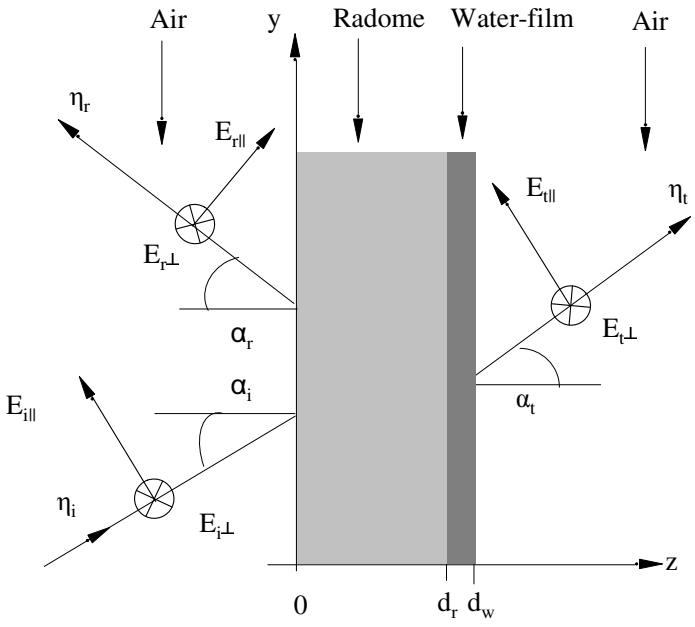

Figure 4.1: water film on the surface of radome.

by imposing restriction on a few purposeful results, has been thoroughly seen in § 2.2.

After makeing use of modification on these linear equation systems (adaptation of parameters corresponding to the model in **Figure 4.1**) and straight forward calculations, the expressions for the complex reflection ($\underline{r}_\perp$, $\underline{r}_\parallel$) and transmission ($\underline{t}_\perp$, $\underline{t}_\parallel$) coefficients of the radome-water film model have been formulated and introduced for the TE- and TM-Waves.

TE-Wave:

$$\underline{r}_\perp = je^{-jk(d_r+d_w)} \frac{\left(\frac{\underline{Q}}{\sqrt{\underline{\epsilon}_{rw}}} - \frac{\sqrt{\underline{\epsilon}_{rw}}}{\underline{Q}}\right)\sin\delta}{2\cos\delta + j\left(\frac{\underline{Q}}{\sqrt{\underline{\epsilon}_{rw}}} + \frac{\sqrt{\underline{\epsilon}_{rw}}}{\underline{Q}}\right)\sin\delta} \tag{4.1}$$

and

$$\underline{t}_{\perp} = e^{jk(d_r+d_w)} \frac{-2}{2\cos\delta + j\left(\frac{\underline{Q}}{\sqrt{\underline{\epsilon}_{rw}}} + \frac{\sqrt{\underline{\epsilon}_{rw}}}{\underline{Q}}\right)\sin\delta}\,, \tag{4.2}$$

where

- d_r and d_w are the radome and the water-film thickness,
- $\underline{\epsilon}_{rw}$ is the complex relative permittivity of water,
- λ and $k = \frac{2\pi}{\lambda}$ are the free-space wavelength and its corresponding wave propagation constant (see also in appendix A).

The terms

$$\underline{Q} = \frac{\cos\alpha}{\sqrt{1 - \left(\frac{\sin\alpha}{\sqrt{\underline{\epsilon}_{rw}}}\right)}} \quad and \quad \delta = kd_w\sqrt{\underline{\epsilon}_{rw} - \sin^2\alpha} \tag{4.3}$$

denote the relationship between the incidence angle to refraction angle in the water film (see (2.50)), and the phase term of propagated wave in the water film (see (2.51)), respectively.
The expressions for the corresponding reflectivity $R_{\perp}$ and transmissivity $T_{\perp}$ are then given by

$$R_{\perp} = |\underline{r}_{\perp}|^2 = \left|\frac{\left(\frac{\underline{Q}}{\sqrt{\underline{\epsilon}_{rw}}} - \frac{\sqrt{\underline{\epsilon}_{rw}}}{\underline{Q}}\right)\sin\delta}{2\cos\delta + j\left(\frac{\underline{Q}}{\sqrt{\underline{\epsilon}_{rw}}} + \frac{\sqrt{\underline{\epsilon}_{rw}}}{\underline{Q}}\right)\sin\delta}\right|^2 \tag{4.4}$$

and

$$T_{\perp} = |\underline{t}_{\perp}|^2 = \frac{4}{\left|2\cos\delta + j\left(\frac{\underline{Q}}{\sqrt{\underline{\epsilon}_{rw}}} + \frac{\sqrt{\underline{\epsilon}_{rw}}}{\underline{Q}}\right)\sin\delta\right|^2}\,. \tag{4.5}$$

TM-Wave:

$$\underline{r}_{\parallel} = je^{-jk(d_r+d_w)} \frac{\left(\underline{Q}\sqrt{\underline{\epsilon}_{rw}} - \frac{1}{\underline{Q}\sqrt{\underline{\epsilon}_{rw}}}\right)\sin\delta}{2\cos\delta + j\left(\underline{Q}\sqrt{\underline{\epsilon}_{rw}} + \frac{1}{\underline{Q}\sqrt{\underline{\epsilon}_{rw}}}\right)\sin\delta} \tag{4.6}$$

and

$$\underline{t}_{\parallel} = e^{jk(d_r+d_w)} \frac{-2}{2\cos\delta + j\left(\underline{Q}\sqrt{\underline{\epsilon}_{rw}} + \frac{1}{\underline{Q}\sqrt{\underline{\epsilon}_{rw}}}\right)\sin\delta} \,. \tag{4.7}$$

In a similar way, the expressions for reflectivity $R_{\parallel}$ and transmissivity $T_{\parallel}$ are also given by

$$R_{\parallel} = \left|\underline{r}_{\parallel}\right|^2 = \left| \frac{\left(\underline{Q}\sqrt{\underline{\epsilon}_{rw}} - \frac{1}{\underline{Q}\sqrt{\underline{\epsilon}_{rw}}}\right)\sin\delta}{2\cos\delta + j\left(\underline{Q}\sqrt{\underline{\epsilon}_{rw}} + \frac{1}{\underline{Q}\sqrt{\underline{\epsilon}_{rw}}}\right)\sin\delta} \right|^2 \tag{4.8}$$

and

$$T_{\parallel} = \left|\underline{t}_{\parallel}\right|^2 = \frac{4}{\left|2\cos\delta + j\left(\underline{Q}\sqrt{\underline{\epsilon}_{rw}} + \frac{1}{\underline{Q}\sqrt{\underline{\epsilon}_{rw}}}\right)\sin\delta\right|^2} \,. \tag{4.9}$$

It may be worthwhile to recall that the phase change on reflection is referred to the first boundary (air-radome), where as the phase change on transmission is referred to the third boundary (water-air). Further, as it is mentioned at the beginning of this section, a properly designed radome has been considered so that the total reflection and transmission can be absolutely referred to as that of the water film. Such kinds of radome should have an optical thickness that is the integral multiple of half-wavelength in the medium (2.55) (refer also in [32, Chap. 21 and 22] and [61, § 4.10]).

For the practical interest of this work, only the reflected and transmitted power from/through the water film has been therefore chosen as the center of the following discussion. For a linearly polarized normal incidence (i.e. $\alpha = 0$, $\underline{Q} = 1$ and $\psi = 45°$), according to (4.4), (4.8), (4.5), (4.9), (2.74) and (2.75), the expressions for the total refelctivity R and transmissivity T are given by

$$R = R_{\perp} = R_{\parallel} = \left| \frac{\left(\sqrt{\underline{\epsilon}_{rw}} - \frac{1}{\sqrt{\underline{\epsilon}_{rw}}}\right)\sin\delta}{2\cos\delta + j\left(\sqrt{\underline{\epsilon}_{rw}} + \frac{1}{\sqrt{\underline{\epsilon}_{rw}}}\right)\sin\delta} \right|^2 \tag{4.10}$$

and

$$T = T_{\perp} = T_{\parallel} = \frac{4}{\left|2\cos\delta + j\left(\sqrt{\underline{\epsilon}_{rw}} + \frac{1}{\sqrt{\underline{\epsilon}_{rw}}}\right)\sin\delta\right|^2} \,. \tag{4.11}$$

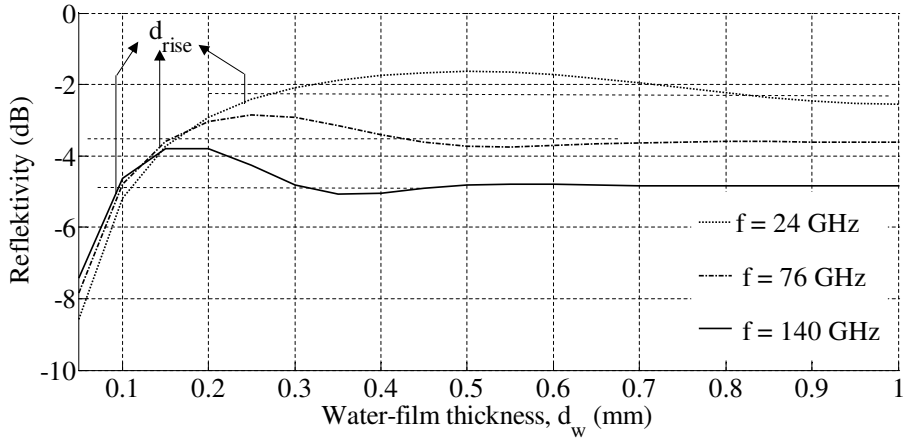

Figure 4.2: Reflectivity from water film at 20 °C.

Where ψ is the polarization angle of the incidence wave.

Equations (4.1) - (4.11) allow computations of quantities that characterize reflection and transmission by water film of known electrical properties and of prescribed thickness. **Figures 4.2** and **4.3** show the dependence of reflectivity and transmissivity on the thickness of the water film at 20 °C for three frequencies, which are used for automotive radar sensors.

According to equations (2.10) and (A.23), the intensity of the electromagnetic wave propagated along the water film is attenuated by the attenuation factor of $e^{\frac{-4\pi}{\lambda}\kappa d_w}$. In the millimeter-wave range, the imaginary part of the complex permittivity of water ϵ'' and its corresponding significant absorption coefficient κ decreases gradually with increasing frequency (**Figure 2.2**). Thus, the absorption of electromagnetic wave in the water film increases with frequency as well as with water-film thickness.

As shown in **Figure 4.2**, the reflectivity is seen to reduce the amplitude of the successive maxima and to give rise to a displacement of the maxima in the direction of smaller thickness. At the penetration or so called skin-depth, where the wave attenuates to the value 36.8% of its original amplitude, absorption of water film is so large that the thickness at which there is appreciable transmission is well below a quarter wavelength in meadim, i.e. $d_w \leq \lambda/4\sqrt{\epsilon_{rw}}$. Consequently, the reflectivity will approach to a con-

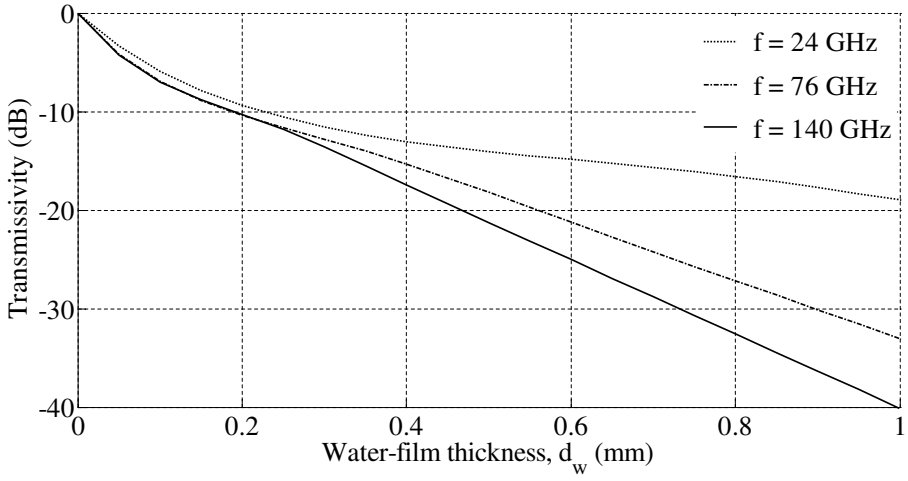

Figure 4.3: Transmissivity through water film at 20 °C.

stant value for further increase in water-film thickness since the wave can not penetrate in the medium much further than the penetration depth [36, § 3-2].

This is just different for the case of non-absorbing film or material like ice on the surface of the radome [8, § 1.6]. Due to interference of waves at the internal and external boundaries of the material, the reflectivity and transmssivity by pure dielectric materials are periodic functions of the thickness with a period of half wavelength. These can be obtained from equations (4.2) and (4.3) by substituting the non complex relative permittivity ϵ_r of the corresponding materials.

As in **Figure 4.3**, the water film transmits millimeter-wave signals with the longer wavelength and strongly attenuates those with shorter wavelength. That means for a 76.5 GHz automotive radar, about 87% of the transmitted power will be attenuated at the water-film thickness of 0.23 mm, where its reflectivity reaches at its first maximum of about -3 dB. This gives an estimation of attenuation per unit length of about 33 dB/mm. The tendency of the signal attenuation increases rapidly with further rise in water-film thickness and an absorption of almost all of the transmitted power may occur with thicknesses above 1.0 $mm, 0.56$ $mm, 0.45$ mm for signals at 24 $GHz, 76.5$ GHz and 140 GHz respectively. **Figure 4.3** shows

also that the attenuation increases with frequencies in which the loss tangent of water ascends (**Figure 2.2**). It proceeds then with gradual growth for frequencies where the loss tangent starts to decrease.

4.1.2 Derivation of the water-film indicator

The water film with thicknesses mentioned above can be easily formed on the surface of millimeter-wave antenna in adverse weather conditions and may degrade millimeter-wave radar performance. Specially automotive radar sensors, which are widely used as comfort and collision mitigation products in the automotive market, needs to detect automatically such performance degradation. This requires the usage of an indicator, which shall be deduced from the physical phenomena of the causes. For this purpose, the relationship between the effects of water film has been examined as follows.

As it is seen in equations (4.10) and (4.11), the reflectivity and transmissivity of the incident wave on the radome-water film system are related over their denominators. Further, according to **Figure 4.2**, the reflectivity from the water film is large enough to be measured, if it propagates back to and received by the antenna as well as if the radar system includes an appropriate measurement system. Therefore, it shall be meaningful to express the transmissivity T as a function of reflectivity R, in order to detect the amount of the signal absorbed by the water film.

Substituting the denominator of (4.11) by (4.10) gives the transmissivity T in terms of the reflectivity R, the complex relative permittivity $\underline{\epsilon}_{rw}$ of the water film and phase term $\delta = kd_w\underline{\epsilon}_{rw}$ of the propagated wave in the water film

$$T = \frac{4}{\left|\left(\frac{1}{\sqrt{\underline{\epsilon}_{rw}}} - \sqrt{\underline{\epsilon}_{rw}}\right)\sin\delta\right|^2} R, \quad for \quad d_w < d_{rise}\ , \tag{4.12}$$

where d_{rise} is the so called rise thickness at which the reflections coefficient r reaches about 90% of its maximum amplitude [62, Chap. 18]. According to (4.10), it can be approximated by $d_{rise} \approx 0.57\frac{\lambda}{4\sqrt{\underline{\epsilon}_{rw}}}$ (**Figure 4.2**).

Because of an ambiguous value of the reflectivity for the water-film thickness greater than d_{rise}, equation (4.12) could not provide a correct value for the transmissivity. Its application is therefore limited for a water-film thick-

ness up to d_{rise} and it represents exactly the theoretical relationship between the transmissivity and reflectivity. The complex relative permittivity $\underline{\epsilon}_{rw}$ can be calculated from equations (2.11) and (2.12) for a given frequency and temperature respectively (see also **Figure 2.2** and **Figure 2.3**).

With equation (4.12), it is achieved to present the definition of an unmeasurable effect of water film on millimeter-wave radar signal (transmissivity) with the corresponding measurable effect (reflectivity). This can be applied for calculating the amount of power propagated through the water film so that the actual detection range as well as the actual detection capacity of millimeter-wave radar sensors can be approximated automatically. It is purposeful particularly for controlling performance of automotive radar sensors, which have to operate by all weather scenario, also including adverse weather conditions.

Further, the water-film thickness formed on the antenna surface can be approximated from the measured reflectivity using equations (4.10) and (4.3). Equation (4.12) is plotted in **Figure 4.4** for a 76.5 GHz millimeter-wave radar incorporation with the water-film thickness and the maximum detection range of an 76.5 GHz automotive radar sensor. The maximum detection range of the radar and its relationship with transmissivity will be discussed in the next section.

Generally speaking, **Figure 4.4** demonstrates the outcome of the above theoretical analysis, how the attenuation of an electromagnetic wave propagated through the water film can be determined for the radar that is designed to detect or measure the corresponding reflectivity.

4.1.3 Relationship between the water-film effects and the radar maximum detection range

Before starting to discuss measurements, it will be helpful for understanding to review the fundamental relationship between the normalized maximum detection range of the radar and reflectivity from the water film. This relationship can be obtained from the monostatic radar equation (2.102) and equation (4.12) that shows relationship between the reflectivity and transmissivity.

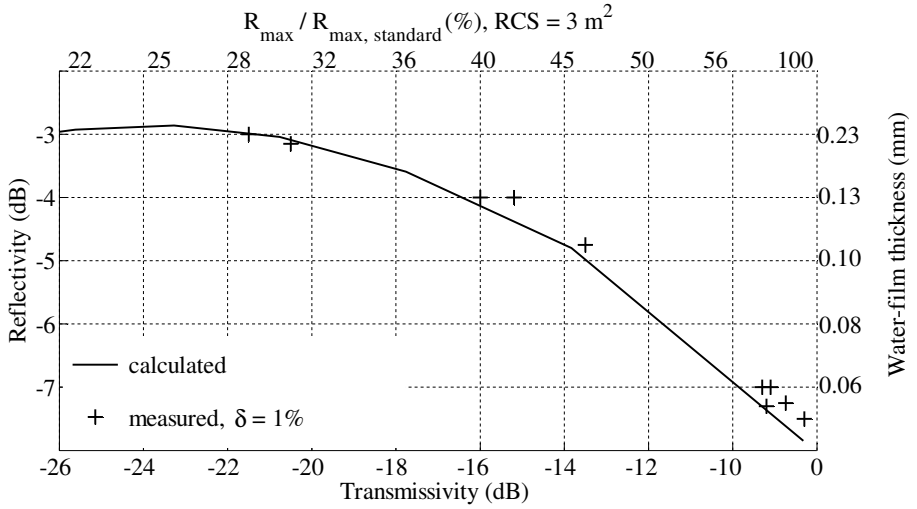

Figure 4.4: Relationship between water-film thickness, reflectivity, transmissivity and maximum detection range of an automotive radar sensor at 20 °C.

In the presence of water film on the surface of the radar antenna or its covering radome, the monostatic radar equation (2.102) has to include an attenuation factor or the transmissivity T. After including T in (2.102) and equating it for the maximum detection range of the radar, an expression of the normalized maximum detection range $R_{max,norm}$ can be formulated in terms of transmissivity T as well as reflectivity R

$$R_{max,norm} = \frac{R_{maxW}}{R_{max}} = (T)^{\frac{1}{4}} \quad , \tag{4.13}$$

where R_{maxW} and R_{max} are the maximum detection range of the radar in the presence and absence of water film, respectively. Note that the relationship between T and R has been given in (4.12). It is also to notice that (4.13) is valid only for specific radar target with a constant radar cross section, and is applicable only for water-film thickness less than d_{rise} (see section 4.1.2). According to (4.12) and (4.13), measuring the reflectivity from water film enables determination of the per cent of maximal detection range that is being detected by the radar in the present of water film on the radar surface. This relationship is provided to **Figure 4.4** with measurements, which will be discussed in section 4.3.

4.2 Experimental investigations

The effects of films, including water film, on the electromagnetic wave propagation have been experimentally investigated to a great extent using different scientific methods [25, 63]. For that matter, this work is only interested on an automatic identification of the effects of water film on detection performance of automotive radar sensors. Before attempting to measure effects of water film with automotive radar system, this section describes even so a less complex and an appropriate lab measuring system, validate theoretical discussed before.

In section 4.3, an application oriented measurement technique will be then followed and illustrated using an automotive radar sensor, to corroborate the technical possibilities of a millimeter-wave radar to monitor its own performance.

4.2.1 Measurement system

Equipment

A Vector Network Analyzer (VNA[1]) has been used for the measurement of effects of water film on millimeter-wave propagation. It operates at the microwave and millimeter-wave region using E-band (60 GHz - 90 GHz) reflexion-transmission module [2] with an out put power of approximately 6 dBm. Its basic capability is to measure the S-Parameters of an Radio Frequency (RF) or micro wave device with sensitivity up to -70 dB and display the result in the frequency domain. Measurements are acquired through IEEE 8-488 bus by an analogue acquisition board placed in a personal computer. Reference [64] gives an account detailed of the VNA.

Measurement Procedure

Horn antennas are widely used as a standard in antenna measurement due to their large gain and superior overall performance to other types of antennas.

[1] Vector Network Analyzer 37369A from Anritsu
[2] 3740A-X Transmission/Reflection millimeter wave module

Hence, E-band pyramid-shaped horn antennas (width 15 mm, height 11 mm and length 37 mm) are used as a transmitter and a receiver [65, Chap. 12]. They are connected to a VNA via a reflection-transmission module. The two antennas are accurately aimed at radome-wet-tissue paper system mounted on mast, covered with an electromagnetic absorbent material (**Figure 4.5**). Depend upon the kinds of measurement, weather it is reflectivity or transmissivity, the antennas should be placed on the same or opposite side of the radome-wet-tissue paper system with the appropriate polarization.

The waveguides are used to connect the antennas with the reflection-transmission module of the network analyzer. It was necessary to employ different kinds of twist wave-guides (0°, 45°, 90°, and 135°) so that either the co-polarization or the cross-polarization components of the reflected and transmitted wave could be measured. If the transmitter antenna is connected with the reflection-transmission module via a 45° twist waveguide, the transmitted signal can be then assumed as 45° linearly polarized electromagnetic wave relative to the incidence plane (i.e. the plane of the page in **Figure 4.5**). The co-polarized component of the reflected signal can be then received by the transmitter antenna itself whereas the cross-polarized component of the reflected signal needs to be received by the antenna that is connected with the reflection-transmission module via a 135° twist waveguide. In this case, the two antennas are placed on top of each other and their distance from the radome-wet tissue paper system should be adjusted so that their antenna patterns (beams) have to be coincide with each other .

For the measurement of the transmitted signal through the radome-wet tissue paper system, the transmitter and receiver have to be placed opposite to each other at the front and back side of the radome-wet tissue paper system. As far as both antennas have been connected with the reflection-transmission module via similar twist waveguides, then the receiver antenna receives the co-polarized component of the transmitted signal through the radome-wet tissue paper system. But, if they have been connected with orthogonal twist waveguides (i.e. a 45° transmitter and a 135° receiver or in the reverse way), the receiver antenna then receives the cross-polarized component of the transmitted signal through the radome-wet tissue paper system. The 45° linearly polarized incident wave is preferred due to its maximum depolarizability effect (see (2.82) and (2.83)) and also due to the practical interest of automotive radar senors (see Chapter 3).

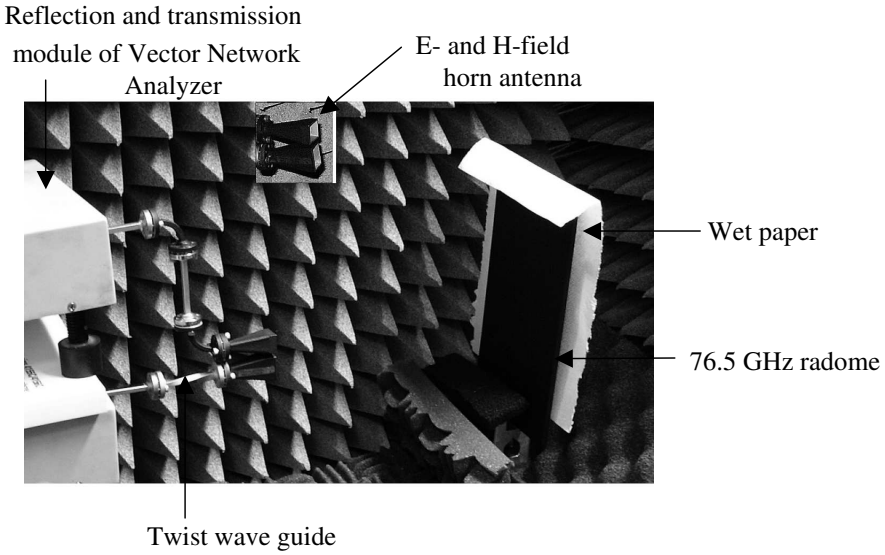

Figure 4.5: Laboratory measurement system to analyse the effects of water film on a radome at millimeter waves.

Tissue paper

In sanitary products like tissue paper, which is made from Cellulose materials [66, 67], the water absorption capacity without dissolving determines the functionality of the product. These special features have made the tissue paper usable as water carrier material in this experiment. The dielectric response of the wet-tissue-paper system is the function of the dielectric properties of individual materials. However, since the tissue paper has a very small real permittivity and negligible loss factor at millimeter waves relative to that of water, then its effect on the experiment can be assumed insignificant [68]. **Figure 4.6** shows the attenuation factor of the tissue paper, measured about 1 dB/mm at 76.5 GHz.

The amount of water on the tissue paper has been measured with a 0.1 g resolution precision balance and is approximated to remain constant during the measurement. The thickness of the water film has been then obtained from the division of this water-amount and the surface area of the tissue

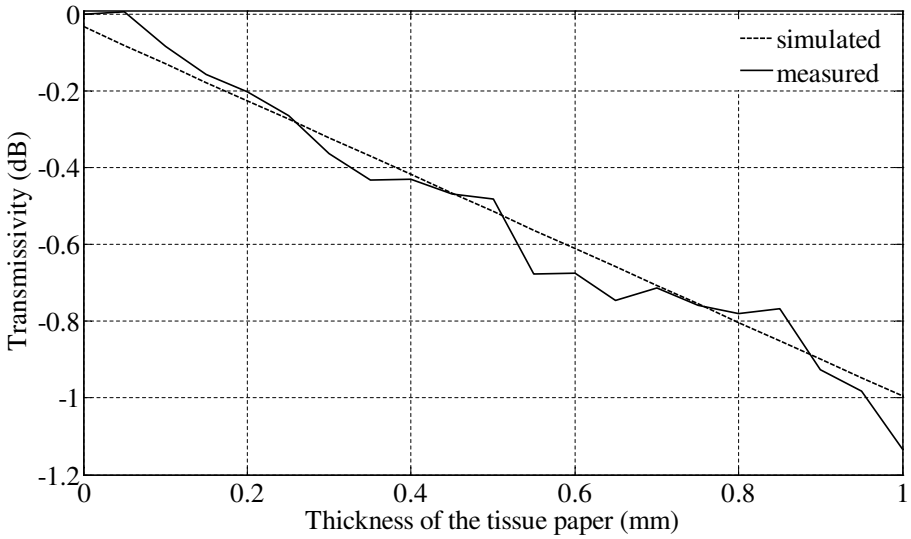

Figure 4.6: Transmissivity through tissue paper at 76.5 GHz and 20 °C.

paper. A water film with a resolution of about 0.05 mm is measured on each tissue paper.

The reflectivity and transmissivity have been then measured as a function of the water-film thickness by overlapping these wet tissue papers. This should be appropriate to investigate the effects of water film on millimeter-wave propagation at the thicknesses of the film, at which the effects are theoretically created a dynamic change. However, one needs careful attention to avoid possible air layer between papers as well as to keep the wetness grade constant while the measurement takes place. These may be a potential cause of measurement inaccuracy and may introduce difference between theoretical and experimental results.

Delectric Radome

The radome-wet tissue-paper system in **Figure 4.5** shall represent the wave propagation model discussed in section 4.1.1. It consists of a dielectric radome, which has been assumed to be properly designed for a 76.5 GHz radar so that its effect on the antenna pattern could be negligible small. This

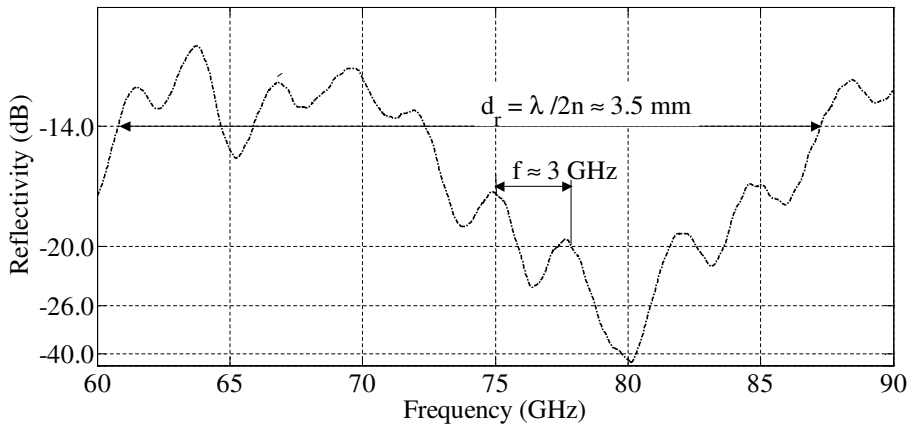

Figure 4.7: Reflectivity of the radome-tissue-paper system versus frequency.

has been proofed by performing measurements on the utilized radome that is made up of a polystyrene material (index of refraction = 1.6 and transmission loss = 0.2 dB).

Figure 4.7 shows the reflectivity, measured on the radom-tissue-paper system. It is almost a periodic function of the thickness of radom-tissue-paper system $d_r = \lambda/2n \approx 3.5\ mm$. Where n is the combined index of the refraction of the radome-tissu paper system. Since the measurement has been performed in a laboratory, where the room could not be absolutely isolated with proper absorber materials, there are an undefined interference on measurements. This has been made notice on the **Figure 4.7** by overlapping a 3 GHz periodic signal on the measurement curve. Furthermore, **Figure 4.7** shows that the radome-tissue-paper system lets signal better transmitted at 80 GHz than at the expected frequency, 76.5 GHz.

Calibration

The VNA is calibrated in the E-band frequency range by using the standard calibration kit [64]. The calibration plane is transported to the measurement plane to which the measured reflection and transmission coefficient must be referred. Then, a measurement has been taken with radome-tissue-paper system shown in **Figure 4.5**. This value has been set up in the VNA as

reference value so that the VNA can measure and store only signals caused by the presence of water film on the radome-wet tissue-paper system.

4.2.2 Results and discussions

For the frequency of interest at 76.5 GHz, the beamwidth of the transmitter and receiver horn antenna in **Figure 4.5** can be approximated from the relationship between the wavelength and the size of aperture [41, § 2.11]. According to the given antenna dimension in section 4.2.1, it should be about 15 deg in the horizontal direction (or azimuth) and about 28 deg in the vertical direction (or elevation) [69, § 9.3]. This implies that the incident wave may make an angle of incidence up to 14 deg with the normal of the radome-wet tissue-paper system. So, the measurements represent an average value over all angles of incidence.

The theoretical results have been obtained from the wave propagation models described in sections 2.2 and 4.1.1 by considering these angles of incidence as well. A comparison between these theoretical and experimental results all around effects of wetness on electromagnetic wave propagation at 76.5GHz are presented in the next two sections.

Reflectivity

Figure 4.8 shows in particular the measured and calculated reflectivity as a function of water-film thickness for both polarization components of an elliptical wave that emerges in the reflected wave from a 45° linear polarized incidence wave (see in section 2.2.2). The reflectivities as a function of angle of incidence and polarization are calculated by using equations (2.72), (4.4), (4.8) for the co-polarized component and equation (2.86) for the cross-polarized component. Averaging of reflectivities over all incidence angle (from -14 deg to 14 deg) gives the theoretical results provided.

The entire set of both measurement components (i.e. co-polarization and cross-polarization) seems in good agreement with the theoretical results. As mentioned in section 4.2.1, the presence of air gap between paper layers results in some measurement inaccuracy and has introduced noticeable difference between the theoretical and practical results, particularly at the

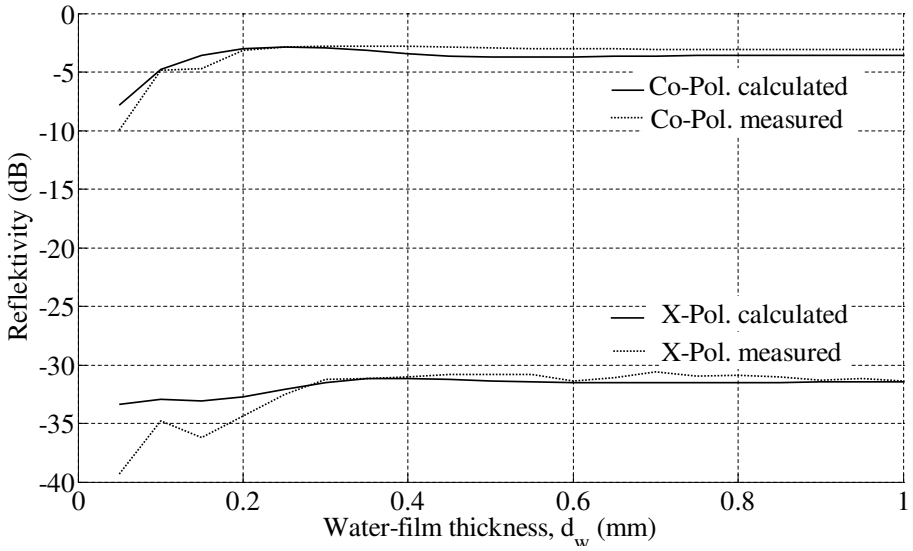

Figure 4.8: Reflectivity from water film at 76.5 GHz and 20 °C.

water-film thickness of $d_w = 0.15\ mm$. Moreover, for water-film thickness above 0.4 mm, the experimental curves show slightly higher values of reflectivity than the theoretical ones. As discussed in section 2.1, this may be caused by the increasing dielectric properties of water due to rise in temperature (**Figure 2.3**).

Transmissivity

Figure 4.9 shows the measured and calculated transmissivity through the water film as a function of its thickness for the co-polarization and cross-polarization components. The transimissivties as a function of the angle of incidence and polarization are obtained by using equations (2.73), (4.5), (4.9) for the co-polarized component and equation (2.87) for the cross-polarized component. Similar to the reflectivity, the mean integral of these transmissivities over all angles of incidence between $-14\ deg$ and $14\ deg$ gives the theoretical results provided to the **Figure 4.9**.

The results in **Figure 4.9** supports the statement that water films attenuates strongly millimeter-wave signals, i.e. $-30\ dB/mm$ for both polarization

components. From the measurement results of the co-polarized component, it does seem that the radome-wet tissue-paper system attenuates more signal than calculated. The increased amount of the attenuation is but in the order of losses caused due to effects of temperature on the dielectric properties of water as well as due to attenuation by the radome and tissue paper (**Figure 4.6**). For these reasons, the deviation between the theoretical and experimental results of the co-polarized component is negligible.

On the contrary, the deviation between the theoretical and experimental results of the cross-polarized component is somehow large. This can be presumably induced by the less sensitivity of the measuring instrument for such extreme small signals (1 dB to 10 dB inaccuracy for measured transmssivities of 40 dB to 90 dB respectively [64]).

Generally speaking, the effects of water film on millimeter-wave propagation, as it is very pronounced in section 4.1.1, have been validated with this experimental investigation. The knowledge of these effects should allow to develop a convenient method for identifying water film on the surface of millimeter-wave radar and its consequence on performance.

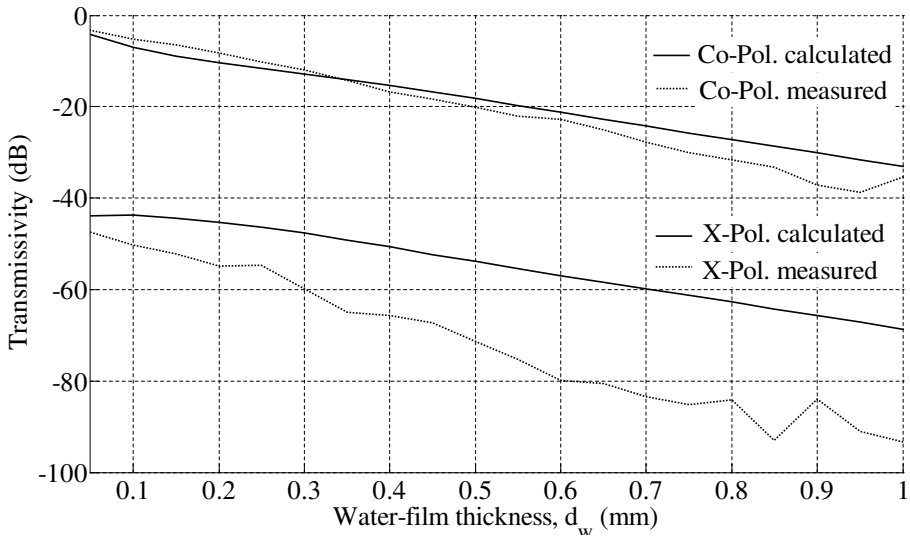

Figure 4.9: Transmissivity through water film at 76.5 GHz and 20 °C.

4.3 Investigations of water-film effects on an LRR2 automotive radar sensor

So far the aim has been to develop an indicator for signal attenuation due to the formation of water film on millimeter-wave radar surface or its covering radome. Having done this, let proceed with analysis of the practical experiments performed on a real FMCW-automotive radar sensor. For this purpose, the LRR2 radar introduced in section 4.3.1 has been employed in the following way.

4.3.1 Measurement system

Equipment

The aim to perform an application oriented experiment has called for employing the LRR2 sensor as measuring equipment for the effects of water film and also rain in the propagation path of the radar signal. System of LRR2 and its principle of operation have been briefly explained in Chapter 3 and the main system parameters are given in **Table 3.1**.

The radar measures signal, which is returned from objects in the radar field of view, and measurements are acquired using a standard computer linked on-line to the radar-emulator system (**Figure B.5**). A measurement program, known as Vector CANape, is used and caused the computer to controll and setup the radar-emulator-computer interface. Signal returns from the radar field of view is sampled and calculated with the signal processing and controlling unit of the radar over 100 ms of a measuring cycle (**Figure 3.4**). About 8192 spectrum and additional measured parameters like information of targets and parameter of components have been send to and stored in the computer for on-line or further off-line measurement analysis.

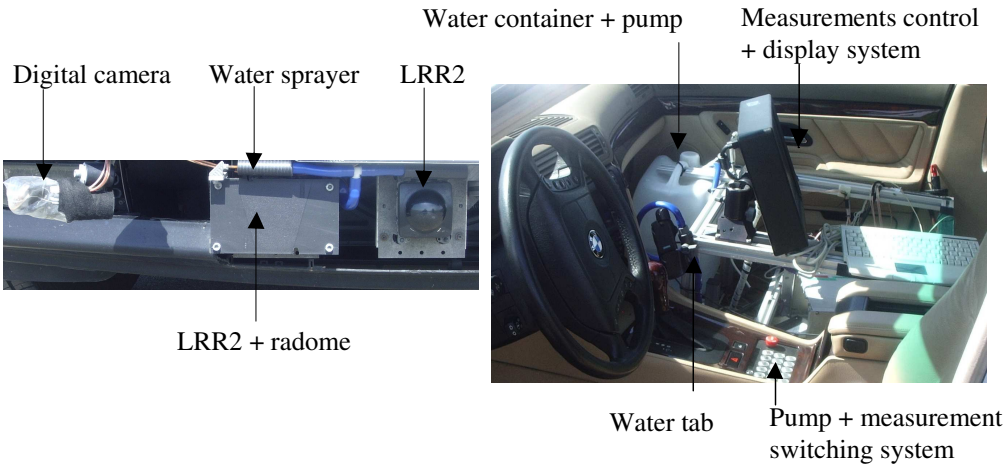

Figure 4.10: Measuring system to detect the effects of water film on the surface of FMCW-automotive radar sensor fitted to the front of a car.

Measurement Procedure

Figure 4.10 shows the general construction of the measuring system on a test car. This consisted at the left side two LRR2 radar sensors, water sprayer as well as digital camera. They are placed on the front grille area of the test car.
The water sprayer system, including a water container with pump and tab, is one of the equipment amongst the measurement data evaluation and displaying systems, which have been presented at the right side of **Figure 4.10**. They are installed at the side of the driver where it is appropriate for on road measurement operation.

The radome, given in **Figure 4.5**, has been fixed in front of one of the LRR2 sensor perpendicular to the direction of wave propagation so that reflected signal from the surface of the radome could be entirely focused on the focal point of the lens antenna where it will be received by the polyrod-patch antenna system.

The external surface of the radome as well as the lens should be made wet with discharged water from the water sprayer that has been mounted on the top of them. This has the purpose to represent the formation of water film on

the surface of the radome or lens antenna in adverse weather conditions. The variation of the degree of wetness on the radome or lens surface is regulated by the flow rate of water through a water sprayer using water tap. It is observed by the digital camera, which has been connected over a coaxial-interface with the same computer mentioned above (**Figure B.5**). While the measurement takes place, recorded results of the camera could be displayed on-line using a visualization program known as "DataVis".

Polyrod-patch system and its equivalent transmission line

Consider the antenna system in **Figure 3.4**. If patch antennas are used as the primary feeds for the lens antenna (wide beamwidth at 76.5 GHz ($> 70\ deg$)), energy could be then radiated on and out of the lens edge. This considerably degrades the antenna patterns of the radar by increasing side lobs and decreasing the gain. Such undesirable effect could be suppressed by employing dielectric rod antennas those are progressively and uniformly tapered to excite surface waves efficiently and to match with free space [69, § 9.4].

The smooth transition due to the tapering of the rod reduces reflected waves and the field within the dielectric rod is not far different from the field in waveguides. This method is already implemented in the antenna system of the LRR2. As **Figure 4.11** shows, polyrod antenna ($\epsilon_r = 2.8$) has been placed on patch antenna with an air gap of a quarter of the wavelength to achieve an impedance matching of the antenna system with a 50 Ω transceiver. The corresponding matching network or the equivalent transmission line of such polyrod-patch antenna system is obtained using the impedance matching technique [70, Chap. 4]. This matching network can be then used to analysis electrically the relationship between load impedance and parameters in the transceiver circuit.

Application of the equivalent transmission line

As shortly mentioned in the above paragraph, the importance of representing the polyrod-patch antenna system with its equivalent network or transmission line is to obtain expression that shows an analytical relationship between load and transceiver parameters.

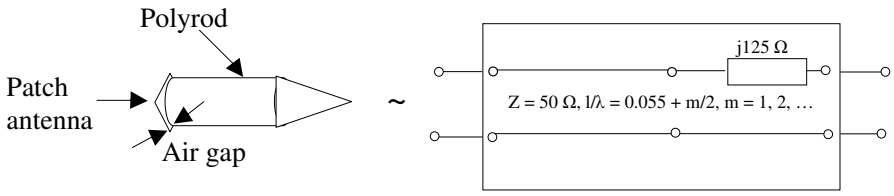

Figure 4.11: Polyrod-Patch antenna system of LRR2-Prototype and its equivalent transmission line.

If the radome in **Figure 4.10** has been placed at a distance of multiple of wavelength from the focal point of the lens antenna and if its surface area is perpendicular to the direction of wave propagation, then rays reflected back from this radome will have the same electrical length at the focal point and make the same phase shift of a multiple of 2π. That means, all these rays may be constructively overlapped at the focal point of the lens where they are received by the polyrod antenna. Depending on the magnitude of the reflected power, this may have significant effects on the functional characteristics of components with non-linear behaviors (such as mixer diode, preamplifier and oscillator).

Such undesirable effect could be positively exploited by monitoring some physical parameters of components, in order to identify radar objects with strong reflectivity. This concept is presented schematically in **Figure 4.12** and it will be experimentally applied to analyse the effects of water film on automotive radar signal in the next sections.

The schematic in **Figure 4.12** includes measurement system to monitor the operation point of the mixer diode whereas the other components have similar purpose as previously explained in section 3.3.

System calibration

As it is known from the literature, diode mixers are the highest frequency low-noise millimeter-wave components in existence [62, 71, 72]. They are fundamentally a multiplier of signals of RF-port and oscillator (**Figure 4.12**).

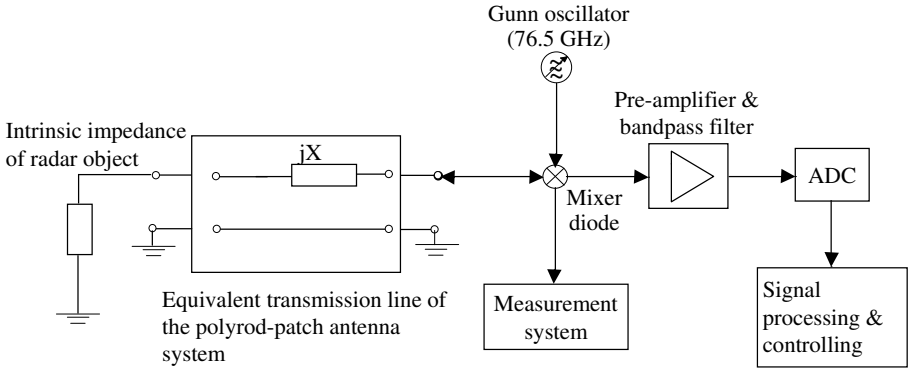

Figure 4.12: Schematic diagram of FMCW-automotive radar sensor including external load, single path

The signal waveform of these two input parameters determines the output by making influence on the operation characteristics of the mixer diodes.

Since diodes possess a strong non-linear characteristic that makes them usable as frequency multiplier, they are sensitive against such set of embedding impedances at all significant oscillator harmonics, mixing frequencies and all diode parameters as well as temperature. That means, measurement calibration on the mixer diode requires knowledge of all those parameter at different significant frequencies and temperatures. To avoid such complexity and make it practicable, relative measurements have been performed only on the diode-operation point.

Usually, the effects of temperature on diode characteristics can be compensated by changing the bias and oscillator power level appropriately with the temperature. Some bias circuits those provide temperature compensation in millimeter-wave application have been proposed in [71, Chap. 5]. In this experiment, the effects of temperature on the characteristic of the mixer diode (mainly the Operation Point) is treated below together with that of the oscillator power.

Measuring the change of the OP of the mixer diode only due to the effects of the port impedance needs necessarily suppression of effects due to other factors like oscillator voltage and temperature. Therefore, it is important to

determine a characteristic function of the OP of the mixer diode as a function of temperature and oscillator voltage.

For this purpose, the OP of the mixer diode is measured at three known oscillator voltages and temperatures. At each temperature, the OP of the mixer diode is measured for the three known oscillator voltages. So, the resulting nine values serve as the so called grid points for interpolating the OP of the mixer diode value at any arbitrary oscillator voltage and temperature. The characteristic function of the OP of the mixer diode is then obtained as a function of any arbitrary temperature and oscillator voltage from these measured values using a two-dimensional formulation of Lagrange's interpolation [73]. The arbitrarily measured OP of the mixer diode value will be then normalized with this characteristic function at the corresponding arbitrarily measured oscillator voltage and temperature. The result is the so called normalized OP of the mixer diode, which has to depend only on the reflected power from the port impedance.

Such method of standardization enables determination of the per cent of shifted OP of the mixer diode that is being by reflected power from the RF-port impedance as follows.

Suppose that, as shown in **Figure 4.10**, the radome-water film system is placed in front of the LRR2 at a distance $d = m\frac{\lambda}{2}$, for m = 1,2, ... The surface area of the radome is orthogonal to the direction of the wave propagation so that the entire reflected signal could be received by the polyrod-patch antenna system of the radar. For appropriately designed radome, this can be represented by the corresponding complex intrinsic impedance $\underline{Z}_{waterfilm}$ of the water film, which may be obtained from the reflection coefficient using the general formulas of transmission line [22, § 5.11]:

$$\underline{Z}_{waterfilm} = Z_0 \frac{1+\underline{r}}{1-\underline{r}} \,, \tag{4.14}$$

where $\underline{r} = \underline{r}_{\perp} = \underline{r}_{\parallel}$ is the complex reflection coefficient of the water film, given by (4.4) or (4.6), and Z_0 is the intrinsic impedance of free-space (A.21). Using the equivalent transformation line of the polyrod-patch antenna system illustrated in section 4.3.1, $\underline{Z}_{waterfilm}$ can be transfered to the RF-port of the radar transceiver circuit. **Figures 4.13** and **4.14** present the $\underline{Z}_{waterfilm}$ and its equivalent transformed impedance $\underline{Z}_{equ}$ as well as their corresponding reflectivity.

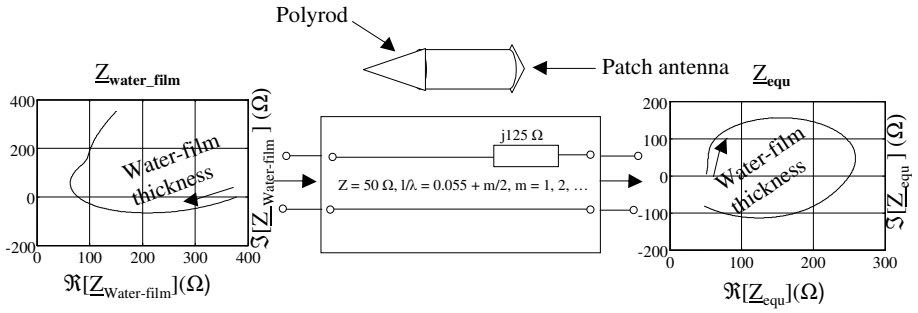

Figure 4.13: The complex intrinsic impedance of the water film and its equivalent at the RF-port.

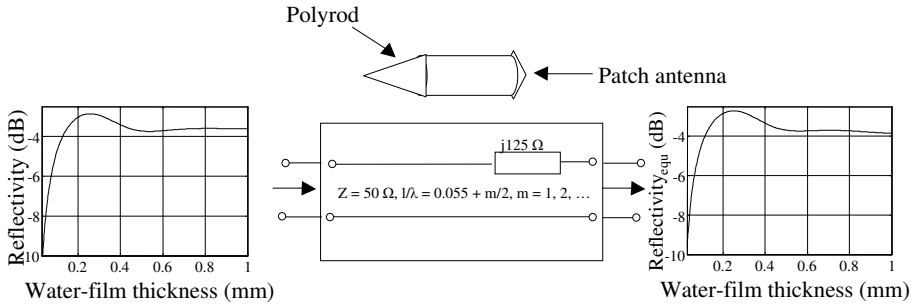

Figure 4.14: Reflectivity from water film and its equivalent at the RF-port.

For the absent of water film in the propagation path of the radar signal ($\underline{Z}_{waterfilm} = Z_0 = 377\ \Omega$), the transceiver circuit of the radar is matched to 50 Ω RF-port impedance (**Figure 4.13**). According to section 4.3.1, as far as the polyrod-patch antenna system has been represented by a loss free equivalent transmission line, the reflection coefficient of water film changes only in phase. So, its magnitude or the reflectivity at the input and out put ports of the transmission line remains unchanged (**Figure 4.14**).

Finally, at constant oscillator frequency, the relationship between the reflectivity from the water film and the normalized OP of the mixer diode can be obtained by simulating the electrical circuit of the transceiver. This includes the equivalent RF-port impedance of the water film (see the circuit

layout in Appendix B.3). This relationship (or known as calibration curve) is presented in **Figure 4.15** for an OP of mixer diode, normalized with its standard value.

The OP of the mixer diode is to be measured with the measurement system that consists a low-pass filter and an analog-digital converter (see **Figure 4.12**). Measurement results could be then interpreted to their corresponding reflectivity value using the calibration curve in **Figure 4.15**. Reflectivities below $-10\ dB$ does affect the OP of the mixer diode, insignificantly. For example, the reflectivity from the internal and external boundaries of the pure lens-antenna system ($\leq -15\ dB$) could not noticeably shift the OP of the mixer diode.

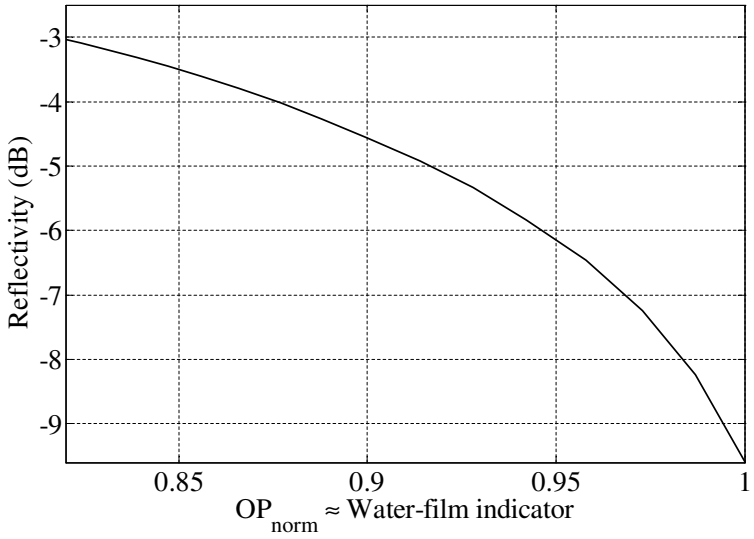

Figure 4.15: Calibration curve: operation point of mixer diode versus reflectivity from water film.

4.3.2 Results and discussions

Indication of the radar maximum detection range

A series of measurements have been performed using the system described in section 4.3.1 and the calibration curve given in **Figure 4.15**. Some of the experimental data that has been taken to determine the reduction of the maximum detection range of the radar are shown in **Figure 4.4** and **Figure 4.16**.

In an air plan field with free of any other scatterers (except road-clutter), a triangular corner reflector with $RCS = 3\ m^2$ is placed as a radar target at a distance of more than 500 m from the test vehicle with the radar boresighted on the corner reflector. Note that a triangular corner reflector with improper angle alignment will degrade by 3 dB if all three edges deviate by 0.35λ or a single edge deviates by 0.7λ [74]. The radar test vehicle is driven slowly with constant speed towards this target along the radar boresighted and detection parameters (like range, velocity and angle) of this target have been recorded. In the same way, a number of measurements have been performed with spray water on the surface of the radome (**Figure 4.10**). The degree of wetness on the radome surface is varied by regulating the flow rate of water through a water sprayer, which has been mounted at the top of the radome as well as of the lens.

The target informations like velocity and angle are used only for controlling the uniformity of the speed between measurements and the alignment of target. The maximum detection range of the target for each measurement with spray water is normalized with the maximum detection range of the target with no water. These normalized detection range informations are provided to **Figure 4.4** with the corresponding reflectivities, which are extracted from the calibration curve in **Figure 4.15**. Note that, in the measurement, the OP of the mixer diode is averaged over four mixer diodes (**Figure 3.4**) before normalization.

The presented measurement is relative in value and extreme care has been taken to minimize an unavoidable sources of errors. The relative error $\delta = 1\%$, given in the **Figures 4.16** and **4.17**, is consisted of external influences like external temperature (causes signal-path expansion) and road-

clutter from different road types. It has been determind through observation over long time ($\geq$ 1 hr) measurement results at different traffic scenarios.

Generally, the measurement results in **Figure 4.4** show relative good agreement with the theory. As it is already stated in section 4.1.1, at a water-film thickness of 230 μm, where about 90% of the transmitted power is attenuated by the water film, the maximum detection range of the radar reduced below 30% of its desired value.

Furthermore, an additional experiment has been carried out on a number of triangular corner reflectors with $RCS = 3\ m^2$. They have been placed at a distance of 25 m, 55 m, 120 m and 180 m away from the test vehicle. Figure 4.16 shows that all these four targets are well detected by the radar as far as water has not been sprayed on the surface of the radome. The indicator remains thus in its no-water signal value. As it is evident from the picture taken by the digital camera (**Figure 4.10**) to the presence of water on the radome surface, the indicator signalize gradual loss of target up to an absolute blockage of radar. After about 42 minutes, when the water container becomes empty, the radar is started again to detect targets step by step and the indicator rise to its original value. But, due to the wet radome, the indicator can not be reached out its original no-water value.

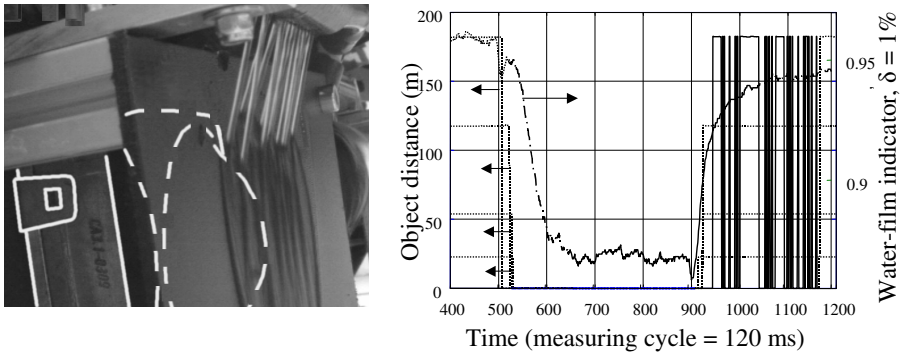

Figure 4.16: Correlation between the distance of radar object and the indicator of water film on the surface of radome at 76.5 GHz and 20 °C.

Indication of the radar detection capacity

The performance of an automotive radar sensor without covering radome can be also degraded by wetness of radar antenna. The effect may be small compared to that of radome. However, water impinging or snow freezes on an antenna lens can have serious effects. The wetting of surface through which millimeter-wave signal transmitted should be avoided or if not at least identified. Ice frozen on the surface of antenna does not usually cause a series problem. When ice is in the process of melting, however, the water surface can distort the signal and in some instance can completely block the radar sensor.

Measurements, carried out in a constant traffic scenario using the measurement system mounted on the test car (**Figure 4.10**), are presented in **Figure 4.17**. It is to observe that exerted aerodynamic forces on the spherical surface of the lens repress the formation of homogeneous water film and contribute to rapid shedding of the water from the surface of radar antenna. Therefore, the possibility to appear total degradation or the so called absolute blindness of the radar sensor has been minimized. Nevertheless, the wetness of the antenna lens alone is enough to reduce object detection capa-

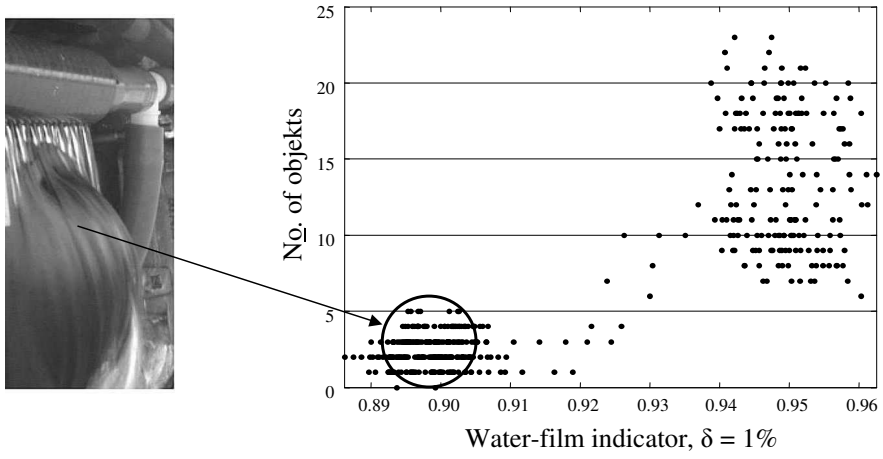

Figure 4.17: Radar detection capacity versus indicator of water film on the surface of radar antenna at 76.5 GHz and 20 °C.

bility of the radar to a certain extent. The number of detected objects by the radar reduces significantly and becomes below 5 while water sprays on the antenna lens. It has been greater than 10 as the radar antenna lens was free from water.

Chapter 5

Effects of rain on millimeter-wave radar

The second major cause of millimeter-wave automotive radar signal degradation is that of the interaction of electromagnetic waves with rains in the propagation medium. A lot of scientific work has been reported in the past on the significance of this interaction in the micro-wave and millimeter-wave range [10, 11, 13, 75, 76, 77, 78, 79, 80, 81]. These studies have been obtained quantitative data, which demonstrate that precipitation generally affects electromagnetic wave propagation at micro- and millimeter-wave frequencies and results in a considerable effect on the detection performance of radars.

Some of the effects of precipitation on wave propagation have a direct application to identify rain in the scanning view of a radar. Hence, the scope of this chapter will be confined on hypothesis those enable the identification of rain using automotive radar sensor by applying the theory given in § 2.3. This can be used as an indicator for the degree of possible degradation of performance and may be applied to deal with proper counteractions so that availability of automotive radar sensor could be assured at rainy weather condition.

5.1 Theoretical analysis

5.1.1 Raindrop-size distribution

Raindrops are randomly positioned in space with a special drop size distribution that depends on the rainfall rate or rain intensity I. It is assumed that the rain droplets are spherical in shape except in heavy rain, where droplets have the shape of an oblate ellipsoid because of the strong winds usually associated with such events. Hence, raindrop-size distribution is related to the rain rate.

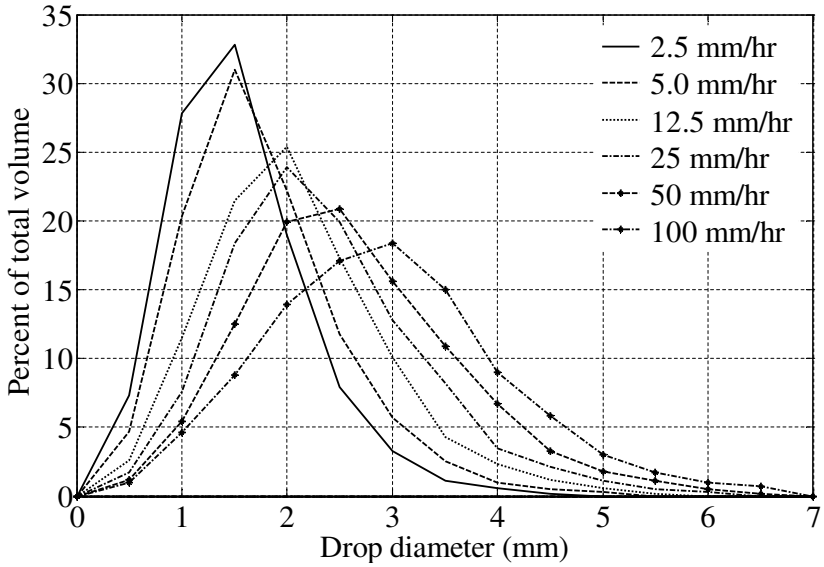

Figure 5.1: Percentage of the total volume contributed by drops of various sizes for six precipitation rates; Laws and Parsons original data 1943, Source: [82].

The raindrop-size distributions have been determined experimentally in various parts of the world, for example, by Laws and Parsons (1943), Wexler (1948), Marshall and Palmer (1948), Best (1950), Hood (1950) [83]. For Rayleigh scattering [2, § 2-3], most of these workers have calculated simultaneous values of reflectivity $Z = \sum D^6$ and rainfall rate or rain intensity

$I = \frac{\pi}{6}\rho\sum(v_D D^3)$ from the distribution of drop-size obtained on a horizontal surface. Where v_D is the terminal velocity of a drop of diameter D and ρ is the density. Typical values of rain intensity I are 0.25 mm/hr (drizzle), 1 mm/hr (light rain), 4 mm/hr (moderate rain), 16 mm/hr (heavy rain), and 100 mm/hr (extremely heavy rain).

The size distribution of the raindrops may also be expressed in terms of the percentage of the total volume contributed by drops of various sizes. Empirical distributions given by Laws and Persons are a reasonable choice for a mean drop-size spectrum in continental temperate rainfall. Hence, it has been taken as reference for this work and presented in **Figure 5.1**. Note that a very big fraction of raindrops are larger than $D \geq 1\ mm$ at rainfall intensities $I \geq 2.5\ mm/hr$. According to section 2.3.1, these raindrops may have big total and absorption cross section (see σ_t, and σ_a in **Figure 2.6**), and applicably produce significant effects on the millimeter-wave propagation and scattering.

5.1.2 Total backscattering cross section of rain

Hydrometeors are essentially particles of water within the atmosphere, they can take the form of liquid water as in rain, mist and fog or ice as in clouds, hail and snow. Plane electromagnetic waves travelling through air containing precipitation are scattered and absorbed by the particles of ice, snow or water. Water with its larger dielectric constant scatters more strongly than ice (see **Table 1.1**). In addition, it has a much larger dielectric loss and the attenuation due to thermal dissipation is therefore much greater for water particles than for ice particles [2, 29]. This makes rain more accountable for the degradation of performance of millimeter-wave radars than ice. Hence, this section concentrates only on the effects of rains on the millimeter-wave propagation.

The rain affects the propagation of electromagnetic waves in different ways. If radiowave is propagating through a region containing raindrops, it will be scattered, depolarized, absorbed and delayed in time. All these effects of rain on the wave propagation are related to the operating frequency and polarization of the wave as well as to the rain rate, which influences the form and size distribution of the raindrops. These physical relationships

have been already studied and theoretical and experimental results are presented in many publications, mentioned at the beginning of this Chapter. Although, this section will be restricted on the examination of the backscattering effect if it can be made applicable for an automatic identification of rain and its consequence on the detection performance of automotive radar sensor systems.

As it is illustrated detailed in section 2.3.1, three quantities with the dimensions of area are derived for a particle in the path of a plane travelling wave. The backscattering cross section σ_b is defined in such a way that σ_b multiplied by the incident intensity would be the total power radiated by an isotropic source, which radiates the same power in the backward direction as the scatterer. The scattering cross section σ_s is such that σ_s multiplied by the incident intensity, is the power scattered by the particle. The total absorption cross section σ_a is such that σ_a times the incident intensity, is the total power taken from the incident wave.

Based on the relationship between these cross sections and the ratio of precipitation size to the wavelength, the effects of rain on wave propagation can be explicitly examined and sought for their practical applicability (refer sections 2.3.1 and 5.1.1). For example, the backscattering properties of precipitation may make possible extensive use of millimeter-wave radar sets for identification purpose of precipitation and could be applied to find out precipitation effect on the detection performance of radars.

The radar signal from precipitation is, however, not steady like that from a point target. The received power at any instant is made up of the resultant of signals from a very large number of precipitation, and depends on their exact arrangement in space, which is continually changing. It means, an instantaneous observation of received power gives very little information about the precipitation, and the signal at any given range has to be averaged until a large number of independent returns have been received. This can be well achieved by FMCW automotive radar, which illuminates the scatterers for relatively longer time (in the order of some milliseconds) and can be also averaged out measurements of rain returns from several antenna elements.

The receiving patterns of LRR2 (**Figure 3.2**) are confined within narrow solid angles. The characteristics of the precipitation (the density ρ and cross

sections σ) can be thus assumed to be uniform throughout the rain cell volume V_{RCR} in **Figure 5.2**.

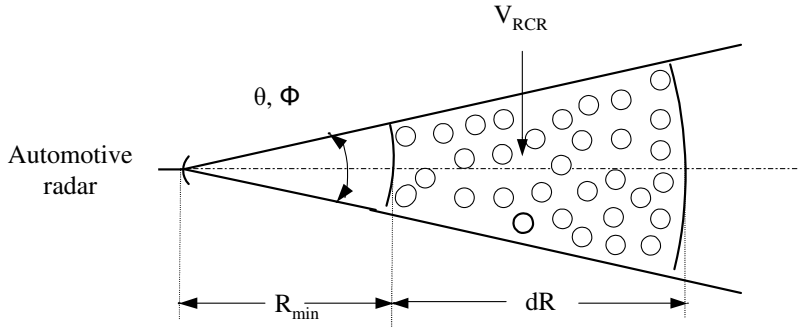

Figure 5.2: Plan view showing narrow beam monostatic radar consisting of raindrop scatterers. θ and ϕ are the half-power beamwidths in the azimuth and elevation, respectively.

In such a case, the ratio of the power received to the power transmitted can be calculated according to the backscattering radar equation (2.107). This can be considerably simplified from the volume integral to the length integral using the expression $V_{RCR} = ((\pi R_{min}^2 \theta\phi) \,/\, (8ln2))\, dR$ [2, § 4-3], and gives the following general equation

$$\frac{P_r}{P_t} = \frac{\pi}{(4\pi)^3} 8ln2\lambda^2 G_t(\eta_i)^2 \theta\phi \int_{R_{min}}^{R_{min}+dR} \frac{\rho\sigma_b}{R^2} e^{-2\gamma} dR \,. \tag{5.1}$$

The fact that the target normally fills the beam at any range accounts for the inverse square law for received power versus range, in place of the usual fourth-power law for a point target such as a vehicle. The total backscattering cross section $\rho< \sigma_b >$ (see (2.110)) per cubic meter of rain cell volume V_{RCR} in the antenna beam can be obviously equated from (5.1) as follows

$$\rho< \sigma_b > = \frac{114}{\lambda^2 G_t(\eta_i)^2 \theta\phi e^{(-2\rho<\sigma_t>R_{min})} \int_{R_{min}}^{R_{min}+dR} \frac{1}{R^2} e^{(-2\rho<\sigma_t>R)} dR} \frac{P_r}{P_t} \,. \tag{5.2}$$

All parameters in (5.2), except $\rho< \sigma_b >$ and $\rho< \sigma_t >$, are either known or measured.

In case of millimeter-wave radar, Mie scattering occurs since most of the raindrops are in the order of the size of the wavelength (**Figure 5.1**). And then, the calculations of the cross sections can be treated by the Mie-theory [2, § 2-8]. The optical distance γ in (5.1) can also expressed with the attenuation due to rain $\rho < \sigma_t >$ (see (2.108)). This is nearly proportional to the rain intensity I and given by $\rho < \sigma_t > = K_t I$. The constant K_t, on the other hand, depends on the rain intensity I and some typical values are given in [2, § 3-2]. For millimeter and optical frequencies, $K_t \approx 0.4 - 0.8\ dB/km/mm/hr$ at rainfall intensities $I < 10\ mm/hr$, and K_t decreases to $0.15 - 0.3\ dB/km/mm/hr$ at rainfall intensities $I > 10\ mm/hr$.

So far, the attenuating effect of the precipitation $e^{-2\gamma}$, through which the signal may have to pass, has been considered. It shows that the influence of the rain intensity over the attenuation makes it difficult to determine the backscattering cross section $\rho < \sigma_b >$ of the rain using (5.2) by only measuring the received power.

For precipitation that is found in near distance to the radar sensor, it could be, however, possible to neglect the attenuation term in (5.2). That is, $\rho < \sigma_b >$ can be approximated as a function of rain intensity I by measuring the average backscattered power P_r. Experimental investigation on this relationship will be presented and discussed in detail in the next section.

5.2 Experimental investigations of rain effects

Since the effects of rain on the wave propagation are generally correlated to each other over the rainfall intensity, the ability to measure returned signal from rain may lead to find out the loss of the signal-to-noise ratio of a radar target. Note that the signal-to-noise ratio is one of the main parameter in terms of which the detection performance of a radar sensor could be judged [39].

The receiver sensitivity of an automotive radar is enough to detect a small amount of power returned from scatterers like raindrops. Obviously, the less the distance of the scatterers from the radar, the more a radar is able to detect smaller or less efficient scatterers due to less antenna beam spreading loss.

This has been verified by conducting an experiment with LRR2 (see section 3.3) on targets at 100 m and 152 m. Measurement results are plotted in **Figure 5.3** for dry and moderate rain weather conditions. It shows effects of rain on radar detection characteristics, namely target signal attenuation and near distance backscattering as well as reduction of train-clutter in near distance. These rain effects are a function of rain intensity and target range (see section 2.3.3 and 5.1.2).

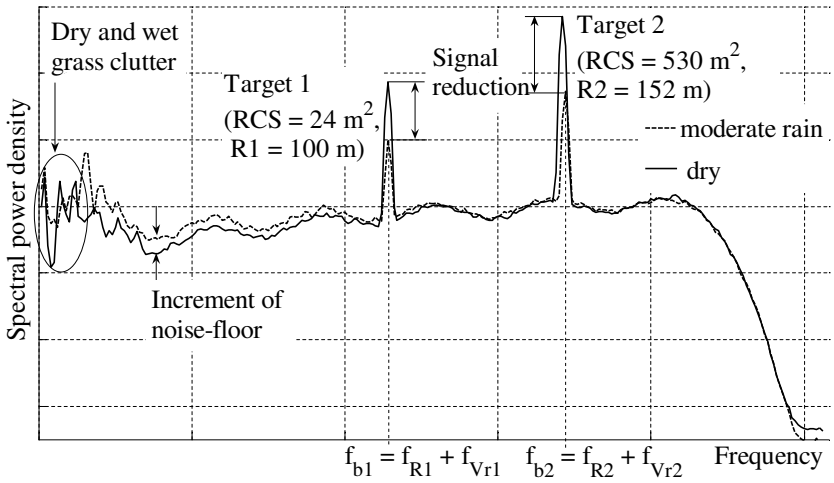

Figure 5.3: LRR2 measurement result with targets at 100 m and 152 m in dry and rainy weather conditions.

As it will be treated in the next sections, this has been generally invoked to exploit specially the near distance backscattering for identification of rain and its effect on the detection performance of automotive radar sensors.

5.2.1 Measurement system

The investigation is conducted with the measurement system shown in **Figure 4.10**. It has been performed in an air port field, where there is no any kind of scatterer except road-clutter. The radar is aimed at reference targets introduced below. The average power of the backscattering signal P_r can be obtained by the integration of the measured power spectral density within

the frequency range, which corresponds to the distance R_{min} and $R_{min} + dR$ of the rain cell volume of **Figure 5.2**. The ratio of the rain backscatter to the trihedral backscatter at the rain range has been measured. This technique offered the advantage of:

- permitting the results to be independent of transmitted power, antenna gain, receiver sensitivity, and system losses,
- requiring analysation of only ratios of measured average power.

Reference targets

Two triangular trihedral reflectors, which are made from aluminum plate and have radar cross sections of 0.5 m^2 and 3 m^2 under all weather conditions, are used as reference targets. It has been usually assumed that there is no discernible changes on the radar cross section of dry and wet reflector [13]. The 0.5 m^2 and 3 m^2 trihedral reflectors are mounted on the top of 40 cm high plastic rod covered by absorber and mast at a range of 10 m and 50 m from the vehicle with the radar boresighted on the reflectors, respectively.

Rain backscatter has been made by comparing its received signal to the reference target of the 0.5 m^2 trihedral reflector. The 3 m^2 trihedral reflector is used as a target to observe the reduction of the signal-to-noise ratio at different rainfall rate. The size was chosen to provide a signal that would be equivalent to the backscatter of personal vehicles [84], greater than ground clutter and rain backscatter.

Meteorological instrumentation

The rainfall intensity has been measured with an accurate tipping bucket rain rate gauge (Casella CEL) under the side of the test vehicle. It has been assumed that the rain is homogeneous in the vicinity of the test vehicle.

Rain collects in one side of the bucket, which then tips when a predetermined volume of water has been collected. Each tip of a bucket is equivalent to 0.1 mm of rainfall and the corresponding time duration for each tip then has been recorded using a software tool developed for this purpose. The ratio

of the depth (0.1 mm) to the recorded accumulation time (in hours) gives then the intensity of rain in mm/hr. **Figure 5.4** presents the rainfall rate measured with this rain gauge at an air port field station.

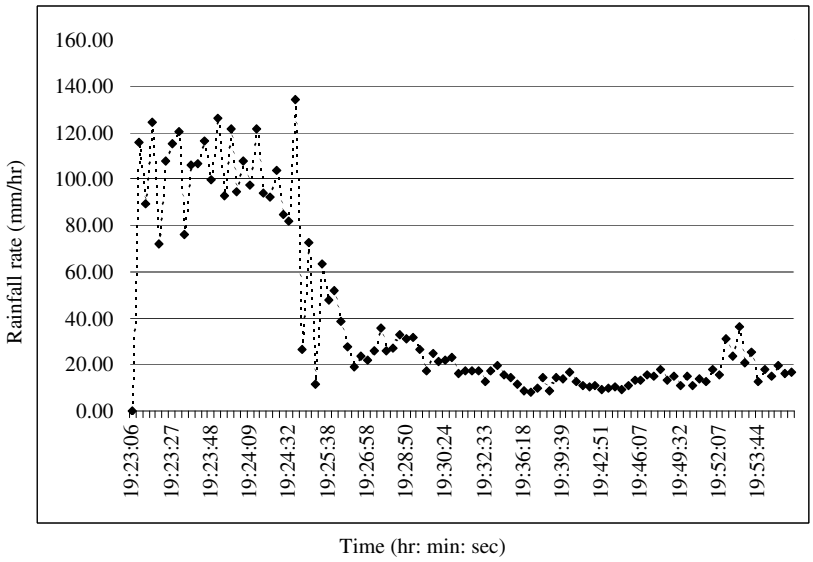

Figure 5.4: Rainfall rate measured on the 29^{th} of July 2005 at the Malmsheim air port, Baden-Württemberg, Germany.

These data points represent measurements made during rainstorm occurring once on the 29^{th} of July 2005 between $19:20$ and $20:00$ hr. Thus, a variety of meteorological conditions are not involved. The rainstorm is generally of short, heavy shower type where there was an intense onset of rain followed by a slow tapering off. The temperature during the measurement was about 28 $°C$. Because of the relatively short time required to accumulate enough rain to tip the bucket (i.e. 7.2 sec for 50 mm/hr and 3.6 sec for 100 mm/hr), the data from a tipping bucket gauge were most accurate for rainfall rate below 50 mm/hr.

5.2.2 Results and discussions

Average rain backscattering cross section

As previously pointed out, the average rain backscattering cross section $\rho< \sigma_b >$ per unit volume has been computed from the ratio of measured average power of the rain backscatter to the reference target at the middle of the rain cell volume as follows

$$\rho< \sigma_b > = \frac{\sigma_{RT}}{V_{RCR}} \frac{P_{rR}}{P_{rRT}} \ , \tag{5.3}$$

where σ_{RT} is the radar cross section of the reference target ($0.5\ m^2$), V_{RCR} is the rain cell volume, and P_{rR}, P_{rRT} are measured average backscatter power of the rain and the reference target, respectively. For both measurements, the same transmitted power P_t has been assumed. The rain cell volume has been chosen in a short distance between the range $R_{min} = 5\ m$ and $R_{min} + dR = 15\ m$ (**Figure 5.2**) so that rain attenuation could be kept minimum and negligible. In addition to that, performing a short distance measurement of rain backscattering is in favour of receiving larger rain return because of less antenna beam spreading loss.

Variability of the rain backscatter for a given rainfall intensity is expected because radar echo power from precipitation is a function of many variable parameters like number, size distribution, shape, and location of raindrops within the rain cell volume at any given moment. In order to get a more steady representative value, it was meaningful to average returned power from a number of consecutive measurements for each rainfall intensity. This is additional to what the radar weights with relative longtime ($> 1\ ms$) illumination of scatterers.

Measured average rain backscattering cross section data are presented in **Figure 5.5** in a logarithm scale. A least squares power fit of a first-order polynomial is made to these data $\rho< \sigma_b >$. The equation for this curves is of the form $Z = aI^b$, where Z is referred to as radar reflectivity in m^2/m^3. The regression coefficients, a and b have been found 0.00224 and 0.99454 as the best fit values for this rain type and location.

During the measurement, the rain has brought a storming windy air, which caused a strong fluctuation of rainfall intensities, particularly for measurements above 50 mm/hr (**Figure 5.4**). Therefore, it was difficult to

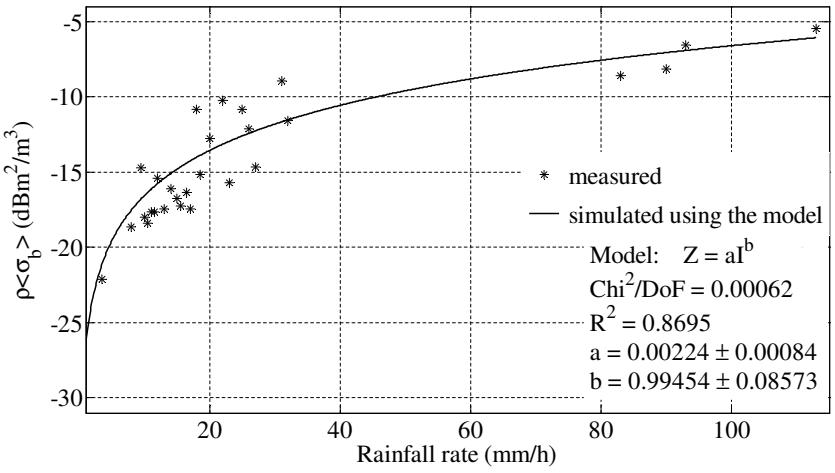

Figure 5.5: Average rain backscattering cross section measured on 29^{th} July 2005 at the Malmsheim air port, Baden-Württemberg, Germany.

arrange unambiguously the average backscattering cross section of these rainfall intensities. But generally, there is an appreciable scatter, which is typical for radar propagation data measured during rain. Since, for rainfall intensity below about 10 mm/hr, the rain drops are small with respect to the wavelength at 76.5 GHz, the backscatter follows Rayleigh scattering law where the average backscattering cross section is proportional to the six power of the drop diameter [2, Chap. 2]. This resulted in the steep slop observed in **Figure 5.5**. For rainfall intensity above about 10 mm/hr, the diameter of raindrops become in the order of the wavelength (**Figure 5.1**). So, backscattering is predominantly due to Mie scattering law where the average backscattering cross section depends weakly on drop diameter. This resulted in the gradual slop observed also in **Figure 5.5**.

Note that the larger drops, in falling, take the form of oblate spheroids and the echoes are therefore sensitive to radar polarization. As the drop size reduces, surface tension forces become more dominant and the drops become more spherical and less polarization sensitive [35].

A comparison with measurement results reported in [10, 13, 12] shows that the backscattering cross section presented in **Figure 5.5** are found to be 5 to 10 dB higher. As previously pointed out, it may be reasonably assumed

that the rain return loss due to beam spreading and rain attenuation is small. Moreover, raindrops create vertical water stalks when they hit the road. These stalks are believed to be a principal source of increased backscattering cross section when it measures just over the road using an automotive radar sensors. It has been conjectured that water stalks may increase the density of raindrops in the radar cell volume.

Note that the objective of this experiment is not only to demonstrate the measurability of rain return using automotive radar but also to pursue identification of rain in the scanning view of the radar sensor. The following section will discuss how rain could be distinguished from other scatterers like targets and terrains those may be appeared in the radar field of view.

Identification of rain using an automotive radar sensor

As it has been generally mentioned in section 3.2, automotive radar sensors operate with single scanned or multiple fixed narrow-beam antenna system, in order to discriminate targets with high angular resolution and in order to cover a wide field of view. Because of this narrow-beam properties of the antenna pattern, backscattering from most of the scatterers like vehicles and barriers may be received only by one or maximum two of the antenna beams. So, all antenna arrays should not have the same backscattering at once unless an extended scatterer like rain occupies the radar field of view (**Figure 5.6**).

Antenna beams, depend upon the design, may have the same or different antenna patterns (**Figure 3.2**). That means, to compare rain backscattering cross sections across beams, the relationship between the antenna pattern has to be taken into consideration.

If the rain cell volume is just chosen in front of radar vehicles where it may be mostly counted as an object free zone (of course regarding to traffic scenarios), all antenna beams in **Figure 5.6** should receive equal rain return. In order to verify this assumption, measurement results of average backscattering cross sections of rain have been provided to **Figure 5.7** incorporated with their first-order polynomial fitting curves.

It shows a 3 dB maximum discrepancy of measurements between beams throughout the whole rainfall intensity. This discrepancy can be referred to

as the difference in the number of raindrops between rain cell volumes in the radar beams. It may be therefore certified the heterogeneity of the rain contrary to the previous assumption local homogeneous rain.

Generally, it does seem that the measurement results from all radar beams are more or less in agreement with each other as well as with the Rayligh and Mie models. Regarding to identifications of rain by automotive radar sensors, such invariability of backscattering between antenna beams has the potential to be used as an indicator for extended scatterers. In case of emerging one and the same target in all four antenna beams, target informations (like relative velocity, distance and strength of backscattering) can be considered as an additional criteria for distinguishing rain from other objects (for example trucks in the near distance).

Regarding to the contrast of rain return and terrain backscattering, it has been seen in some works that the backscatter coefficient of, for example, traffic roads are significantly small [37, 84]. It depends on some fundamental parameters like the surface roughness, the polarization, the complex dielectric constant of the road, the frequency and the grazing angle, at which the main beam as well as the side beam may make with the road.

For an automotive radar sensor with the actual placement area (see section 4.1), the main and the first side lobs of the antenna are making incidence angles of about 3 *deg* and 6.5 *deg* with the traffic road, respectively.

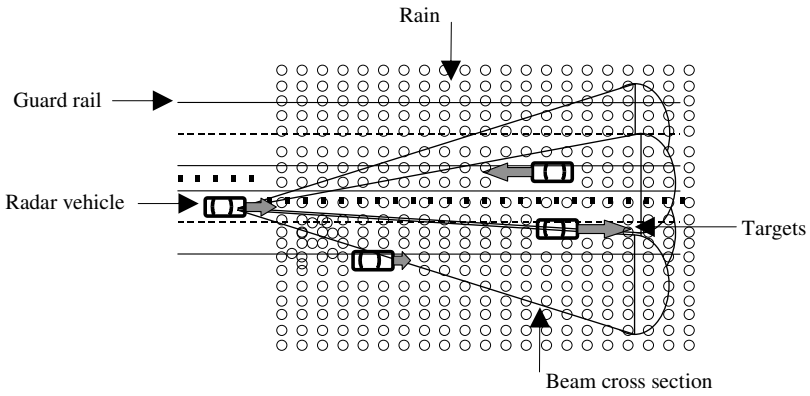

Figure 5.6: Rain as extended scatterer in the radar field of view.

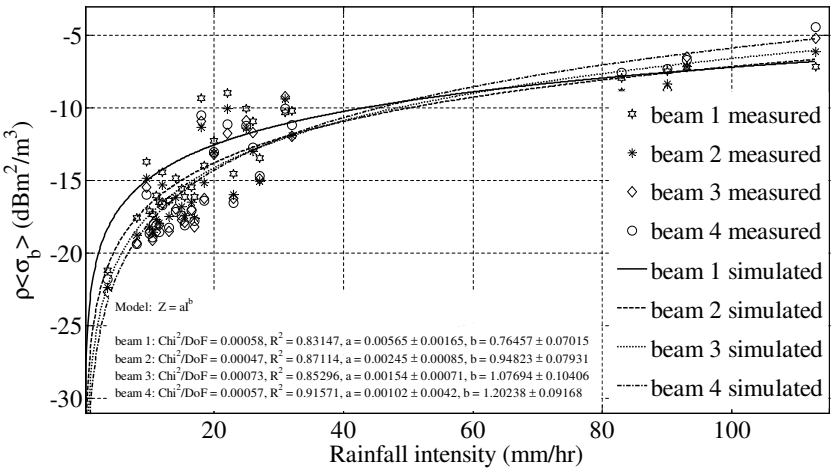

Figure 5.7: Four beam average rain backscattering cross section measured on 29^{th} July 2005 at the Malmsheim air port, Baden-Württemberg, Germany.

This may produce a maximum backscattering cross section, for example, of asphalt road lower than $-40\ dBm^2$ [46, § 4.1]. That means, for rainfall intensities higher than $4\ mm/hr$, the backscattering cross section of rain and therefore its identification may not be disfigured with road returns (**Figure 5.7**). Note that, as it will be discussed in the section below, these rainfall intensities are only accountable for significant loss of the signal-to-noise ratio.

Loss of the signal-to-noise ratio due to rain

The effects of rain on the detection performance of a radar may be generally observed through probe the reduction of the signal-to-noise ratio. As it has been demonstrated in **Figure 5.3**, this is the result of signal attenuation and increment of noise floor due to rain returns throughout the measurement range of the radar.

Note that signal attenuation due to rain is a mixture of scatter loss and absorption. Note also that the scattering and absorption cross sections are a function of the relationship between the raindrop-size and the wavelength (**Figure 2.6**). Hence, the signal-to-noise ratio has been investigated as a function of the rainfall intensity.

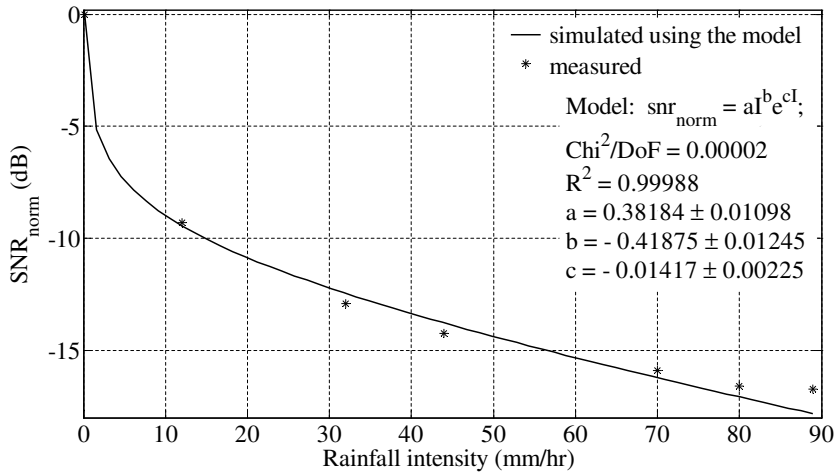

Figure 5.8: Reduction in signal-to-noise ratio due to rain, measured on 29^{th} July 2005 at the Malmsheim air port, Baden-Württemberg, Germany.

For this purpose, measurement data referred to the second reference target has been exploited (see section 5.2.1). The signal-to-noise ratio (SNR) is extracted from measurements at different rainfall intensities, and results are provided to **Figure 5.8** relative to the signal-to-noise ratio at the absence of rain. A least squares power fit of a non-linear model is made to these data. The equation for this curves is of the form $SNR = aI^b * e^{cI}$, where the terms aI^b and e^{cI} are referred to as the rain reflectivity (contributed to rise in the noise floor) and the rain attenuation, respectively. The coefficients, a, b and c have been found 0.38, -0.42 and -0.014 as the best fit values for this rain type and location.

As it is pointed out in the previous sections, **Figure 5.8** shows once again the Rayleigh and Mie scattering mechanisms applicable at different raindrop-sizes wavelength relationship. The rain generally influences the performance of an automotive radar sensor by reducing the signal-to-noise ratio of a radar target. At rainfall intensities to 10 mm/hr, the curve follows a negative steep slop that may be referred to as the Rayleigh scattering and reaches quickly a 10 dB signal-to-noise ratio loss of a radar target. Beyond 10 mm/hr, the curve continues with the negative gradual slope, related to the Mie scattering, and come up to a 16 dB signal-to-noise ratio loss by $90mm/hr$.

Relationship between the reduction in signal-to-noise ratio and the rain backscattering cross section

The models, just described in the previous paragraphs, can be used to formulate an expression about the relationship between the measurable average rain backscattering cross section and the unmeasurable loss of signal-to-noise ratio of a radar target. **Figure 5.9** shows this relationship, which has been obtained by correlating the models for average rain backscattering cross section and loss of the signal-to-noise ratio through their common physical parameter I (i.e. the rain intensity). Some measurement results have been also included in **Figure 5.9** with the model.

Although, the reduction of the signal-to-noise ratio due to rain give rise to performance loss of automotive radar sensor. This can be found out by sensing rain and its average backscattering cross sections. Despite the fluctuating behavior of targets cross section of an automotive radar sensor, the relationship shown in **Figure 5.9** may be applied to monitor the fundamental detection criteria of radar sensors, i.e. the minimum required signal-to-noise ratio.

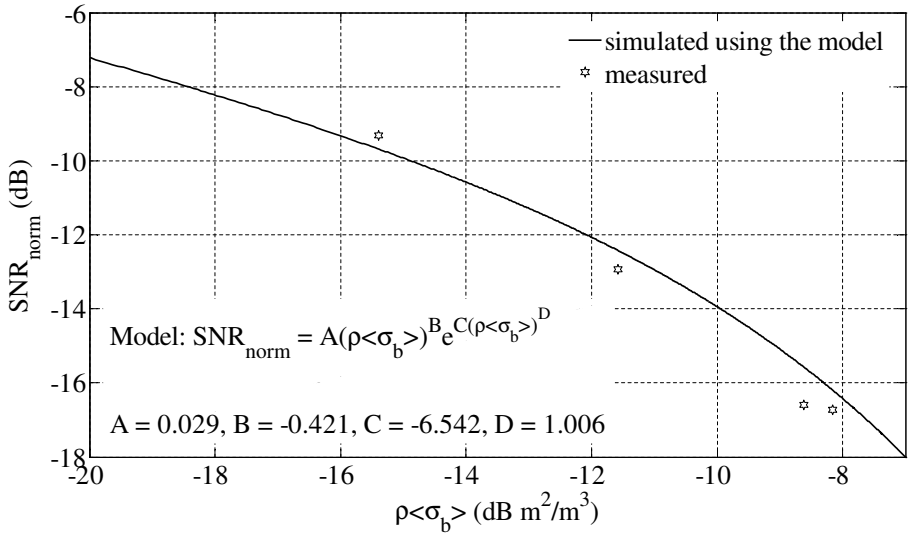

Figure 5.9: Reduction in signal-to-noise as a function of average rain backscattering cross section.

Chapter 6

Conclusions

The most immediate, and perhaps the most important use that can be applied from results of this work is in the design of millimeter-wave automotive radar sensors, which have also to operate in adverse weather conditions.

It has been pointed out that the employment of automotive radar sensors for safety-oriented applications (collision mitigation, warning and avoidance systems) requires a reliable performance at all weather conditions. Here two of the key factors that must be taken into consideration in adverse weather conditions, and their immediate recognition by millimeter wave based radar, will be briefly reviewed. The possible counteractions against the effect of these factors on operation of automotive radar sensors will be also remarked.

Two of the prime considerations in adverse weather conditions are the water film on the surface of antenna or its covering and rain in the propagation path of radar signals. Theoretical and experimental results of this work have been intelligibly expressed that the presence of these two factors may considerably affect detection characteristics of automotive radar sensors. It has been even so ascertained that millimeter-wave radar sensors have potentials to distinguish such drawback. This makes able the radar sensor system to use an appropriate means for counterbalance of sensor unreliability due to adverse weather conditions.

Water film

Since water has an imaginary dielectric property with considerable loss factor at millimeter frequencies, water film shows strong attenuation and reflection of millimeter-wave signals. Hence, the performance of millimeter-wave radar sensors suffer under wetness that can be formed on the surface of antenna or its radome during adverse weather conditions.

The amount of energy attenuated and reflected back by the water ride on the absorption property of water, whose amount on the other hand is determined by the water-quantity or thickness of the water film. This correlation between the attenuated and reflected power through thickness of the water film has given an opportunity to formulate a direct relationship between the power reflected and the actual maximum detection range of the radar (**Figure 4.4**). Therefore, in attempting to deal with the effects of water film on the detection performance of an automotive radar sensor, the reflected power from the surface of antenna or its covering radome has been observed using the following techniques.

Depending on the measurement principle of radar systems, different methods can be used to observe the reflected power from the surface of an antenna or its radome. But the one, described in this work, should be common for all radar systems and may not necessarily require to make valuable modification to sensor systems. Since the power reflected from the water film at millimeter frequencies is large enough to affect the operation characteristic of non-linear components in the radar system (e. g. mixer diode, preamplifier), it can be measured by monitoring some physical parameters of these components.

In this work, the operation point of the mixer diode has been monitored to find out degree of reflections from the surface of antenna or its radome. A calibration curve, which defines the relationship between power reflected and shift of operation point of the mixer diode, has been developed (**Figure 4.15**).

This method has been precisely enabled to detect the formation of water film and to identify its effect on the performance of automotive radar sensors, such as reduction of maximum detection range and detection capability of radar sensors. This has been experimentally verified, and measurement

results are presented in **Figures 4.16** and **4.17**. The electronic version of this work (available on request from the author) includes lab and on-road demonstrations, which show the identification of water film and its effect on detection-performance of an automotive radar sensor. Both demonstrations have been performed using the automotive radar sensor LRR2, described in this work.

Measurement results of the operation point of the mixer diode can be therefore used as water-film indicator in the automotive radar sensors, and serve to command counteractions like:

- removal of the water film, for example by thermal means (heater),
- regulation of performance by perform system-adaptation with the actual propagation medium,
- handing over of the system by switching off the radar sensor.

Note that removal of snow by thermal means (heater) may generally have an effect on the property of antenna material and lifespan. Note also that the loss due to water film may be reduced significantly by treating the surface of antenna or radome to make it non wetting, or water repellent. This method has been already experimented and shown substantial results for micro-wave airport surveillance radar and ground-based radars for satellite communications [85, 86, 87]. In case of millimeter-wave radar, particularly for automotive applications, the rain water may not be expected to form a uniform film due to exerted aerodynamic force, but forms many small streaks that rapidly ran off proper designed antenna and radome surface in narrow rivulets. However, a frozen snow and freezing rain may easily cause moist surface of antenna or radome. According to the theoretical and experimental results presented in Chapter 4, such insignificant amount of wetness can lead to considerable performance degradation of millimeter-wave radar sensors. Therefore, besides an automatic identification and neutralization of such effect, investigation of non-wetting materials like hydrophobic should be important for millimeter-wave frequencies. Due to the traditional placement of automotive radar sensors in the front grille area of a vehicle, aging and dusting have to be considered as a decisive factor by the investigating such water-repellent materials.

Rain

Further scope of this work shows that the presence of rain in the propagation path of millimeter waves causes strong attenuation and backscattering if a very big fraction of raindrops have the size in the order of the wavelength or larger. This is mainly the case for rainfall intensities greater than $4mm/hr$, known as moderate, heavy and extremely heavy rains. As a consequence, the performance of millimeter-wave radar may suffer under such rainy weather condition.

Analogous to that of the water film, the rain effects on millimeter-wave propagation (attenuation and backscattering) are correlated through the rainfall intensity. This has made possible to formulate a direct relationship between the signal backscattered and the loss of signal-to-noise ratio of the radar target (**Figure 5.9**). Note that the signal-to-noise ratio is one of the main parameter in terms of which the detection performance of a radar sensor could be judged. Therefore, in attempting to deal with the effects of rain on the detection performance of an automotive radar sensor, the near-distance backscattered power from the rains has been observed.

This is achieved by examining the average power of the rain backscattering signal from measured power spectral density through integration within the frequency range, in which the rain cell volume has been encircled (**Figure 5.2**). It is based on the principle of "Narrow-Beam First Order Multiple Scattering". An average rain backscattering cross section has been then gained at different rainfall intensities through comparison of measured backscattering signals of rain and reference target (trihedral reflector) placed at the rain range (**Figure 5.5**). The rainfall intensity has been simultaneously recorded using an accurate tipping bucket rain rate gauge and measurement results are presented in **Figure 5.4**.

The single scanned or multiple fixed narrow-beam properties of the antenna pattern of automotive radar sensors has been exploited to discriminate rain from other kinds of scatterers. An extended scatterer like rain uniformly occupies the radar field of view and result in an equal amount of measured average rain backscattering cross section between all antenna elements (**Figures 5.6** and **5.7**).

Furthermore, the loss of signal-to-noise ratio of a target with fixed radar cross section has been traced out for different rainfall intensities (**Figure 5.8**). This clearly demonstrates the impact of rain on performance of radar sensors. Since this signal-to-noise ratio loss of a target is the result of rain attenuation and increment of noise-floor due to rain return, it has been found practical to express such signal-to-noise ratio loss with measurable rain backscattering cross section (**Figure 5.9**). This is purposeful particularly for radar targets with fluctuating radar cross sections, as in targets of automotive radar sensor system.

This method is readily applicable to approximate effects of rain on performance of automotive radar sensors and to counteract with measures those may be able to compensate the loss of signal-to-noise ratio. As an example, frequency correlation is known in the literature for its application to improve target detection in a uniform precipitation. In additional to countermeasures mentioned previously, it can be appropriately employed to compensate the loss of the signal-to-noise ratio during rain.

Performance optimization

The above presented findings emphasize the importance of identification of water film and rain by millimeter-wave radars to convey information about the detection performance to radar sensor systems. An automotive radar sensor performance monitoring may be more interesting, if it could be used for performance controlling, as well.

Besides the indication of performance degradation due to water film or rain, there should have to be possibilities to make system adaptations to the actual propagation medium. As an example, **Figure B.4** presents a signal to noise ratio improvement in short ranges, in which the modulation system was able to adapted to the actual maximal detection range of the radar sensor. Such countermeasures are conceivable to improve the performance of automotive radar sensors during adverse weather conditions. Therefore, it needs to be investigated for further valuableness in the whole measurement range.

Generally speaking, an identification of water film and rain in the propagation path of millimeter wave affords access to performance controlling,

which may make automotive radar sensors more intelligent and reliable in adverse weather conditions such as rain and snow.

Appendix A

Electromagnetic plane Waves

The state of excitation which is established in space by the presence of electric charges is said to constitute an electromagnetic field. It is usually represented by two vectors, **E** and **H**, called the electric and magnetic vector respectively. A second set of vectors like the electric current density **J**, the electric displacement **D**, and the magnetic induction **B** are introduced to describe the effects of the field on material objects. The space and time derivatives of the five vectors are related by Maxwell's equations, which hold at every point in whose neighbourhood the physical properties of the medium are continuous [8, Chap. 1]. A continuous surface that is the locus of points where the electromagnetic wave vectors are in phase is called a wavefront. Consider now this electromagnetic wave traveling outward from the source in a fixed direction and have the wavefront always a plane perpendicular to the direction of propagation then it is said to represent a plane wave. This plane wave will be homogeneous, if a plane of the wavefront is as the same time a plane for constant amplitude.
The propagation of homogeneous plane electromagnetic waves can be predicted from Maxwell's equations. Such waves illustrate the interplay of electric and magnetic effects and are also of great fundamental and practical importance for topics treated in this work.
Consider a simple medium with constant, scalar permittivity and permeability, and one with no free charges and current ($\rho = 0$, $\mathbf{J} = 0$). Maxwell's

equations are then [22, Chap. 3]

$$rot\mathbf{E} = -\frac{\partial B}{\partial t} = -\mu\frac{\partial H}{\partial t} \tag{A.1}$$

$$rot\mathbf{H} = \frac{\partial D}{\partial t} = \epsilon\frac{\partial E}{\partial t} \tag{A.2}$$

$$div\mathbf{D} = 0 \tag{A.3}$$

$$div\mathbf{B} = 0 \tag{A.4}$$

For homogeneous plane waves, let's assume variation in only one direction. Take this as the $z - direction$ of Cartesian coordinate system. Then $\frac{\partial}{\partial x} = 0$ and $\frac{\partial}{\partial y} = 0$. Let start with the equations (A.1) and (A.2) in Cartesian coordinates. With the specialization defined above, equation (A.1) leads to

$$-\frac{\partial \mathbf{E}_y}{\partial z} = -\mu\frac{\partial \mathbf{H}_x}{\partial t} \tag{A.5}$$

$$\frac{\partial \mathbf{E}_x}{\partial z} = -\mu\frac{\partial \mathbf{H}_y}{\partial t} \tag{A.6}$$

$$0 = -\mu\frac{\partial \mathbf{H}_z}{\partial t} \tag{A.7}$$

and equation (A.2) leads to

$$-\frac{\partial \mathbf{H}_y}{\partial z} = \epsilon\frac{\partial \mathbf{E}_x}{\partial t} \tag{A.8}$$

$$\frac{\partial \mathbf{H}_x}{\partial z} = \epsilon\frac{\partial \mathbf{E}_y}{\partial t} \tag{A.9}$$

$$0 = \epsilon\frac{\partial \mathbf{E}_z}{\partial t} \tag{A.10}$$

Equations (A.7) and (A.10) show that the time-varying parts of $\mathbf{H}_z$ and $\mathbf{E}_z$ are zero. Thus the fields of the wave are entirely transverse to the direction of propagation. The remaining equations break into two independent sets, with (A.5) and (A.9), and (A.6) and (A.8).
The propagation behavior is illustrated by either set. Choose the set with $\mathbf{E}_x$ and $\mathbf{H}_y$, differentiating (A.6) partially with respect to z and (A.8) with respect to t:

$$\frac{\partial^2 \mathbf{E}_x}{\partial z^2} = -\mu\frac{\partial^2 \mathbf{H}_y}{\partial z \partial t}., \tag{A.11}$$

$$-\frac{\partial^2 \mathbf{H}_y}{\partial t \partial z} = \epsilon \frac{\partial^2 \mathbf{E}_x}{\partial t^2}.. \tag{A.12}$$

Substitution of equation (A.12) into equation (A.11) yields

$$\frac{\partial^2 \mathbf{E}_x}{\partial z^2} = \mu\epsilon \frac{\partial^2 \mathbf{E}_x}{\partial t^2}.. \tag{A.13}$$

The important partial differential equation (A.13) is a classical form known as the one-dimentional wave equation, having solutions

$$\mathbf{E}_x(z,t) = \mathbf{E}_t\left(t - \frac{z}{v}\right) + \mathbf{E}_r\left(t + \frac{z}{v}\right)., \tag{A.14}$$

that demonstrate propagation of a wave in the z direction with velocity

$$v = \frac{1}{\sqrt{\mu\epsilon}}.. \tag{A.15}$$

The first term of the solution in (A.14) represents an electric field $\mathbf{E}_t$ moving (or transmitted) in the positive z direction with velocity v and the second term represents the electric field $\mathbf{E}_r$ moving (or reflected) in the negative z direction, with the same phase velocity v.
The velocity v defined by (A.15) is found to be the velocity of electromagnetic wave for the corresponding medium. In particular, for free space

$$v = \frac{1}{\sqrt{\mu_0\epsilon_0}} = c\,. \tag{A.16}$$

Where c is known as speed of light. For a medium with relative permittivity ϵ_r and relative permeability μ_r the velocity of the plane wave is then

$$v = \frac{c}{\sqrt{\mu_r\epsilon_r}}\,. \tag{A.17}$$

By differentiating (A.6) partially with respect to t and (A.8) with respect to z, the equivalent one-dimensional wave equation gives solutions for the magnetic fields

$$\mathbf{H}_y(z,t) = \mathbf{H}_t\left(t - \frac{z}{v}\right) + \mathbf{H}_r\left(t + \frac{z}{v}\right).. \tag{A.18}$$

Analogous to $\mathbf{E}_t$ and $\mathbf{E}_r$ of equation (A.14), the $\mathbf{H}_t$ and $\mathbf{H}_r$ represents the transmitted and reflected magnetic field respectively. Substituting (A.14) in

either (A.6) or (A.8) and set the additive constants of integration equal to zero (i.e. neglect a field constant in space) gives on integration,

$$\mathbf{H}_y(z,t) = \frac{\eta \times \mathbf{E}_x(z,t)}{Z}.. \tag{A.19}$$

Where η is the unit vector in the direction of propagation and

$$Z = \sqrt{\frac{\mu}{\epsilon}}\,, \tag{A.20}$$

is known as the intrinsic impedance of the medium. In case of free space, it will be:

$$Z_0 = \sqrt{\frac{\mu_0}{\epsilon_0}} \approx 377 ohm\,. \tag{A.21}$$

Finally, using the Pointing theorem [22, Chap. 3], the average density of power flow in the direction of propagation will be found out from the real part of the cross product between (A.14) and conjugate of (A.18):

$$\overline{P} = \frac{1}{2}\Re\left(\mathbf{E}_x \times \mathbf{H}_y^*\right) = \frac{|\mathbf{E}_x|^2}{2Z}\eta\,. \tag{A.22}$$

For the purpose of later applications it will be useful to write down the full explicit solutions of the field equations for a wave propagated in stratified medium produced by linear polarized harmonic incidence waves. The time factor e^{jwt} will henceforward be suppressed.
Let equation (A.14) be replaces by their equivalent exponential form as derived from the one-dimensional Helmholtz equation, which states the wave equation in phasor form [22, Chap. 3]

$$\mathbf{E}_x = \mathbf{E}_t e^{-jkz} + \mathbf{E}_r e^{jkz}\,. \tag{A.23}$$

Where $k = \omega\sqrt{\mu\epsilon} = \frac{\omega}{v}$ is a constant of the medium at a particular angular frequency ω and is frequently called the wave number. The exponential form of the corresponding magnetic field can be obtained by substiting (A.23) into (A.19)

$$\mathbf{H}_y = \frac{1}{Z}\left(\mathbf{E}_t e^{-jkz} - \mathbf{E}_r e^{jkz}\right). \tag{A.24}$$

The above relationships are generally applicable as introduction for the wave propagation and scattering models in the Chapters 2, 4 and 5.

Appendix B

Supplementary Graphs

B.1 Attenuation due to hydrometeors

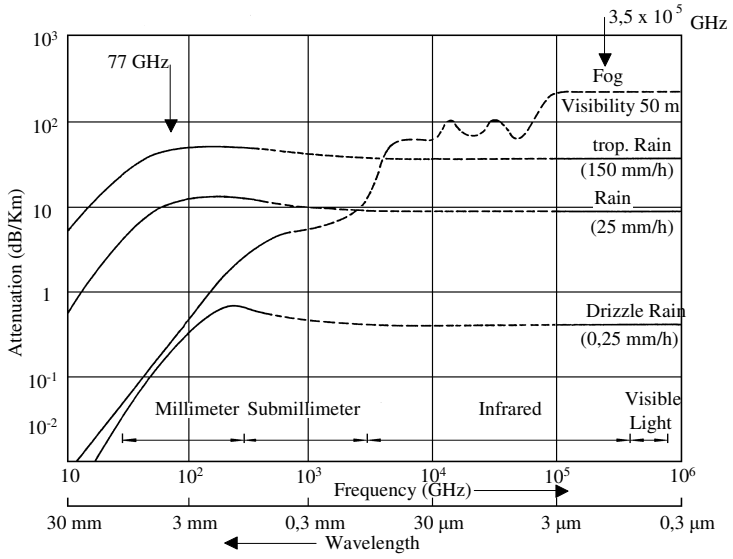

Figure B.1: Attenuation of electromagnetic wave through rain and fog, Source: [4].

B.2 The complex refraction index of water

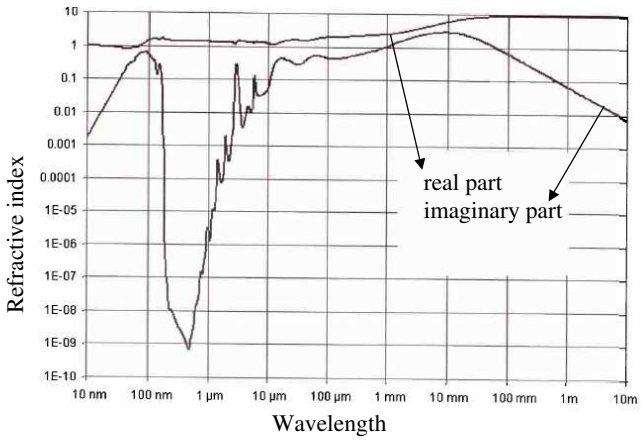

Figure B.2: Refraction index of water for wavelengths from 10 nm to 10m, Source: [88].

B.3 LRR2-transceiver layout

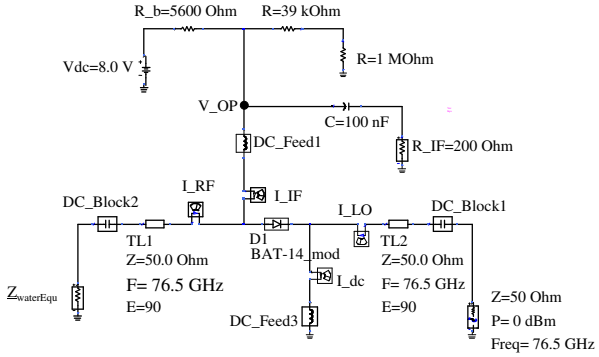

Figure B.3: Single path layout of the LRR2-Transceiver circuit including the load impedance.

B.4 Improvement of SNR due to system adaptation

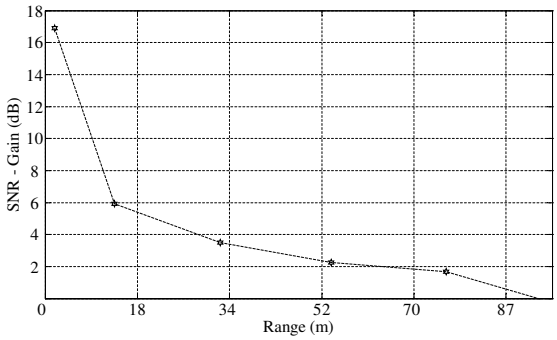

Figure B.4: Short range SNR improvement by adapting the modulation parameters.

B.5 Test car measurement system of an automotive radar sensor

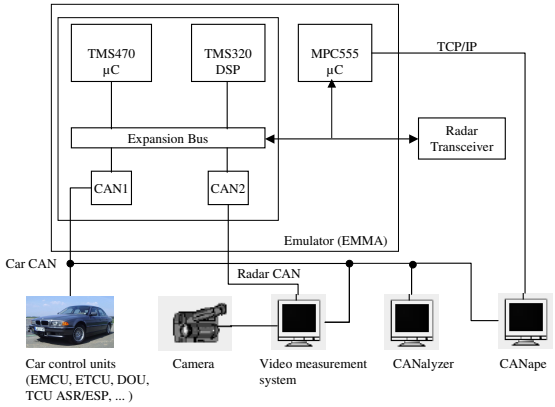

Figure B.5: Block diagram of the measurement system of an automotive radar sensor in a test car.

Appendix C

Glossary

C.1 Symbols and physical constants

a	:	molecular radius, parameter
A, $\underline{A}$	:	radar cross-section, parameter
$\underline{A}$	:	complex amplitude
α, α_T	:	angle, molecular polarizability
β	:	effective bandwidth of signal
$\mathbf{B}$	:	magnetic induction
B	:	parameter
$c \approx 3 \times 10^8\ m/s$	:	speed of light, parameter
C	:	concentration, parameter
χ_e	:	dielectric susceptibility
$\mathbf{D}$	:	electric displacement
D	:	particle diameter, aperture diameter, parameter
d	:	material thickness, parameter
δ	:	phase term, standard division
$\mathbf{E}$	:	electric vector
E	:	scalar value of the electric field
e	:	Euler's constant
$\mathbf{e}$	:	unit vector
$\underline{\epsilon}$	:	complex electric permittivity

$\underline{\epsilon_r}$	:	complex relative electric permittivity
$\epsilon_0 \approx 8.85 \times 10^{-12}\ F/m$	:	free space electric permittivity
ϵ_r'	:	real part of the relative electric permittivity
ϵ_r''	:	imaginary part of the relative electric permittivity
η	:	unit vector, viscosity
$f,\ \Delta f$	:	frequency, frequency difference
δf	:	standard division of errors for frequency
$\mathbf{f}$	:	function of the scattered wave
G	:	Antenna gain
g	:	relation between the local field acting on
	:	the molecule and the applied field
γ	:	optical distance or attenuation coefficient
H_N	:	hydration number of the individual ions
$\mathbf{H}$	:	magnetic vector
I	:	Intensity, rain Intensity
$\mathbf{J}$	:	electric current density
k	:	propagation constant, Boltzmann's constant
$\mathbf{k}$	:	propagation direction
κ	:	absorption coefficient
L	:	linear dimension
λ	:	Wavelength
Λ	:	conductivity
m	:	integer numbers
μ	:	magnetic permeability
μ_r	:	relative magnetic permeability
$\mu_0 \approx 4\pi \times 10^{-7}\ H/m$	:	free space magnetic permeability
N	:	Number of molecules per unit volume
n	:	index of refraction, particle size distribution
p_k	:	cross-polarization coefficient
$\mathbf{P}_d$	:	electrical dipole moment density
$\mathbf{P}$	:	electric polarization
$P,\ \overline{P}$	:	power, average power density
ϕ	:	antenna beamwidth in elevation, angular excursion
ψ	:	polarization angle
$\underline{Q}$	:	complex relation between the angle of incidence and
	:	angle of transmission
$\underline{r}$	:	complex reflection coefficient
$\mathbf{r}$	:	radius vector
R	:	reflectivity, distance or range of radar target
ρ	:	charges density, number of particles per unit volume
S	:	power flux density
σ	:	scatterer cross-section

$t,\ \Delta t$	:	time, time difference
$\underline{t}$	:	complex transmission coefficient
T	:	Transmissivity, period, absolute temperature
T_m	:	modulation time
δT_R	:	standard division of error for range
τ	:	relaxation time, effective time duration of signal
$\tan\delta$	:	loss tangent
θ	:	antenna beamwidth in azimuth
$v,\ v_r$	:	velocity, relative velocity
$V,\ V_{RCR}$	:	Volume, rain cell volume
$w,\ dw$	:	angular frequency, differential solid angle
$x,\ y,\ z$	:	Cartesian coordinates
$Z_0 = \sqrt{\frac{\mu_0}{\epsilon_0}} \approx 377\ ohm$	:	free space wave impedance
Z	:	wave impedance, meteorological reflectivity
$<>$	:	statistical mean or average

C.2 Abbreviations

ACC	:	Adaptive Cruise Control
ADC	:	Analog Digital Converter
AICC	:	Autonomous Intelligent Cruise Control
CM	:	Collision Mitigation
CWAS	:	Collision Warning and Avoidance Systems
CW	:	Continuous Wave
DSP	:	Digital Signal Processing
EM	:	ElectroMagnetic
FFT	:	Fast Fourier Transformation
FMCW	:	Frequency Modulated Continuous Wave
HPW	:	Half Power Width
IEEE	:	International Electrical and Electronics Engineering
MM-Wave	:	MilliMeter-wave
MMIC	:	Microwave Monolithic Integrated Circuit
NL	:	Nnumber of Layer
NLE	:	Number of Linear Equation
PLL	:	Phase Locked Loop

LRR2	:	Long Range Radar second generation
OP	:	Operation Point
RCS	:	Radar Cross-Section
RF	:	Radio Frequency
SNR	:	Signal-to-Noise Ratio
TE-Wave	:	Transversal Electric Wave
TM-Wave	:	Transversal Magnetic wave
VCO	:	Voltage Controlled Oscillator
VNA	:	Vector Network Analyzer
VSWR	:	Voltage Standing Wave Ratio
$\perp$, $\parallel$	:	perpendicular and parallel components of polarizations

Literature

[1] G. R. Wildmann, M. K. Daniels, L. Hamilton, L. Humm, B. Riley, J. K. Schiffmann, D. E. Schnelker and W. H. Wishon. Comparison of lidar-based and radar-based adaptive cruise control systems. *SAE 2000 World Congress*, March 6-9, 2000.

[2] Akira Ishimaru. *Wave Propagation and Scattering in Randome Media*, volume 1 and 2. Acadamic Press, New York, 1978.

[3] E. D. R. Shearman, E. G. Hoare and A Hutton. Trials of automotive radar performance in road spray. *IEE*, 1998.

[4] J. Detlefsen. *Radartechnik: Grundlagen, Bauelemente, Verfahren, Anwendungen*. Springer - Verlag, Berlin, Heidelberg, 1989.

[5] E. F. Belohoubek. Radar control for automotive collision mitigation and headway spacing. *IEEE Trans. Veh. Technol.*, 31:89–99, May. 1982.

[6] E. Brus. Vehicular radar: The ultimate aid for defensive driving. *Microwaves & RF*, pages 53–58, Sept. 1987.

[7] A. Kawakubo, S. Tokoro, Y. Yamada, K. Kuroda and T. Kawasaki. Electronically-scanning millimeter-wave radar for forward objects detection. *2004SAE International*, pages 127–134, 2004.

[8] M. Born, E. Wolf. *Principles of Optics*. Cambridge University Press, Cambridge, 7th edition, 2003.

[9] Edward E. Altshuler. A simple expression for estimating attenuation by fog at millimeter wavelengths. *IEEE Trans. on Antennas and Propagation*, AP-32:757–758, 1984.

[10] Joseph Nemarich, Ronald J. Wellman, and James Lacombe. Backscatter and attenuation by falling snow and rain at 96, 140, and 225 ghz. *IEEE Trans. Geoscience and Remote Sensing*, 26:319–329, May 1988.

[11] Takeshi Manabe, Toshio Ihara, and Jun Awaka. The relationship of raindrop-size distribution to attenuations experienced at 50, 80, 140 and 240 ghz. *IEEE Tranc. on Antennas and Propagation*, AP-35:1093–1096, November 1987.

[12] M. M. Z. Kharadly. Scattering by rain and melting snow. *Antenna and Propagation*, 2:406–410, 1989.

[13] Victor W. Richard, John E. Kammerer, and H. Bruce Wallace. Rain backscatter measurements at millimeter wavelengths. *IEEE Transaction on Geoscience and Remote Sensing*, 26:244–252, May 1988.

[14] Matsuo Sekine, Chii-Dong Chen, and Toshimitsu Musha. Rain attenuation from log-normal and weibull raindrop-size distributions. *IEE Trans. on Antennas and Propagation*, AP-35:358–359, 1987.

[15] Alebel Arage, Goetz Kuehnle, Rolf Jakoby. Measurement of wet antenna effects on millimeter wave propagation. *2006 IEEE Radar Conference*, 2006.

[16] Alebel Arage, Wolf M. Steffens, Goetz Kuehnle, Rolf Jakoby. Effects of water and ice on automotive radar. *German Microwave Conference*, 2006.

[17] American Institute of Physics. *American Institute of Physics Handbook*. McGraw-Hill, New York, 3rd edition, 1972.

[18] N. W. Ashcroft and N. D. Mermin. *Solid State Physics*. Holt, Rinehart, and Winston, New York, 1976.

[19] J. S. Blackemore. *Solid State Physics*. W. B. Saunders Co., Philadelphia, 1974.

[20] A. R. von Hippel. *Dielectrics and Waves*. Wiley, New York, 1954.

[21] J. A. Saxton. Dielectric dispersion in pure polar liquids at very high radio-frequencies: Ii. relation of experiment results to theory. *Proceedings of the Royal Society of London*, Volume 213:473–491, 1952.

[22] Simon Ramon, John R. Whinnery, Theodore Van Duzer. *Fields and Waves in Communication Electronics*, volume 2nd Edition. John Wiley and Sons, New York, Chichester, Brisbane, Toronto, Singapore, 1984.

[23] H. Fröhlich. *Theory of dielectrics*. Clarendon Press, Oxford, 1949.

[24] H. Eyring. *The Theory of rate processes*. McGraw-Hill Book Co. Inc, New York, 1941.

[25] J. A. Lane and J. A. Saxton. Dielectric dispersion in pure polar liquids at very high radio-frequencies: I. measurements on water, methyl and ethyl alcohols. *Proceedings of the Royal Society of London*, 213:400–408, 1952.

[26] W. J. Ellison, K. Lamkaouchi and J.-M. Moreau. Water: A dielectric reference. *J. Mol. Liquids 68*, pages 171–279, 1996.

[27] T. Meissner and F. J. Wentz. The complex dielectric constant of pure and sea water from microwave satellite observations. *IEEE Trans. Geosci. Remote Sensing 42*, pages 1836–1849, 2004.

[28] G. W. Robinson, S. -B. Zhu, S. Singh, and M. W. Evans. Water in biology, chemistry and physics: Experimental overviews and computational methodologies. *World Scientific, Singapore*, 1996.

[29] Jonathan H. Jiang and Dong L. Wu. Ice and water permittivity for millimeter and sub-millimeter remote sensing applications. *Atmospheric Science Letters*, March 31, 2004.

[30] H. Mayer. *Physik Dünner Schichten*, volume Band 4, Teil 1. Wiss. Verlag Ges. M. B. H., Stuttgart, 1950.

[31] Eugene Hecht, Adelphi University. *Optics, Second Edition*. Addison-Wesley Publisching Company, Reading, Massachusetts, 1987, 1974.

[32] R. S. Longhurst. *Geometrical and Physical Optics*. Longman Scientific and Technical Group, England, 3rd edition, 1993.

[33] Peter Beckmann, André Spizzichino. *The Scattering of Electromagnetic Waves from Rough Surfaces*. Pergamon Press LTD., Oxford, London, New York, Paris, 4 edition, 1963.

[34] Milton Kerker. *The Scattering of Light.* Acadamic Press, Inc., New York, 1969.

[35] H. Gent, I. M. Hunter and N.P. Robinson. Polarization of radar echoes, including aircraft, precipitation and tarrain. *Proc. IEE*, 110:2139–2148, December 1963.

[36] Akira Ishimaru. *Electromagnetic Wave Propagation, Radiation, and Scattering.* Prentice-Hall, Inc., New Jersey, 1991.

[37] R. L. Cosgriff, W. H. Peake, R. C. Tayor. *Terrain Scattering Properties for Sensor System Design.* Engineering Experiment Station, The Ohio State University, Columbus, 1959.

[38] S. Silver. *Microwave Antenna Theory and Design.* McGraw-Hill, New York, 1949.

[39] M. I. Skolnik. *Radar Systems*, volume 2nd Edition. McGraw-Hill, Inc., New York, 1962.

[40] G. Kühnle, H. Mayer, H. Olbrich, W. Steffens and H. C. Swoboda. Low-cost long-range radar for future driver assistance systems. *Auto Technology*, November 2003.

[41] M. I. Skolnik. *Introduction to Radar Systems.* McGraw-Hill, Inc., New York, 1980.

[42] John Gowar. *Optical Communication System.* Prentice Hall Europ, Trowbridge, Wiltshire, U.K., 2nd edition, 1993.

[43] Siemens AG: G. Mahlke, P. Goessing. *Lichtwellenleiterkabel*, volume 4. MCD Verlag, Erlangen, 1995.

[44] Reinhard Hammel. *Zur Entfernungsauflösung von Punktzielen mit FMCW-Radarsystemen.* DLR-Forschungsbericht 89-47, 1989.

[45] Klaus Peter Wagner. *Winkelauflösende Radarverfahren für Kraftfahrzeuganwendungen.* Dessertation, München, 1997.

[46] Alebel Arage. *Entwicklung und Verifikation von Möglichkeiten zur Degradationserkennung bei Adaptive-Cruise-Control (ACC)- Radarsensoren.* M. SC. Thesis, Darmstadt, 2003.

[47] Ramzi Abou-Jaoude. Acc radar sensor technology, test requirements, and test solutions. *IEEE Trans. on Intelligent Transportation Systems*, 4:115–122, September 2003.

[48] Rudolf Kuehn. *Mikrowellen Antennen*. VEB Verlag Technik, Berlin, 1964.

[49] I. J. Bahl, P. Bhartia. *Microstrip Antennas*. Artech House, Inc, Massachusetts, 1980.

[50] J. Brown. *Microwave Lenses*. Methuen and CO. LTD., London, 1st edition, 1953.

[51] Richard C. Johnson. *Antenna Engineering Handbook*, volume 3rd. McGraw-Hill Inc., New York, 1993.

[52] K. L. Fuller. To see and not to be seen. *IEE Proc.-F, Comun., Radar & Signal Process.*, 137:1–10, 1990.

[53] Jerry L. Eaves, Edward K. Reedy. *Principles of Modern Radar*. VAN Nostrand Reinhold Company, New York, 1987.

[54] A. G. Stove. Linear fmcw radar techniques. *IEE Proc.-F,*, 139:343–350, October 1992.

[55] T. V. Kerssenbrock, P. Heide. Novel 77 ghz flip-chip sensor modules for automotive radar applications. *IEEE MTT-S International Microwave Symposium*, June 13-19, 1999.

[56] L. Raffaelli. Millimeter-wave automotive radars and related technology. *IEEE MTT-S Digest*, pages 35–37, june 1996.

[57] J. Robinson, D. K. Paul, J. Bird, D. Dawson, T. Brown, D. Spencer, and B. Prime. A millimeteric car radar front end for automotive cruise control. *IEE*, 9:1–8, 1998.

[58] B. C. Blevis. Losses due to rain and radomes and antenna reflecting surfaces. *IEEE Trans. on antennas and propagation*, pages 175–176, Ap. 13, 1965.

[59] M. R. Islam, A. R. Tharek. Wet antenna effects on microwave propagation - an overview and results from sprayer tests. *Proceeding of International Wireless Telecommunication Symposium*, pages 94–97, May 17-20, 2000.

[60] G. Liu, J. T. Ong, E. Choo, and C. G. Teo. Techniques to separate wet radome loss from measured rain attenuation data during rain events. *IEE:Electronics Letters*, 36:904–906, 11th May 2000.

[61] Carlo G. Someda. *Electromagnetic Waves: Optoelectronics Imaging and Sensing*, volume Series Edition. Chapman and Hall, London, Weinheim, New York, Tokyo, Melbourne, Madras, 1998.

[62] Horst Wupper. *Grundlagen Elektronischer Schaltungen*. Dr. Alfred Huethig Verlag, Heidelberg, 2nd edition, 1986.

[63] M. R. Islam, A. R. Tharek, J. Din, J. Chebil. Measurement of wet antenna effects on microwave propagation - an analytical approach. *Microwave Conference*, pages 1547–1551, Dec. 3-6, 2000.

[64] Anritsu. *Series 371xxA Vector Network Analyzer Operational Manual*. Anritsu Co., Morgan Hill, California, 1997.

[65] K. Lange, K.-H. Löchrer. *Taschenbuch der Hochfrequenztechnik*. Springer-Verlag, Berlin, 5 edition, 1992.

[66] Martin Nilsson. Water-induced charge transport in microcrystalline cellulose. 2006.

[67] Serka Fernandez. *Dielectric relaxation study of the cellulose solvent system LICl/N,N-dimethylacetamide*. Dessertation, Regensburg, 2003.

[68] R. Raffaelli, M. Tedesco, C. Riminesi and A. Ignesti. Thickness-independent measurement of the permittivity of thin samples in the x band. *IOP Publishing Ltd, UK*, pages 503–509, 28 February 2002.

[69] P. Bhartia, I. J. Bahl. *Millimeter Wave Engineering and Applications*. John Wiley & Sons, Inc., New York, 1984.

[70] Peter A. Rizzi. *Microwave Engineering: Passive Circuits*. Prentice-Hall, Inc., New Jersey, 1988.

[71] Stephen A. Mass. *Microwave Mixers*, volume 2nd. Artech House, Boston, 1993.

[72] Zinke, Brunswig. *Hochfrequenztechnik 2, 5.Auflage, Herausgegeben von A. Vlcek, H.L. Hartnagel und K. Mayer*. Springer-Verlag, Berlin, Heidelberg, 5th edition, 1999.

[73] H. William. *Numerical Recipes*. Cambridge University Press, Cambridge, 2nd edition, 1992.

[74] Fred E. Nathanson, J. Patrick Reilly, Marvin N. Cohen. *Radar Design Principles*, volume 2nd. McGraw-Hill, Inc., New York, 1990.

[75] F. B. Dyer, N. C. Currie, and M. S. Applegate. Radar backscatter from land, sea, rain, and snow at millimeter wavelengths. *International Conference Radar 77*, pages 559–563, 25-28 Oct. 1977.

[76] Julius Goldhirsh. Prediction methods of rain attenuation statistics at variable path angles and carrier frequencies between 13 and 100 ghz. *IEEE Trans. on Antennas and Propagation*, AP-23:786–791, November, 1975.

[77] Joerg Sander. Rain attenuation of millimeter waves at wavelebgth of 5.77, 3.3, and 2 mm. *IEEE Trans. on Antennas and Propagation*, AP-23:213–220, 1975.

[78] Charles E. Hendrix, Gregory Kulon, and Thomas A. Russell. *Specification of Polarization Parameters for Optimal-Performance in Rain of Dual Circularly Polarized Radio Links*, volume 40. May 1992.

[79] TA-Shing Chu. Frequency dependence of microwave depolarization versus rain attenuation. *IEEE Trans. on Antennas and Propagation*, AP-32:994–997, September 1984.

[80] Wolfhard J. Vogel. A terrestrial rain depolarization compensation experiment at 11.7 ghz. *IEEE Trans. on Communications*, COM-31:1241–1246, November 1983.

[81] H. W. Arnold. Measurements and prediction of the polarization dependent properties of rain and ice depolarization. *IEEE Trans. on Communications*, COM-29:710–715, May 1981.

[82] J. Alfred, Jr. Bogush. *Radar and the Atmosphere.* Artech House, Inc., MA, 1989.

[83] K. L. S. Gunn and T. W. R. East. The microwave properties of percipitation particles. *Journal of the Royal Meteorol Society*, pages 523–545, 1954.

[84] Robert Schneider. *Modellierung der Wellenausbreitung für ein bildgebendes Kfz-Radar.* Dissertation, Karlsruhe, 1998.

[85] I. Anderson. Measurements of 20 ghz transmission through a radome in rain. *IEEE Trans.*, AP-23:699–622, Sptember 1975.

[86] A. Cohen, and A. Smolski. The effect of rain on satellite communications earth terminal rigid radomes. *Microwave J.*, 9:111–121, September 1966.

[87] R. M. Weigand. Performance of a water-rapellent radome coating in an airport surveillance radar. *IEEE Proc.*, 61:1167–1168, September 1973.

[88] D. J. Segelstein. *The complex refractive index of water, in physics.* University of Missouri, Kansas City, 1981.

List of published papers

- Alebel Arage, Götz Kühnle, Rolf Jakoby, "Measurement of Wet Antenna Effects on Millimeter Wave Propagation", 2006 IEEE RADAR Conference, Verona, USA, 2006.
- Alebel Arage, Wolf Steffens, Götz Kühnle, Rolf Jakoby, "Effects of Water and Ice Layer on Automotive Radar", German Microwave Conference (GeMiC) 2006, University of Karlsruhe, Germany, 2006.
- Alebel Arage, Wolf Steffens, Joachim Hauk, Götz Kühnle, Rolf Jakoby, "Identification of Wetness on Millimeter Wave Radar Surface", Frequenz: Journal of RF-Engineering and Telecommunications, vol. 60, 2006, pp. 28-30.
- Alebel Arage, Jörg Hilsebecher, Joachim Hauk, "Messung der Reflexion an einem Linsen- /Radomsystem mit Slow Speed- FSK-Modulations system", Robert Bosch GmbH, September 2005.

List of submitted patents

- Alebel Arage, Jörg Hilsebecher, Juachim Hauk, "Messung der Reflexionsstärke an der Linsen- / Radomoberfläche durch Mischerarbeitspunktverschiebung", Patentschrift: Patent Application No. 2005/0932, date of filing 16.03.2005.
- Alebel Arage, "Erkennung und Messung der Niederschlagsintensität mit Automotive Long Range Radar-System", Patentschrift: Patent Application No. 2005/2423, date of filing 21.07.2005.
- Alebel Arage, Klaus Lehre, Klar Michäl, Jörg Hilsebecher, "Frequenz-Scanning Verfahren zur Messung der Reflexion an der Linsen- / Radombelegung", Patentschrift: Patent Application No. 2006/0315, date of filing 20.01.2006.

Comment on my participation: experiments, analysis, planning, writing

Curriculum Vitae

Personal Information:

Name	Alebel Arage Hassen
Date & Place of Birth	27^{th} December 1970 in Woreillu, Ethiopia

Education:

09.1976 - 06.1980	Worillu Elementary School, Ethiopia
09.1981 - 04.1986	Woreillu Secondary school, Ethiopia
April 1986	GEC Level "A"
01.1987 - 12.1988	Associate Degree in Electro-Mechanics, Electrical and Electronics Institute, Addis Ababa, Ethiopia
04.1995 - 10.1999	B. SC. in Electrical Engineering and Information Technology, Institute of Applied Science, Giessen, Germany
04.2000 - 06.2003	M. SC. in Communication Engineering, Technical University of Darmstadt, Germany

Work Experience:

01.1989 - 08.1993	Technical Expert, Ethiopia Electric Light and Power Authority (EELPA), Addis Ababa, Ethiopia
02.1998 - 12.1999	Technical Trainee, Siemens AG, Munich, Germany
11.1999 - 12.2000	Software Developer, Siemens AG, Frankfurt a.M., Germany
01.2001 - 09.2001	Software Developer, Web Arts AG, Friedrichsdorf, Germany
01.2002 - 06.2002	Software Developer, Daimler Chrysler AG, Frankfurt a.M., Germany
11.2002 - 09.2006	Researcher, Robert Bosch GmbH, Leonberg, Germany